MASTER THESIS

Thesis submitted in partial fulfillment of the requirements for the degree of Master of Science in Engineering at the University of Applied Sciences Technikum Wien - Degree Program Mechatronics/Robotics

Exploring the Population Characteristics of Direction-Selective Ganglion Cells Across the Retinal Space

By: Jan Svaton, Bsc

Student Number: 1910228018

Supervisors: Prof. Dr. Maximilian Jösch
Ing. Richard Pasteka, Msc

Wien, September 2, 2020

FH University of Applied Sciences
TECHNIKUM WIEN

Declaration

“As author and creator of this work to hand, I confirm with my signature knowledge of the relevant copyright regulations governed by higher education acts (see Urheberrechtsgesetz /Austrian copyright law as amended as well as the Statute on Studies Act Provisions / Examination Regulations of the UAS Technikum Wien as amended).

I hereby declare that I completed the present work independently and that any ideas, whether written by others or by myself, have been fully sourced and referenced. I am aware of any consequences I may face on the part of the degree program director if there should be evidence of missing autonomy and independence or evidence of any intent to fraudulently achieve a pass mark for this work (see Statute on Studies Act Provisions / Examination Regulations of the UAS Technikum Wien as amended).

I further declare that up to this date I have not published the work to hand nor have I presented it to another examination board in the same or similar form. I affirm that the version submitted matches the version in the upload tool.“

Wien, September 2, 2020 Signature

Kurzfassung

In meiner These, habe ich eine neuartige Methode erkundet, die ein 40-mal größeres Sichtfeld und damit die Ueberwindung von den erwähnten technischen Limitierungen ermöglicht. Die These benutzt diese Methode um die Bevölkerungsmerkmale von Richtungsselektiven Ganglienzellen in der gesamten Fläche von Maus-Retinas zu untersuchen. Durch die Nachbildung von bereits bekannten Merkmalen und Mustern konnten wir diese neue Aufnahme-Methode für gültig erklären. Des Weiteren, diese These betrachtet die Wirkung von Adjuvantien, welche die globale Infektionsrate von den retinalen Ganglienzellen erhöhen können. Dies kann potentiell die unvoreingenommene Aufnahme der Ganglienzellen erleichtern. Außerdem, wird eine neue Art der Anregung um die Empfangsfelder der retinalen Ganglienzellen zu bestimmen vorgestellt. Dieser neuer Stimulus übertrifft konventionelle Stimuli sowohl in der Auflösung der erhaltenenen Empfangsfelder und erlaubt eine Verkuerzung der Präsentationszeit. Es eröffnet zum ersten Mal die Tür für folgenden Studien, die das Verteilungsmuster der Emfangsfelder über die gesamte Retina-Fläche erkunden und verbesstert die Fähigkeit der Einteilung in Zellklassen.

Schlagworte: Retina, Bildaufnahmen, Richtungsselektive Ganglienzellen, Empfangsfeld

Abstract

This thesis explores a newly developed method that uses a FOV, which is 40-times larger in comparison with conventional optical methods, allowing me to overcome this technical limitation. I have used this novel method to explore population characteristics of direction-selective ganglion cells (DSGCs) across the retinal space of mouse retinas. By recreating already known population patterns, I confirmed that our novel imaging method works. In addition, this thesis investigates the effects of adjuvants for enhanced global infection rates of retinal ganglion cells (RGCs) that may potentially facilitate the unbiased recording of RGCs and introduces a novel stimulus for inspecting receptive fields (RFs) of RGCs. This novel stimulus outperforms conventional stimuli used in current studies in both the resolution of the yielded RF and the necessary time of stimulus presentation. It opens the door for following studies to describe for the first time the distribution patterns of RFs across the retinal space and to improve the clustering of cell classes.

Keywords: Retina, Imaging, Direction-selective ganglion cells, receptive fields

Contents

1 Rozšířený abstrakt

1.1 Cíle práce

Diplomová práce se zaměřuje na populační vlastnosti směrově selektivních gangliových buněk (DSGCs) a jejich distribučních vzorců napříč sítnicí. Takovéto téma představovalo velmi pracný úkol pro předchozí studie a existuje tudíž jen hrstka studií, které tento jev zkoumají (Sabbah et al., 2017). V této diplomové práci bychom chtěly předešlé objevy zreplikovat pomocé naší nové metody jednofotonové mikroskopie, která poskytuje mnohem větší zobrazovací pole než konvenční zobrazovací metody.

Kromě toho chceme zjistit, jak stabilní jsou vlastnosti DSGCs. Většina studií o DSGCs je založena na předpokladu, že jejich vlastnosti jsou statické a nezávislé na scéně, kterou DSGCs kódují. V důsledku toho většina studií používá široký výběr umělých stimulů, které (1) mohou hypoteticky vyvolávat odlišné DSGC odpovědi a (2) kvůli jejich umělosti nemusí být zcela vhodné, jak již některé studie odhalily (Felsen a Dan, 2005). Pokud by byla pravda, že směrově selektivní vlastnosti jsou závislé na prezentovaných podnětech, řada stávajících studií by musela být přezkoumána.

Pro zkoumání vlastností DSGC použijeme wilde-type laboratorní myši, intravitreálně injekované adeno-asociovanými viry (AAV), které obsahují geneticky kódované indikátory neuronální aktivity. Míra AAV infekce se může lišit od sítnice k sítnici a představuje tak jisté zkreslení v šíření geneticky kódovaných indikátorů napříč sítnicí. Tento zkreslující účinek bychom chtěli zmírnit a získat co nejvíce infikovaných buněk pomocí vybraných adjuvancií, které by měly posílit AAV infekci sítnice.

Posledním cílem této práce je navrhnutí stimulu, který by lépe popsal receptivní pole (RF) DSGC, než popisují konvenční stimuly. Vytvoření stimulu, který by poskytl vysokorozlišovací RF, by mohlo odhalit nové skutečnosti o skladbě sítnice odlišnými podtypy DSGC a pomoci lepší klasifikaci tříd sítnicových gangliových buněk.

1.2 Metodika

Vlastnosti DSGCs byly zkoumány v myších divokého typu (wilde-type) za pomoci geneticky exprimovaných kalciových indikátorů s červeně posunutým spektrem. Konkrétně byly využity adeno-asociované viry *AAV2.9.Syn.NES.jRCaMP1a.WPRE.SV40* a *AAV-dJ-hSyn-CAR-GECO1*. Přesný postup intravitreálních injekcí a sítnicové disekce je popsán v anglické části textu níže.

Table 1: Shrnutí testovaných AAV a jejich adjuvantů

Vir	Myší	Adjuvant	Adjuvant pozn
AAV2.9.Syn.NES.jRCaMP1a.WPRE.SV40	2	-	-
AAV-dJ-hSyn-CAR-GECO1	3	-	-
AAV-dJ-hSyn-CAR-GECO1	3	D-Mannitol	10 % s AAVs
AAV-dJ-hSyn-CAR-GECO1	3	Dexamethasone	Intravitreálně, pre 1h
AAV-dJ-hSyn-CAR-GECO1	3	Dexamethasone	Intraperitoneálně, pre 24h

Zjednodušené schéma mikroskopu nového typu, sestrojeného v naší laboratoři, je znázorněn na obrázku níže. Celé zařízení je ovládáno počítačem, který generuje stimuly navržené a renderované v Psychophysics Toolbox Version 3 (toolbox MATLAB).

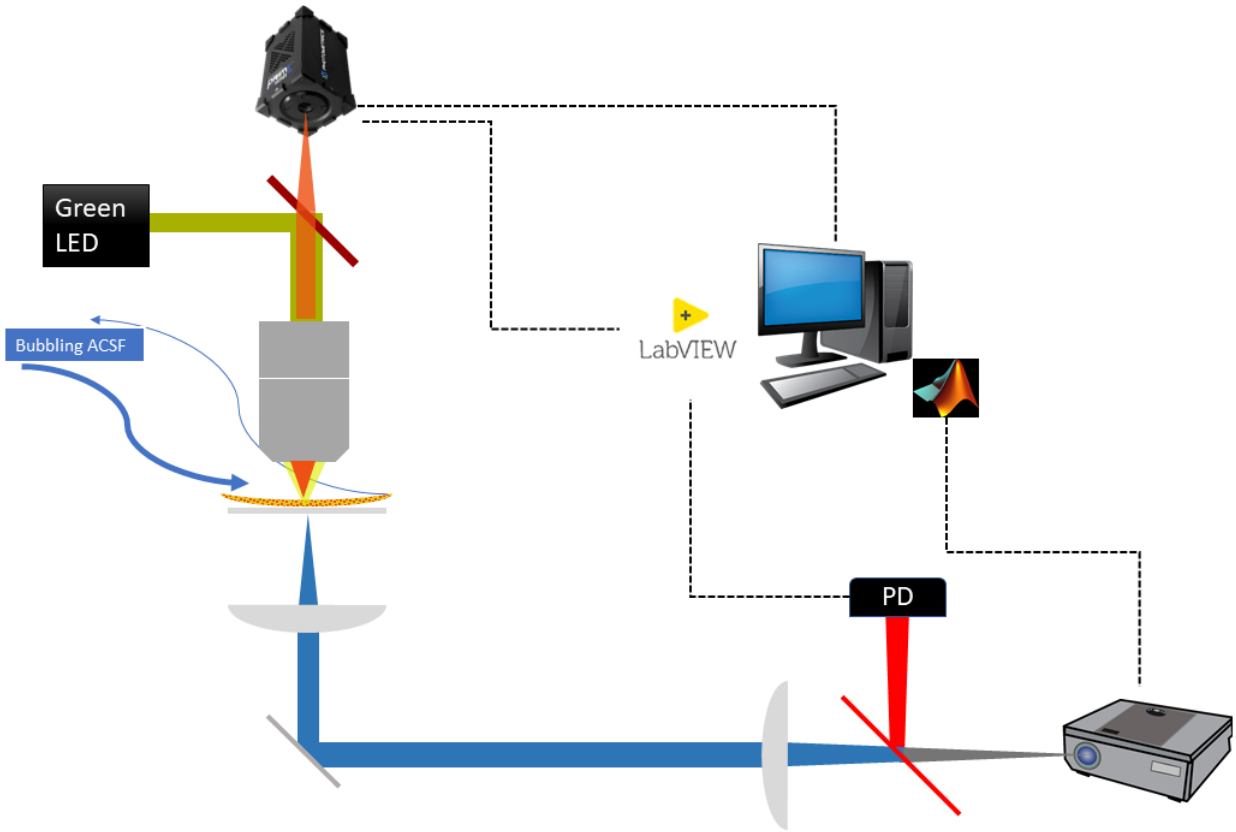

Figure 1: Schému nového jednofotonového fluorescenčního mikroskopu. Řídící počítač generuje sitmuli, které jsou přes upravený projektor promítány na vypreparovanou sítnici pod objektivem. Sítnice je perfuzována okysličeným umělým mozkomíšním mokem, který buňky udržuje naživu. Zelená LED současně osvětluje sítnici a dodává tak potřebnou fluorescenční energii. Výsledná fluorescence je pak zachycena objektivem a přes červený filtr míří vzhůru do kamery.

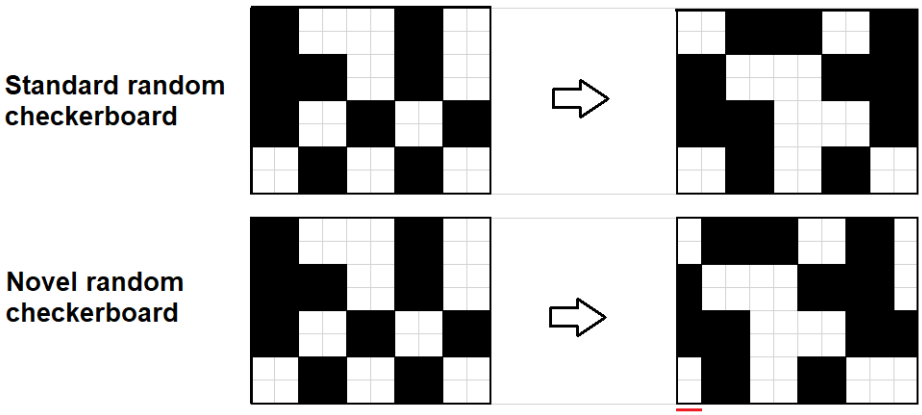

Figure 2: Ilustrace nového RF stimulu: konvenční stimulus generuje černé/bílé pixely v dané mřížce, které je fixní po celý experiment. V novém stimulu se tato mřížka náhodně pohybuje v každém kroku

1.3 Výsledky

Prokazatelný účinek adjuvancií se neprokázal: mnohem výraznější efekt má volba samotného AAV serotypu. Existují dva možné důvody, proč adjuvancia neúčinkovala podle očekávání. Za prvé, předchozí studie o účincích těchto adjuvancií byly provedeny v mozku myší místo sítnic, ve kterých mohou adjuvancia fungovat odlišně. Za druhé, adjuvancia (nebo alespoň některé z nich) mohly fungovat, ale účinek byl nepatrný kvůli jiným souběžným vlivům na šíření infekce. Jelikož intravitreální injekce byly prováděny ručně, mnoho jejich atributů (například rychlost injekce, místo injekce atd.) se lišily od oka k oku. V neposlední řadě je každá myš fyziologicky jedinečná a průběch infekce se tak může lišit. Testováním mnoha dalších sítnic bychom pravděpodobně mohli vidět skutečný účinek adjuvancí, avšak takový úkol byl nad rámec této diplomové práce.

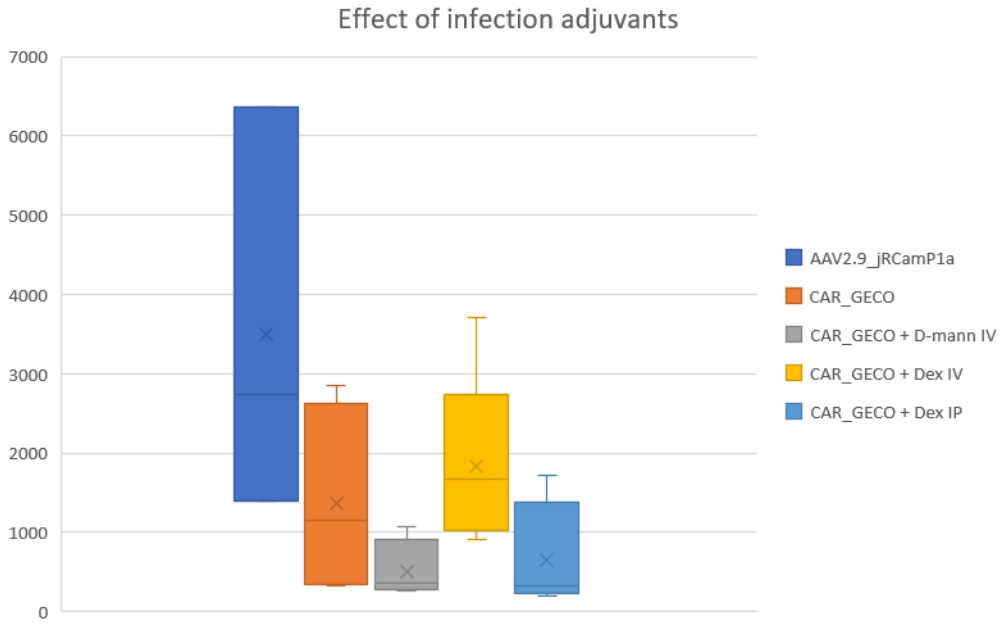

Figure 3: Výsledek efektu adjuvancií pro zvýšení virové infekce: *AAV2.9.Syn.NES.jRCaMP1a.WPRE.SV40* působil lépe než *AAV-dJ-hSyn-CAR-GECO1*; efekt samotných adjuvancií zůstává diskutabilní.

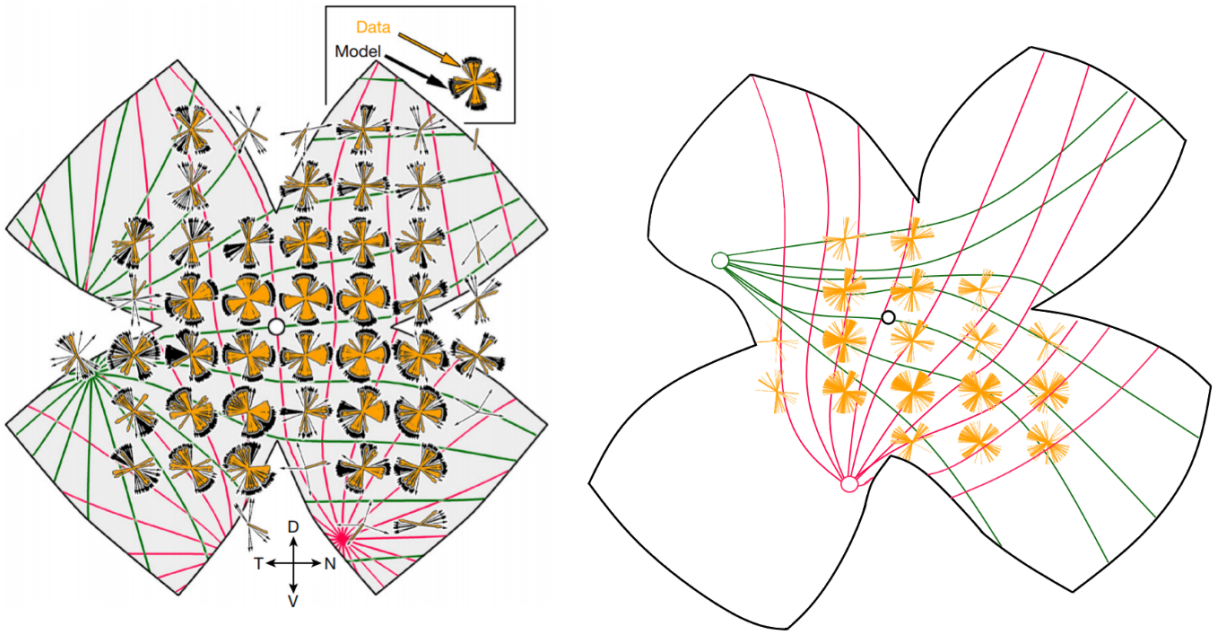

Figure 4: Replikovaná populačni DSGC studie pomocí našeho nového mikroskopu. Vlevo: Sabbahova studie o distribuci DSGCs na sítnici - zelené a růžové křivky značí meridiány translačních a rotačních optických polí; bylo použito 26 sítnic s více než 2400 DSGCs. Vpravo: Výsledek naší replikační studie. Berte v potaz, že meridiány byly domalovány pro ilustraci; byla použita pouze 1 sítnice s 951 DSGCs.

Replikací studie o známých DSGC populačních vlastnostech (Sabbah et al., 2017) jsme prokázali, že naše nová metoda jednofotonové fluorescenční mikroskopie funguje a že ji lze použít pro jiné rozsáhlé studie sítnic. Díky přibližně 40krát většímu zornému poli, než mají běžné konvenční zobrazovací metody, naše metoda umožňuje provádět velké populační záznamy neuronální aktivity a to pouze s pár experimenty, ve srovnání s desítkami nebo dokonce stovkami experimentů při použití konvenčních metod. Kromě toho je aparát relativně levný, takže nejmodernější neuronální populační studie jsou dostupné i pro další laboratoře.

Kromě replikace existující rozsáhlé studie tato práce také představuje vylepšený stimul pro výpočet receptivních polí gangliových buněk sítnice. Tento nový stimul dokázal získat receptivní pole při mnohem vyšším rozlišení, než bylo dříve dosaženo a to vše během několika málo minut. Spolu s naší novou velkoplošnou fluorescenční zobrazovací metodou nemusí vylepšené stimuly vést jen k novým objevům týkajících se skládání sítnice odlišnými podtypy DSGCs, ale také otevírají dveře následujícím studiím, které poprvé v historii mohou popsat distribuci RF napříč sítnicí.

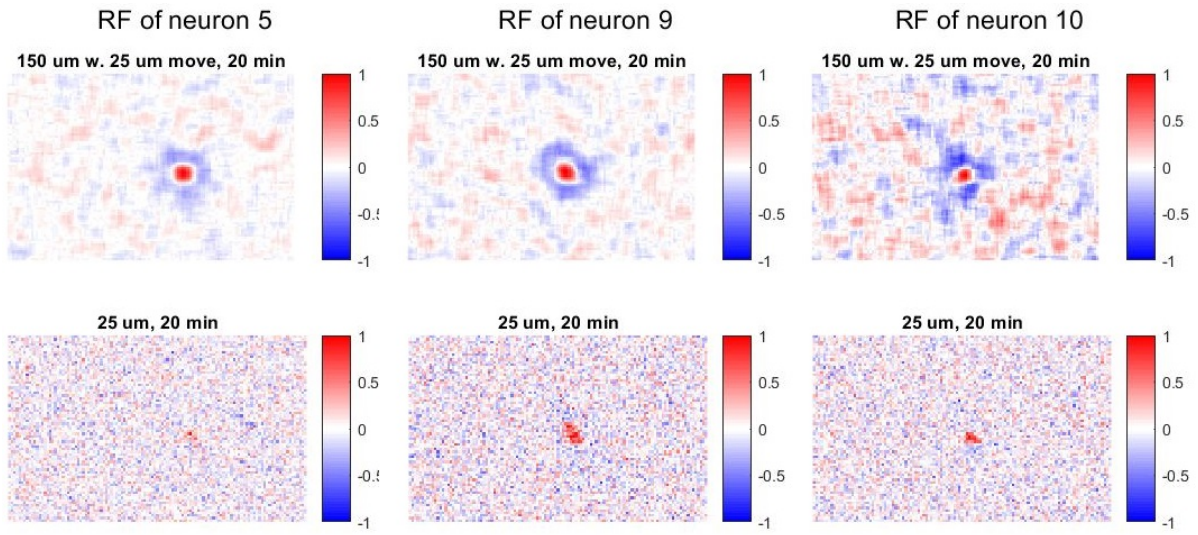

Figure 5: Ukázka síly nového RF stimulu: dokážeme detekovat buňky s ON vnitřkem a OFF vnějškem. Tyto vlastnosti jsou s konvenčním stimulem nedetekovatelné

2 Introduction

How do we see what we see? This may be one of the oldest and most daunting questions in philosophy and neuroscience that still remains largely unanswered today. To understand how we process images of the outer world in our minds, it is wise to start unravelling this mystery from where it all begins: the retina.

Theories and views on the function of the retina have changed dramatically over the past few years. Only a few decades ago, many textbooks and review articles (for example Meister & Berry (1999)) assumed that the main purpose of the retina is simply to convey a visual image to the brain, where intensive neural computing would decipher the vast barrage of information it sees. The retina was thought to serve merely as a light adaptation and a lateral inhibition mechanism that would help to normalize the image that was being relayed to the brain (Gollisch & Meister, 2010).

Today, scientists believe that the retina is smarter than previously thought: rather than just relaying an altered pixel-wise version of an image it sees, it extracts distinct features about the visual space (Gollisch & Meister, 2010). The features presumably contain compressed information about important things that are happening in the visual scene. For instance, they indicate detection of motion, its direction, orientation or the approach of an object. Detection of these features is vital and perhaps that is the reason why mammals are already born with hard-wired retinal circuits that implement their extraction. These circuits are assembled from selective wiring among five classes of retinal neurons (described in the next chapter). Outputs of these feature-extracting circuits are integrated by distinct types of retinal ganglion cells and sent to downstream brain areas. In this way, the retina potentially reduces the load of information for the brain.

One feature of particular interest to this thesis is direction-selectivity. The corresponding type of retinal ganglion cells, that are active only when an object moves in a particular direction across the visual space, are hence called direction-selective retinal ganglion cells (DSGCs). Although they were discovered more than half a century ago (Barlow & Hill, 1963) and many of the details on how their circuitry works have already been explained, many of their population properties still remain unexplored today.

In the past, DSGCs have been studied using either electrophysiological or two-photon imaging techniques that allowed simultaneous recording of DSGCs in a relatively confined area of

$\sim$ 200 x 200 μm^2. While these techniques helped to explain a great deal about the neural circuitry of DSGCs (Briggman et al., 2011; Euler et al., 2002; Yonehara et al., 2013; Matsumoto et al., 2019), they are rather cumbersome for studying the population properties of DSGCs and their distribution patterns across the retinal space. This had substantially constrained our understanding of how motion is relayed on a global level. Furthermore, as recent studies have shown, only by studying populations of DSGCs can we unravel their emergent properties that were elusive in the past (Kühn & Gollisch, 2019; Zylberberg et al., 2016). Thanks to the novel one-photon microscopy method, developed in our lab, we are able to easily explore thousands of DSGCs within one single experiment. In comparison, achieving such feat with the conventional 2-photon microscopy approach would require tens of experiments and numerous laboratory animals lives.

In this thesis, I want to take a look at the population properties of DSGCs and their distribution across the retinal space. This was a very laborious task for previous studies and hence there are only a few that investigate this phenomenon (Sabbah et al., 2017). I would like to replicate their findings with our novel one-photon microscopy method and if possible, discover new patterns that were previously overlooked.

In addition, I want to see how stable direction-selective responses of DSGCs are. Most studies on direction-selectivity are built on an assumption that direction-selective properties are static and independent of the scene which DSGCs encode. Consequently, most studies use a wide selection of artificial stimuli, which (1) may hypothetically elicit different direction-selective responses and (2) due to their artificiality, may not be optimal to use in the first place, as some studies have already revealed (Felsen & Dan, 2005). If it were true that direction-selective properties are stimuli-dependent, a number of existing studies should be questioned and rethought.

To investigate DSGCs properties, I will use wild-type mice injected intravitreally with adeno-associated viruses (AAVs), containing genetically encoded indicators of neuronal activity. Since the retinal AAV infection rate might vary from retina to retina, it can constitute bias in the spread of genetically encoded indicators across the retina. I would like to ameliorate this effect and obtain as many infected cells as possible with the use of selected adjuvants that should boost the retinal AAV infection.

Finally, I want to design a stimulus that would better describe the receptive fields (RFs) of DSGCs than conventional stimuli do. Creating a stimulus which would yield high-resolution RFs could potentially elicit new findings on the tiling of the retina with distinct DSGCs subtypes.

3 First Steps of Seeing: the Structure and Function of the Mouse Retina

The structure and function of the mouse eye is very similar to our eye: the main principle of utilizing cornea and lens to refract light and form an image on the photosensitive layer of the retina is the same as in other vertebrates. The same applies for the structure of the mouse retina, which is highly stratified and commonly separated into five distinct layers, presented in schematic diagram 6B. Three of these layers are composed of cell bodies: *outer nuclear layer*, comprised of rods and cones, *inner nuclear layer*, comprised of bipolar cells, horizontal cells and OFF-amacrine cells, and finally, *ganglion cell* layer, which except ganlgion cells contains also ON-amacrine cells. These nuclei layers are separated by two synaptic layers, where wiring among nuclei of adjacent layers occurs. These two synaptic layers are shown in the schematic under the terms "plexiform layers" (Latin plexus = a braid): *outer plexiform layer*, which connects photoreceptors with bipolar and horizontal cells, and *inner plexiform layers*, where bipolar and horizontal cells make synaptic connections with amacrine cells and dendrites of ganlgion cells (Rodieck & Rodieck, 1998).

Of course, some differences of the mouse eye and retina compared to ours exist. For instance, mouse retina lacks *fovea centralis*, a retinal spot with the densest concentration of cones and no rods. It is estimated that mouse visual acuity is only about 1 $\%$ of human vision and the rest of the cognitive information that helps mouse to navigate around its whereabouts is made up by olfactory, tactile and auditory cues (Baker, 2013). Also, due to the overall small body size, the axial length of the mouse eye is only about 3.4 mm with majority of the vitreous body being substituted by a lens, as depicted in Figure 6A.

3.1 Mouse Photoreceptors

Photoreceptors are depicted at the top of the schematic 6B. This is the outermost part of the retina, while the bottom of the schematic, where ganglion cells are located, is oriented in the interior of the eye. In this sense, light comes from the bottom and crosses all nuclei only to be registered by photoreceptors right at the top. Photoreceptors then converts photons into neuronal signal, which cascades across bipolar, horizontal and amacrine cells back to the bottom, where ganglion cells recollect the signal and relay it further to the brain.

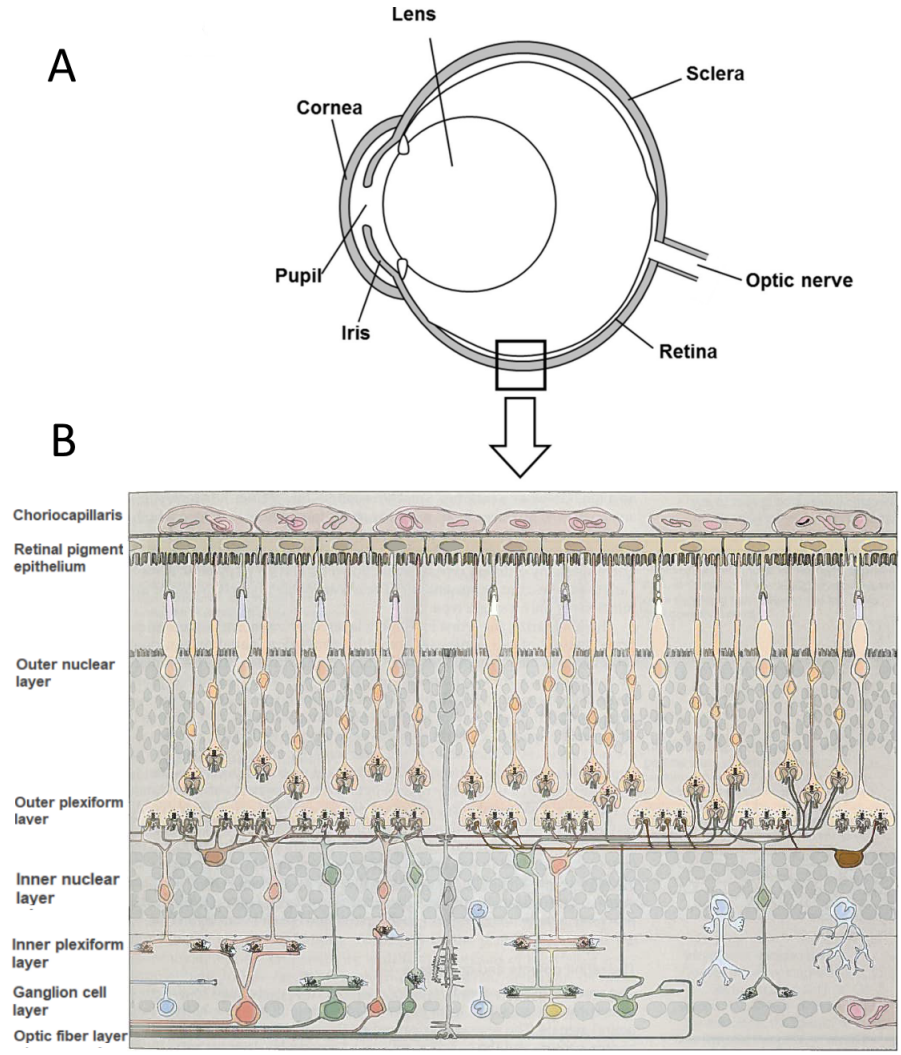

Figure 6: A: simplified model of the mouse eye anatomy. Source: Peirson et al. (2018, Fig. 1A); B: schematic diagram depicting stratified structure of the retina; thickness of the retinal section is approximately 200 μm. Source: Baker (2013, p. 39, edited).

At first sight, this kind of design seems somewhat counterintuitive - why would be the light detected only right at the end of the retina? Would not the information, carried by photons, be dispersed and therefore hampered by the neural tissue? Even though this is a valid argument, the ground reason why the retina evolved this way is the substantial energetic demand of the photoreceptors. In this way, the retinal pigment epithelium and choriocapillaris (top of the schematic) lay right behind the photoreceptors and provide needed nourishment, oxygenation, and regenerate photopigment via visual cycle (Thompson & Gal, 2003).

As stated earlier, mice did not evolve *fovea centralis*, a highest acuity spot with the densest concentration of cones and no rods. There are two schools of thought on whether mice possess so-called *area centralis*, a spot where density of photoreceptors and ganglion cells peaks

and decreases laterally from there on (Peirson et al., 2018; Leamey et al., 2008; Sundberg et al., 2001). According to Leamey, the *area centralis*, is located temporally to the optic disc. Yet, the photoreceptor density in mouse *area centralis* is still only comparable to the peripherial parts of the cat retina (Leamey et al., 2008; Peirson et al., 2018).

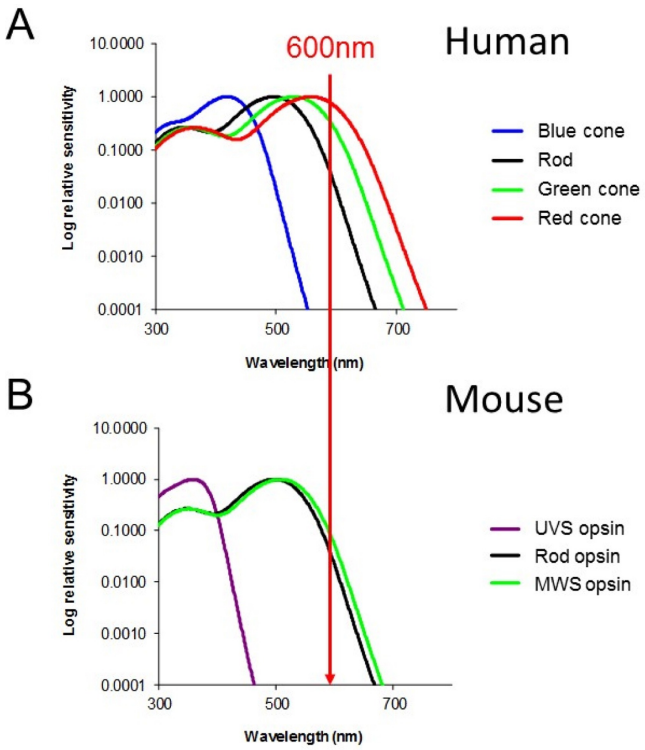

Figure 7: Comparison of opsin sensitivity distribution across visual spectrum for human (A) and mouse (B). A red light stimulus at 600 nm, will be 12 time less sensitive for mice than for humans. Source: Peirson et al. (2018, Fig. 2).

Interestingly, mouse photoreceptors occupy approximately whole half of the retina. Due to nocturnal lifestyle of mice, the retina is heavily rod-dominated: around 97 %, or 6.4 million, of all photoreceptors are rods that operate in dim light (scotopic vision) (Leamey et al., 2008). The remaining 3 % are cones, which mediate bright light (photonic vision). Unlike us, mice possess only two cone visual pigments: an ultraviolet light sensitive (UVS) opsin and a middle-wavelength sensitive (MWS) opsin, which peak sensitivities are at 360 nm and 510 nm, respectively (Jacobs et al., 1991). The peak sensitivity of rod opsin is at 498 nm (Bridges, 1959). Due to this imbalance of spectral distribution of opsins, mice are much more sensitive to short wavelengths compared to humans. Vice versa, mice are relatively dull in discerning long wavelengths: they are 12 times less sensitive to red light stimulus at 600 nm compared to humans, as presented in Figure 7 (Peirson et al., 2018). Our novel one-photon optical method, described later, takes advantage of this property.

3.2 Horizontal Cells

As their name suggests, horizontal cells, depicted in brown in the inner nuclear layer of the schematic diagram 6B, have rather horizontal than vertical connections with photoreceptors and bipolar cells. Their main purpose is to sharpen contrasts (thus to emphasize the borders of objects in the visual scene) and to implement color vision based on rod-cone opponency in dim light conditions (Kalat, 2016; Joesch & Meister, 2016). Both of these features are obtained via subtracting inputs of adjacent photoreceptors by horizontal cells. This mechanism is known as *lateral inhibition*.

Interestingly, edge detection algorithms in computer vision sharpen contrasts similarly as horizontal cells do. The principle of *lateral inhibition* is relatively simple and can be illustrated on contrast-sharpening masks. Such masks highlight a pixel which resides in the center of the mask, while subtracting pixels in the surround. This mathematical operation leads to highlighted borders (sharpened contrast) of an image. The neurocircuit operation of horizontal cells is very similar: each horizontal cell excites only adjacent bipolar cell while inhibiting other bipolar cells in the surround.

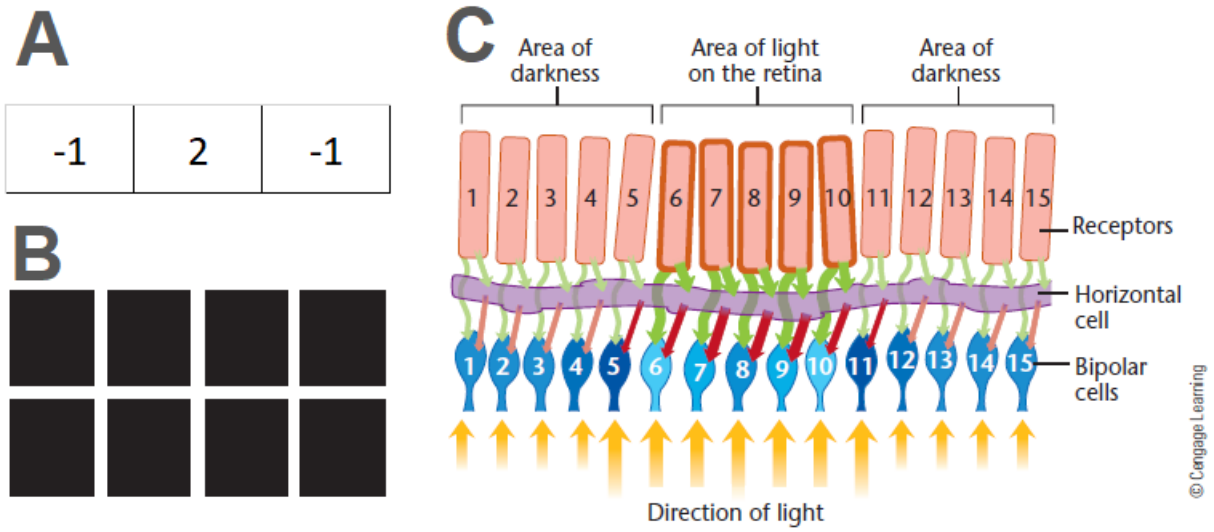

Figure 8: A: Kernel of a simple, one dimensional sharpening mask: pixel in the center is highlighted (multiplied by 2) while surrounding pixels are subtracted; by convoluting this mask with an image we sharpen the image (highlight its contrasts). B: Illustration of lateral inhibition: you should see black flickering dots at the white "crossroads". C: Neurocircuitry of lateral inhibition. In reality, light decreases activity of photoreceptors, which have inhibitory connections onto bipolar cells. To avoid such double negations and keep things simple, the connections of photoreceptors onto bipolar cells are depicted as excitational (green arrows). Horizontal cells excite adjacent bipolar cells, which lay right under them, and inhibit cells in their close proximity. The net result is the following: the most excited bipolar cells are the ones that are on the edges of the incoming light (yellow arrows). Source: Kalat (2016, p. 164).

3.3 Bipolar Cells

Bipolar cells receive input from photoreceptors and horizontal cells and project their changing levels of activation further onto amacrine and ganglion cells. There are about thirteen different types of bipolar cells (Rodieck & Rodieck, 1998). To keep things simple, they can be grouped depending on the three following characteristics:

1. **Number of input connections from photoreceptors**
   In the *area centralis*, some bipolar cells tend to make contacts with only a few photoreceptors (e.g. midget bipolar cells) and thus they relay acute image of the visual scene. Vice versa, in the periphery, inputs from many photoreceptors converge into a single bipolar cell (e.g. diffusive bipolar cells), resulting in facilitated sensitivity to faint light, but decreased spacial acuity (Kalat, 2016). The specific part of the visual scene that a cell is responsive to is known as a receptive field (RF).

2. **Type of dendritic contact**
   Bipolar cells can be activated either by increase or decrease of light, depending on whether their dendrites connect to the center or periphery of photoreceptor axonal invagination (see Figure 9) (Rodieck & Rodieck, 1998). Cells that are activated by the increase of light are termed "ON" cells (presented in green in Figure 9). Those that increase their activity upon decrease of light are termed "OFF" cells (orange in Figure 9).

3. **Type of afferent photoreceptor**
   Each bipolar cell can be also defined by the type of presynaptic photoreceptor. For instance, on-midget bipolar cell that receives inputs from UVS-cone is be termed *UVS-On-midget bipolar cell*.

It is important to note that these features propagate further to RGCs, which inherit their distinct RFs and ON/OFF responses.

3.4 Amacrine Cells

Amacrine cells constitute the most diverse and unknown group of cells within the retina. They contain around 40 different cell types that vary greatly in morphology, size and function, and form the most intricate ciruitry in the retina: amacrine cells receive signals from bipolar and other amacrine cells and project onto yet another amacrine, bipolar cells and ganglion cells. Due to this wiring complexity, most of their functions remain largely unknown (Rodieck & Rodieck, 1998).

Some ganglion cells exhibit specific functional properties, which cannot be explained by just integration of signals coming from bipolar cells and it is most likely that further neurocomputations are needed to make up their functional properties. As it turned out, amacrine cells

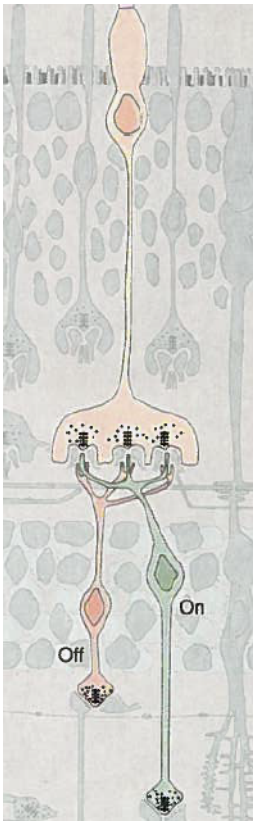

Figure 9: Schematic of ON and OFF midget bipolar cells connecting on pedicles of a cone. Source: Rodieck & Rodieck (1998, p. 52).

constitute vast neurosubstrate that is heavily involved in computing such RGCs features, such as local edge detection and direction selectivity (Rodieck & Rodieck, 1998).

For this thesis, it is important to highlight one specific type of amacrine cells, the starburst amacrine cell (SAC), named after its distinct shape (see Figure 10A). SACs are known to induce the direction-selective properties of DSGCs due to the highly specific dendritic connections they make onto DSGCs (discussed bellow).

3.5 Ganglion Cells

The output of the retinal pathway is conveyed to the brain by axons of ganglion cells. There are tens of different ganglion cell types, each having distinct connections with bipolar and amacrine cells. It is assumed that each type carry information about different visual features, extracted from its receptive field (Baden et al., 2016). However, these features do not solely arise due to the inner properties of retinal ganglion cells (RGCs), but due to their specific presynaptic neurocircuits. For instance, as noted above, DSGCs inherit their direction-selective property from SACs.

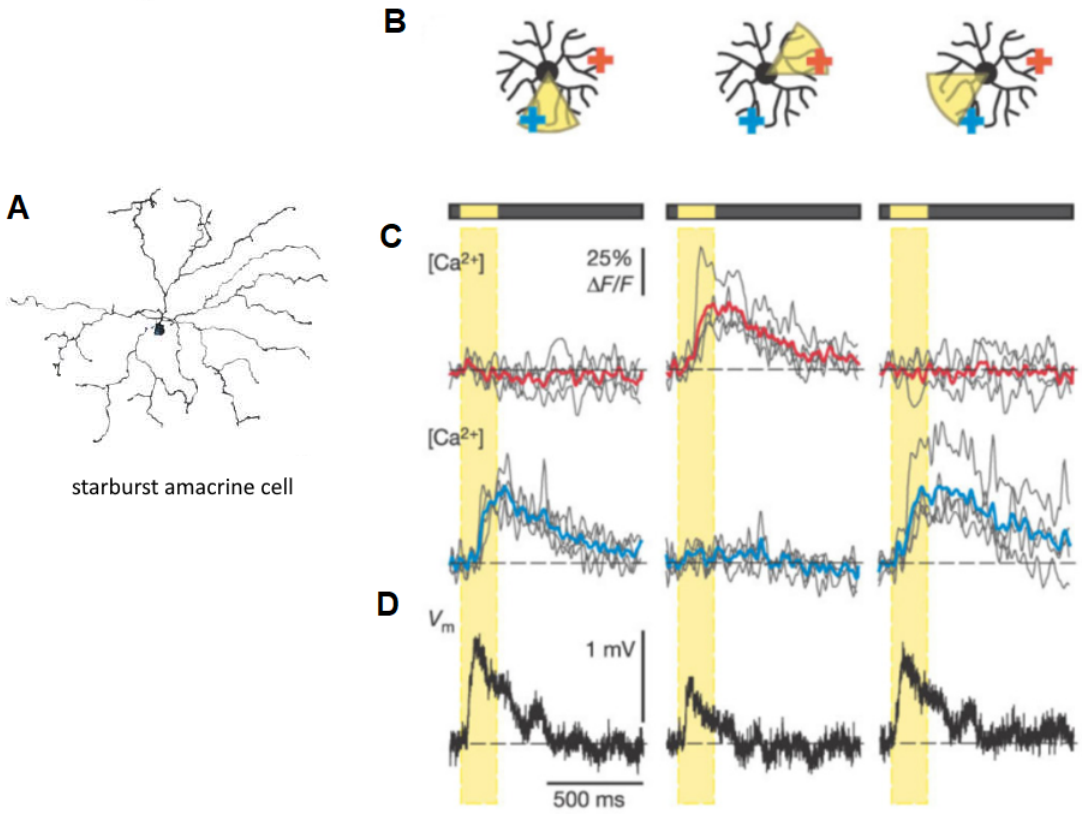

Figure 10: A: Morphology of a starburst amacrine cell. Source: Rodieck & Rodieck (1998, p. 53);
B: Local stimulation of SAC dendrites with 'pie-wedge'-shape stimulus elicits their immediate local calcium responses, which indicate release of neurotransmitter GABA. Note that the calcium response occurs only when the respective recording site (either red or blue cross with similarly color-coded calcium traces) is stimulated with light (yellow 'pie-wedge' section). In the instance on the left, only the blue stimulated site elicits calcium response. However, voltage recordings from the SAC soma exhibit responses regardless the stimulation location (D), indicating the SAC cell body is not direction selective per se. Source: Euler et al. (2002, fig. 2)

Direction-selective Ganglion Cells

The ability to detect movement is crucial for both spotting potential pray or predator and for providing feedback for the brain about its own movements. Therefore it is essential for daily survival and it would be the best if this feature was extracted in the neural pathway as early as possible. As it turned out, indeed it originates already in the retina, where significant part of RGCs is sensitive to motion swiping across their RFs only in a specific direction. The first ones to describe this feature were Barlow and Hill in the 1960s (Barlow & Hill, 1963). They discovered that by moving a small bright spot in a certain direction across RFs of RGCs they can elicit abrupt firing of some of the cells (hence called preferred direction or PD in short), but not when they moved the light in the opposite (null) direction. These cells where named

direction-selective retinal ganglion cells (DSGCs)

Similarly to other cells found in the retina, DSGCs can be further subdivided to many different subtypes. DSGCs can be segregated based on the following criteria:

1. **Response to light**
   Since retinal ganglion cells inherits this feature from bipolar cells, also DSGCs can be responsive only when light stimulus is on (ON DSGCs), or off (OFF DSGCs, also called J-RGC (Joesch & Meister, 2016)), or only to onset and offset of light, called ON-OFF direction-selective retinal ganglion cells (ooDSGCs).

   ON DSGCs can be yet subdivided into two groups based on their temporal dynamics: into *sustained ON* DSGCs, which stay active during the whole light stimulation, or *transient ON*, which stay active only during the onset of light stimulation.

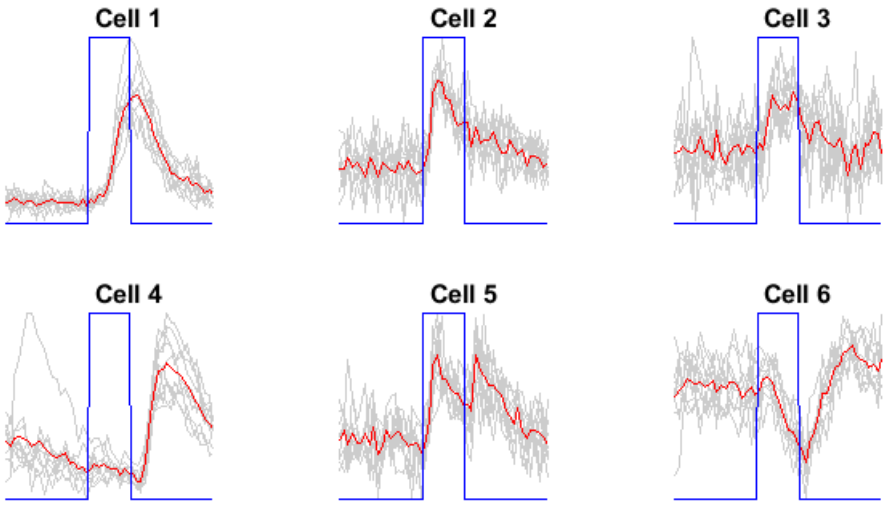

Figure 11: Illustration of light-dependend characteristics of DSGCs: blue line indicate stimulation with flash of light, red curve is a mean timecourse of 10 trails (light gray). Sustained ON cells (1 and supposedly 3), transient ON (2), ON-OFF (5) and OFF (4). Note that kinetics of cells can vary greatly (slow cells 1 and 4 vs relative quick 2 and 5). There are also more types of RGCs: take cell number 6, for instance, known as Suppressed-bycontrast (SbC) RGC.

   Perhaps for their abundance in the retina, the most intensively studied group of DSGCs is represented by the ooDSGCs. They were the first to be described by Barlow in 1963 and remained in the center of scientific attention ever since. Most of DSGCs intrinsic properties, that are later described, were explored in ooDSGCs, but it is most likely that similar mechanisms are employed in other DSGCs subtypes, too.

2. **Response to specific direction of motion**
   Barlow and Hill showed that there are four cardinal preferred directions of ooDSGCs: dor-

sal, ventral, nasal and temporal (see Figure 12). Later studies proved, that these cruciform orientation are not oriented haphazardly, but are actually aligned with the gravitational and body axes, as shown in Figure 13 (Sabbah et al., 2017).

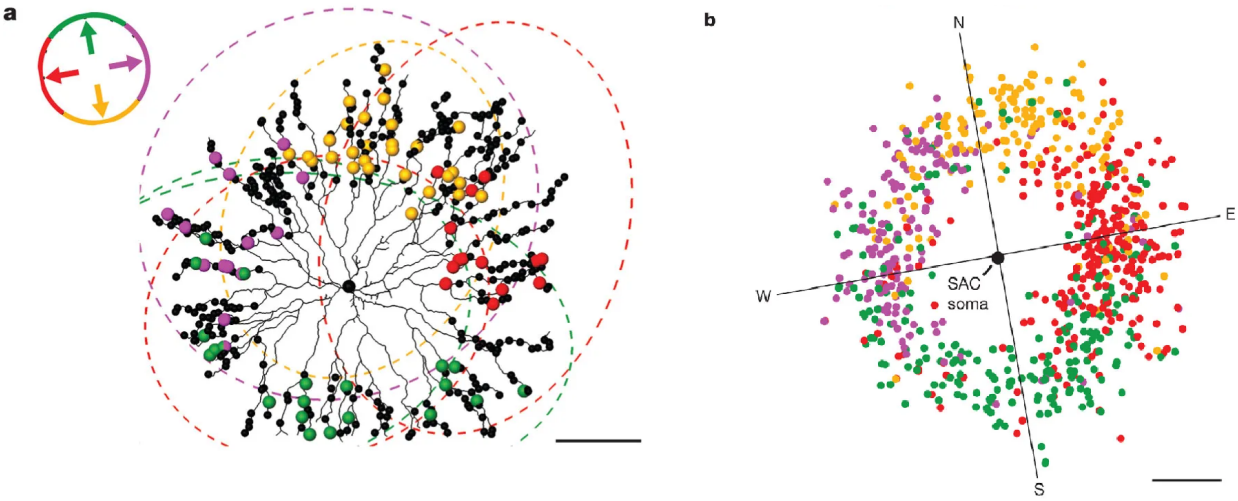

Figure 12: Highly specific connections from SACs onto DSGCs are presumably the major cause of direction-selective responses of DSGCs. A: an OFF SAC and its synapses (black dots) with ooDSGCs. Dendritic trees of adjacent ooDSGCs are depicted by dashed elipses; along with their synapses, they are color-coded by their preferred directions (top left). It is visible that ooDSGCs preferably make contacts with SAC dendrites oriented in the null direction. For instance, ooDSGCs with westward preferred direction tend to make connections with eastward-oriented dendrites of SACs. B: Postsynaptic locations of 24 ooDSGCs oriented respective to a SAC soma. Source: Briggman et al. (2011, fig. 4)

It has been shown that direction-selectivity of DSGCs is induced mainly due to inhibitory GABAergic effects that originate in presynaptic dendrites of SACs, which inhibit activity of DSGCs when a stimulus is moving in the null direction (Figure 12) (Euler et al., 2002). This finding is supported by other study in which SAC dendrites were ablated, abolishing the direction-selective responses of DSGCs (Yoshida et al., 2001). Interestingly, each SAC can wire onto multiple DSGCs and induce their direction-selective responses, since each SAC dendrite is direction-selective per se and works as an independent unit, depicted in Figure 10 (Briggman et al., 2011). When a stimulus is presented from a centrifugal direction, that is from center of a cell to its periphery, the SAC dendrite becomes active and inhibits the DSGC it connects onto. In this way, SAC dendrite responds best to the direction that is opposed to the preferred by of its postsynaptic DSGC (see Figure 14).

Additionally, also excitatory glutamatergic and cholinergic motifs that strengthen direction-selectivity in a push-pull manner (i.e. supporting bursting activity of DSGCs when stimulus moves in a preferred direction) were later described (Matsumoto et al., 2019)

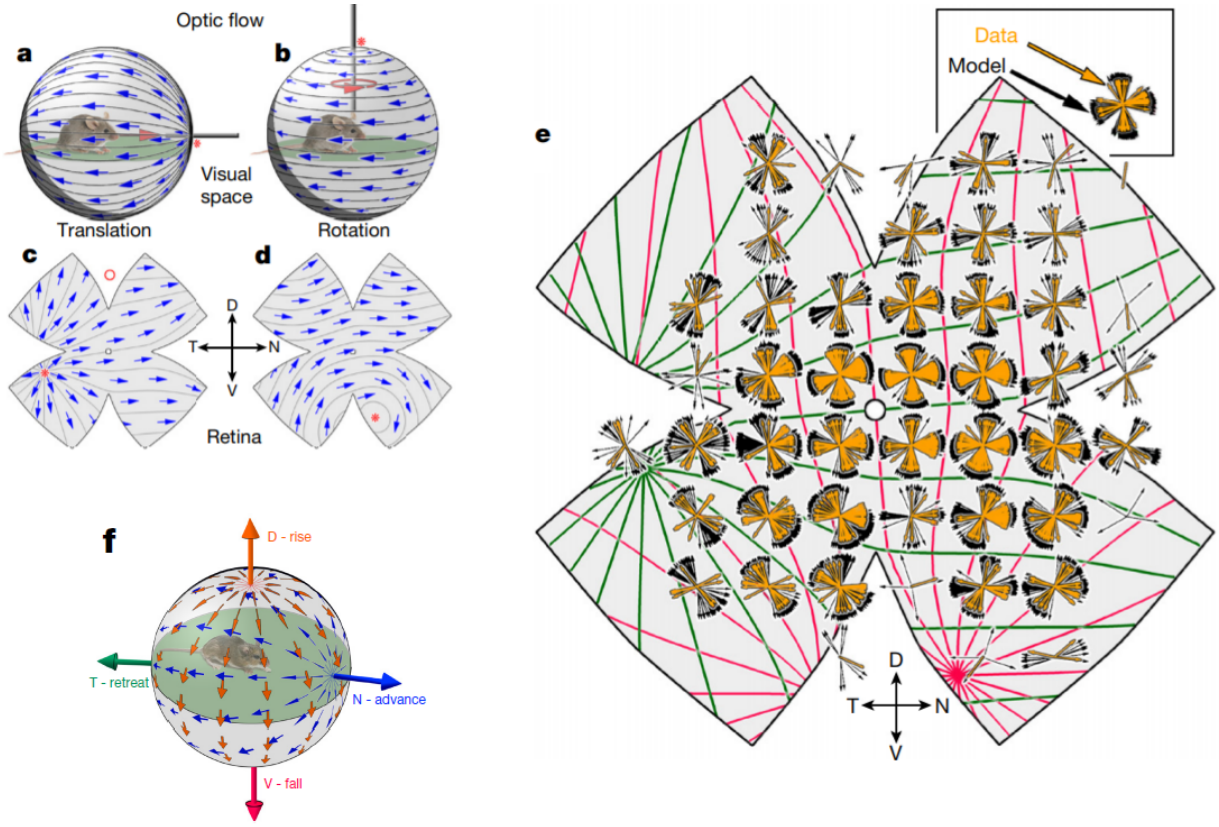

Figure 13: Interestingly, DSGCs are aligned with their PDs along the gravitational and body axes. When an animal runs or rotates (a, b) through an environment, it induces optic flow in the retina with respective flowfield poles (c, d). Respective four cardinal subtypes of DSGCs (here called D, V, N and T) are aligned with meridians of such flowfield poles to optimize the readout about the environment motion (e). In this way, selective firing of the four DSGCs subtypes can inform the brain about various global motions (f). For instance, if the animal moves forward it activates the same subtype (N DSGCs) in both eyes, whereas leftward rotation activates opposing subtypes (right eye, N; left eye, T). Source: Sabbah et al. (2017, fig. 1 & 4)

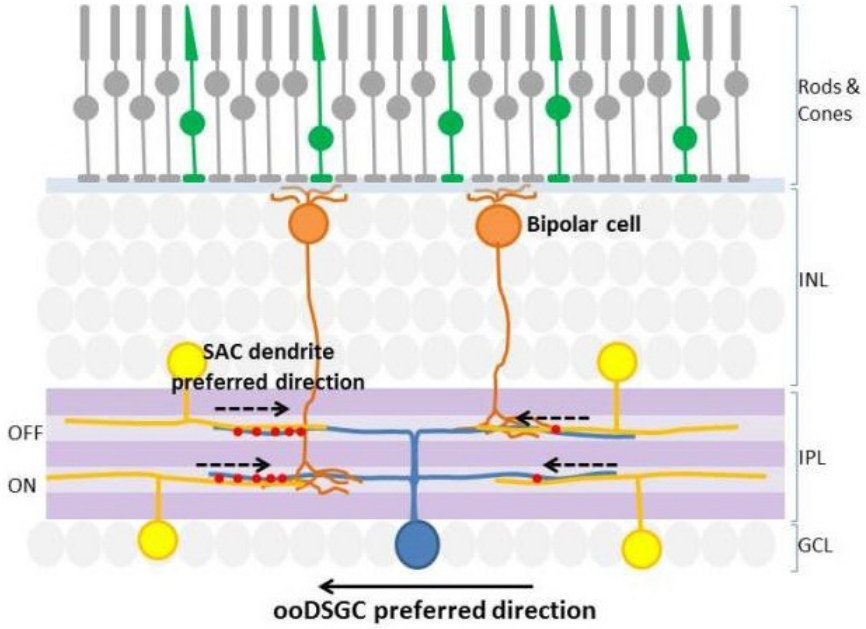

Figure 14: Illustration of direction-selective circuit in cross section of the retina: in blue is DSGC that prefers rightward direction, indicated by solid arrow. Preferred direction of SAC dendrites, on the other hand, is the opposite to that (dashed arrows) with numerous inhibitory GABA synapses along this axis (red dots). Source: Normann et al. (1999, fig. 1)

4 Detection of Neuronal Activity

Main objective of neuroscience is to explain how nervous system encodes and stores information by untangling wiring patterns of neurons, identifying new cell types and discovering means of their molecular communication (Obien et al., 2015). These tasks are addressed also thanks to the ever-evolving tools and methods in immunostaining, electrophysiology, and optics. Depending on the scale we want to investigate, we select the appropriate tools: from recording a single cell channel with patch clamp to electroencephalography recordings of the whole brain. Optimally, we would like to have the best possible resolution on the largest scale possible (whole brain), however, it is obvious that this task is impossible to reach.

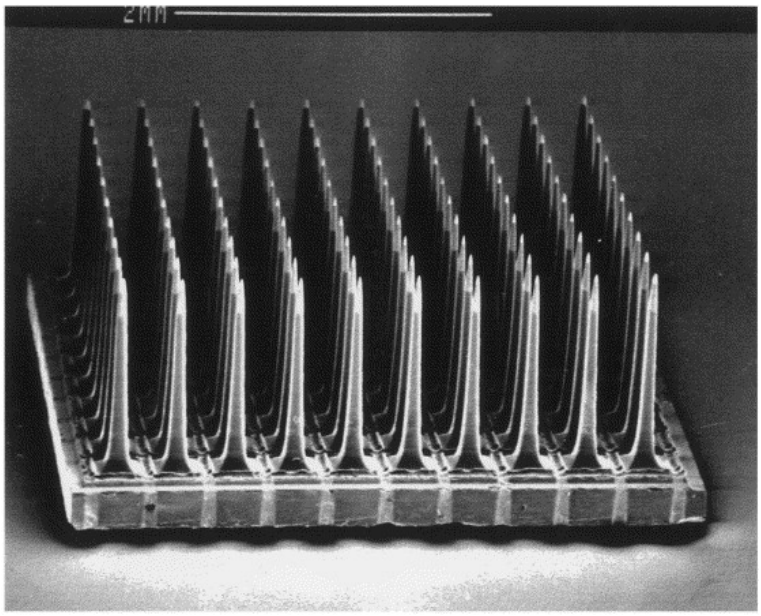

Figure 15: A scanning electron micrograph of a microelectrode array. Source: (Normann et al., 1999, fig. 1)

One way to record cell activity (whole cell recording) *in vivo* is via microelectrode, which often had to perturb membrane of the cell in question. This is not favourable, since we are physiologically affecting the investigated cell and thus interfering with its functional properties we want to look into. Moreover, another bias of using microelectrodes may arise from their incapibility of probing certain cells due to their unfavorable morphology, or weak electrical dipoles (Jercog et al., 2016). Still, this method is very used today thanks to the superb temporal resolution, minimal distortion of the signal and possibility of recording from a single membrane channel.

However, recording a group of adjacent cells becomes with this approach rather awkward and near-to-impossible to achieve. For this task, microelectrode arrays, that have recording sites of $200x200\mu m^2$, were developed. Microelectrode arrays can record signals from hundreds of cells with very good temporal resolution (in the order of kHz). On the other hand, such recordings take up enormous hard-drive memory and are computationally demanding. Moreover, they also suffer from detecting all possible unwanted signals that come from a surround of every sensor of the array, not necessarily from neurons.

Unlike microelectrodes or microarrays, combination of optical imaging and genetically encoded indicators enables concurrent tracking of thousands of neurons without any physical contacts with the cells, yielding more unbiased data and allowing more sophisticated analyses of neural population properties. Moreover, the genetically encoded reporter can respond not only to the changing voltage potential of cells, but to myriad different processes within the cells, such as vesicle releases, changes in neurotransmitter concentrations, or intracellular calcium dynamics (Lin & Schnitzer, 2016). Hence, the combination of optical microscopy and genetically encoded fluorescent indicators has become the favourite method in recording neural activity over the last two decades (Lin & Schnitzer, 2016).

4.1 Genetically Encoded Indicators of Neuronal Activity

Genetically encoded indicator is a protein that fluorescent upon light excitation of certain wavelength and concurrent occurrence of certain inner process of a cell that the indicator was designed to respond to. This biosynthetic indicator protein is not embedded into the cell by endocytosis or intracellular injection, as some synthetic dyes are, but rather by making the cell to express the protein on its own from a DNA/RNA vector it is enforced. In general, there are two ways of introducing genetic vectors to cells: either by infecting the cells with a virus containing the genetic information, or by transgenesis and breeding genetically mutated individuals.

Transgenic animals are easy-to-use, as they do not necessarily need any additional treatment. Moreover, some transgenic lines of animals can express the indicator on their own for their entire life and thus are more convenient for longitudinal studies. Their downside is that the biosensor expression can be lower compared to their virally infected peers, and that it may require to cross two or even three lines of transgenic animals to get the expression of the indicator in a specific cell-type we want to investigate. This can (a) be very expensive, costing several hundreds of euros per animal, and (b) can introduce certain peculiarities in behaviour of mice or functional differences in their neurons (Lin & Schnitzer, 2016).

Calcium Indicators

Genetically encoded calcium indicators (GECIs) are perhaps the most robust modality for optical imaging of neuronal activity that evolved a lot over the past years: from optimizing the strengths of photonic outputs to faster kinetics of the protein (i.e. increased temporal resolutions) and engineering a whole spectrum of indicating colors. Probably the most popular indicators nowadays are either GCaMPs, that use green fluorescent proteins (GFPs), or R-GECOs, that use red fluorescent proteins (RFPs).

Calcium indicators respond to cell activity indirectly: an action potential (AP) of a cell is associated with rapid influx of calcium ions, which in turn activate the indicator. Upon opening voltage-gated calcium channels during an AP, the intracellular concentration of calcium rises in cortical neurons $\sim$ 150 nM within 10 ms and persists with half decay time of 50 - 70 ms (Helmchen et al., 1997). Meanwhile, the duration of AP is usually one magnitude lower, $\sim$ 3 - 5 ms (Helmchen et al., 1997). This therefore constitutes major drawback of calcium imaging: its temporal resolution is limited by the slow kinetics of calcium.

On the other hand, a single localized AP can trigger a global and prolonged response of the indicator and thus amplifies the detectable photonic signal (Lin & Schnitzer, 2016).

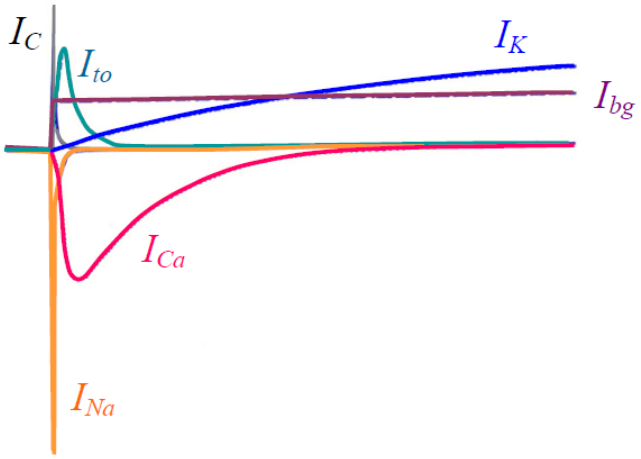

Figure 16: Decomposition of membrane current into individual ion fluxes upon AP. Influx of calcium into cell is depicted in red. Source: Simurda (2007, fig. 20)

4.2 Viral Delivery of Genetically Encoded Biosensors

Viral delivery of genetically encoded biosensors can be performed with a wide range of different viral vectors, depending on the specific feature of the vector we want to exploit. For instance,

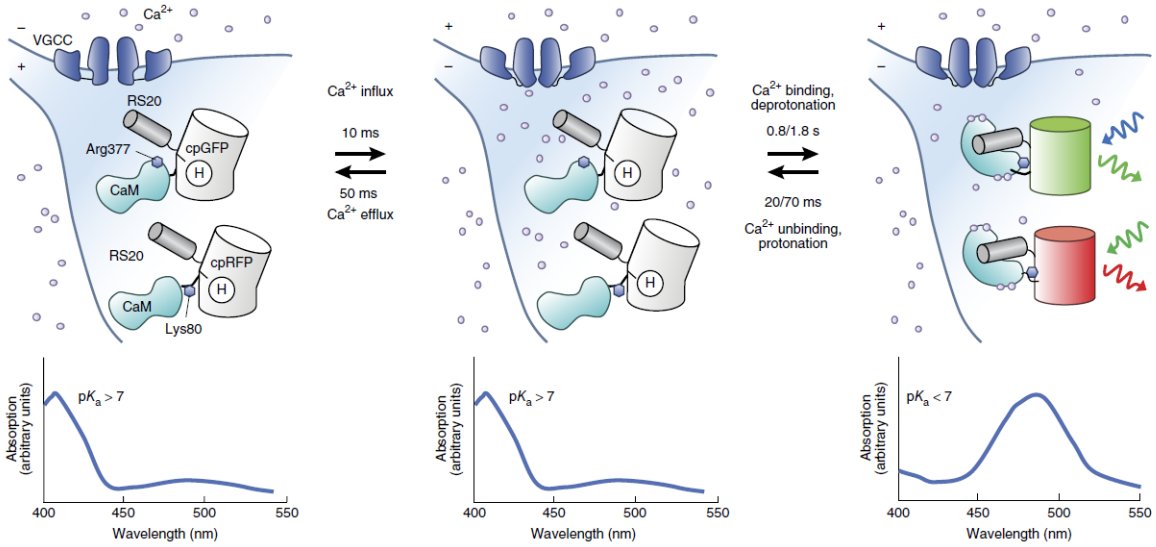

Figure 17: GECIs respond to increase of calcium concentration after AP and subsequent opening of voltage-gated calcium channel (VGCC), shown at the top. Calcium-induced binding of RS20 (a peptide from smooth-muscle myosin light-chain kinase) to a calmodulin (CaM) causes repositioning of Arg377 in GCaMPs and Lys80 in R-GECOs with subsequent deprotonization in their fluorescent proteins and absorbance shift (bottom) (Lin & Schnitzer, 2016). GCaMPs report APs with green fluorescent light upon excitation with blue light, R-GECOs with red light upon excitation with green light (afferent and efferent sinusodial arrows on the right). Source: Lin & Schnitzer (2016)

some vectors integrate themselves into the host genome and thus transcribe the introduced genetic vector forever. This can be useful for longitudinal studies. Other vectors, for instance, can transfect cells that are presynaptic or postsynaptic to the primarily infected cell. On the other hand, to not only praise the viral delivery of genetically encoded biosensors, we should also note that it can be difficult to obtain adequate and specific expression of the indicator protein only in the desired cell type and that the viral infection might not spread very far, being only localized to the immediate viral injection site. Moreover, many different viral classes and serotypes must be first tested for transduction efficiency and potential cell toxicity (Lin & Schnitzer, 2016).

One of the most popular vectors used in neuroscience are recombinant adeno-associated viruses (rAAVs). They are favoured for their non-pathogenecity, ability to maintain long-term gene expression and relatively big DNA packaging size of almost 5 kb (Lundstrom, 2018). To date, 13 different AAV serotypes and more than 100 variants have been isolated and used for gene delivery (Lundstrom, 2018). The most frequently used rAAV vectors in neuroscience are based on the serotype AAV2, the first serotype to be identified and characterized (Chai et al., 2019).

Viral vectors can be delivered to the retina in two ways: they can be injected either into the subretinal space (epiretinal injection), where they target mostly photoreceptors, or into to vitreous body of the eye (intravitreal injection), where they predominantly target inner neurons of the retina and RGCs (Euler et al., 2019). It has been shown that the transducted biosensor is expressed sufficiently after two weeks, which is a period that many studies use for imaging, before reaching expression plateau after 7 weeks (Natkunarajah et al., 2008).

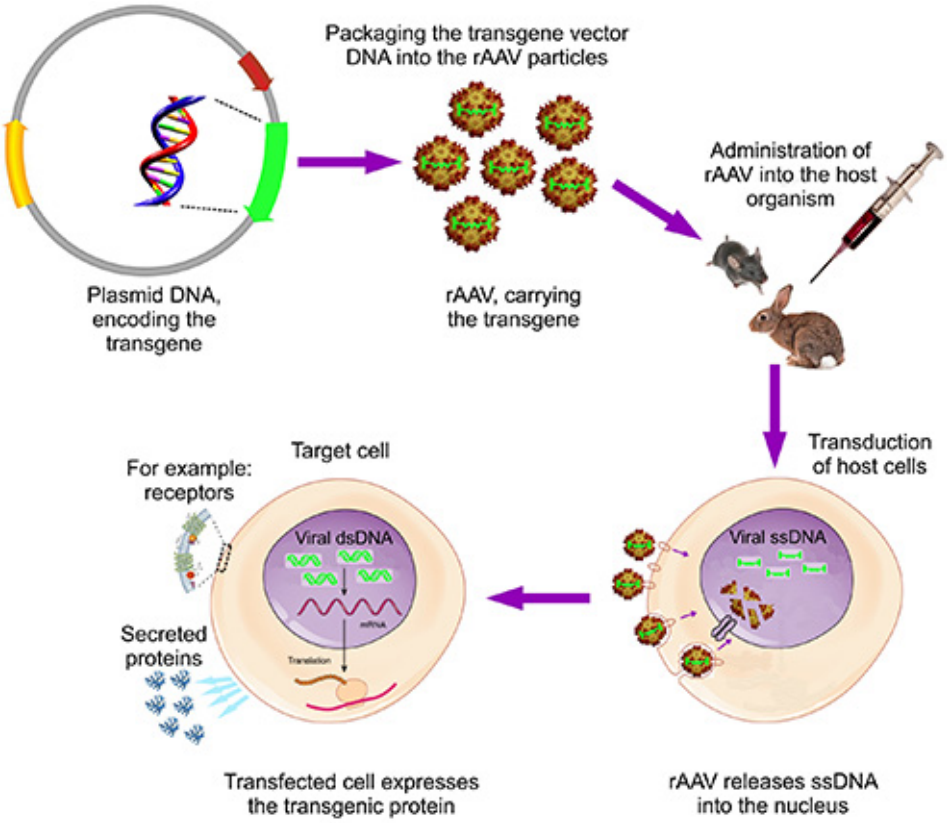

Figure 18: Viral delivery of biosensors: after engineering rAAVs by inserting DNA sequence of a desired biosensor to a DNA plasmid and encapsulating this transgene vector into rAAV particles, the rAAVs are injected into the host organism. There, they infect targeted cells and start to express the biosensor. Source: Biomedicum AAV Core Facility (2017)

4.3 Constrains of Optical Methods

Unlike other parts of the vertebrate nervous system, the retina is directly sensitive to light, and therefore using light microscopy inevitably leads to *unintended* activation of the retina. This *unintended* activity is superimposed on the purposely evoked *intended* activity we want to investigate, making them impossible to untangle (Euler et al., 2019). This can drastically curtail fidelity of the recorded neural activity. Hence, it is desirable to diminish this effect as much as possible.

For this reason studies on the retina conventionally employ two-photon (2P) microscopy, which, unlike one-photon (1P) microscopy, uses infrared-shifted excitation laser that is far from the peak absorbance sensitivity of photoreceptors and thus minimize their unintended activations (see again Figure 7). Along with very high resolution that allows studying neuronal activity of single synapses, 2P imaging became the standard and respected technique that has to date helped to shed light on intrinsic properties and complex synaptic interactions of many cell types in the retina (Borghuis et al., 2013; Duebel et al., 2006; Yonehara et al., 2013; Chen et al., 2016).

However, since 2P microscopy scans the image in a raster fashion, the FOV is constrained by maintaining sufficient temporal resolution, which for calcium imaging is $\sim$ 15 Hz, yielding FOV of $\sim$ 200 x 200 μm^2 with a few hundred detected cells at best. Moreover, there are three ways how unintended activation occurs in 2P imaging anyway:

Direct 1P excitation

The excitation light of 2P imaging is typically $\sim$ 910 nm, far beyond even the MWS opsin absorbance peak ($\sim$ 510 nm). In this sense, one would assume that it is unlikely for the individual photons to excite the retina. However, some photoreceptors are excited anyway, owing to the relatively high power of the excitation beam that is required for generating fluorescence signal and the fact that all opsins have a long, ultra-low sensitivity tail that goes far into the IR range (Figure 19) (Euler et al., 2019). As Euler estimated, direct 1P excitation, caused by a laser tuned to 930 nm and operating at a typical average power of 5 mW (in the tissue), is causing $\sim$ 18 activated rhodopsin (Rh*) molecules per rod per second ($Rh^* \cdot rod^1 \cdot s^1$) (Euler et al., 2009).

Direct 2P excitation

Recombination of two IR photons can also occur in photoreceptor instead of fluorescent probe. Since excitation probability falls with the fourth power with increasing distance from the focal plane of the microscope, it might appear that the probability of direct 2P excitation is very low (Euler et al., 2019). Yet, due to amplification mechanism of phototransduction cascade and high opsin concentration (mouse rods contain $\sim 7 \times 10^7$ of rhodopsin molecules) in photoreceptors, which per se densely populate the retina, even sporadic 2P excitation of opsins can lead to a substantial laser-induced activation of the retina (Euler et al., 2019; Denk & Detwiler, 1999). According to Euler estimations, direct 2p excitation constitutes the largest portion of the artificially induced activity, accounting for $\sim 21 \times 10^3$ activated rhodopsin (Rh*) molecules per rod per second $Rh^* \cdot rod^{-1} \cdot s^{-1}$ (Euler et al., 2009).

Indirect excitation

Last unintended activation stems from photons that are emitted by fluorescent probe, or any inherent autofluorescent protein in the tissue, and scattered towards photoreceptors. This effect is expected to be on the range of that for direct 1P excitation (Euler et al., 2019).

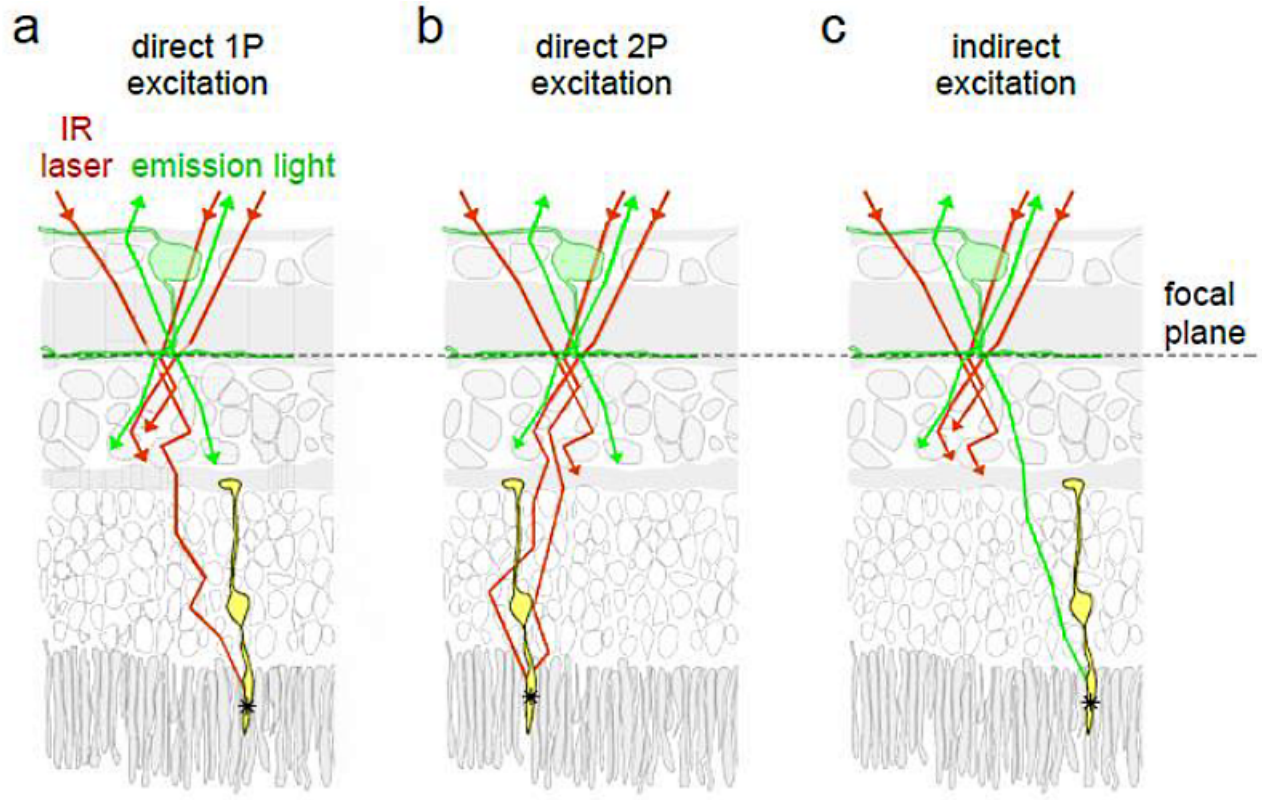

Figure 19: Means of direct and indirect excitaion of photoreceptors. Note that here the retina is inversely oriented, with photoreceptors at the bottom. Source: Euler et al. (2019, fig. 2)

5 Novel One-photon Fluorescence Microscopy Method

With the development of red-shifted fluorescent proteins, such as the family of indicators derived from R-GECOs, new possibility in optical imaging of the retina emerges: since 1P microscopy is free of false 2P activations and uses significantly lower power of excitation light compared to 2p microscopy at the same time, the magnitude of unintended activation of the retina introduced by 1P imaging is low enough to yield recordings with good signal-to-noise ratio. Although this method may not be applicable to retinae of all vertebrates, it is good enough for laboratory mice which have UV-shifted opsins (Figure 7) and their sensitivity to red light, which supplies energy to the fluorescent proteins, is relatively low.

The biggest benefit of using 1P microscopy, except of cost and general simplicity, comes in enormous FOV that 1P imaging offers: since 1P microscopy does not scan the specimen in a raster fashion, its FOV is no longer constrained, yielding the FOV $\sim$ 40-times larger compared to FOV of 2P microscopy. This enables us to record simultaneously activity of thousands of RGCs and explore their population properties across the retinal space much easily and in much greater detail than any study ever before.

5.1 Microscope Setup

Simplified schematic of the microscope setup is depicted in Figure 20. Starting at bottom right, a visual stimulus, designed and rendered in Psychophysics Toolbox Version 3, is projected onto the retina from a projector, in which blue LED was changed for UV LED to better adjust to mouse opsins' spectral distribution. Red light is from the stimulus diverted away with dichroic mirror right at the beginning, since (1) red light would cause stimulus leakage (we want to see the activity of cells that emit red light, not the projected stimulus per se) and (2) the red light serves as a synchronizing clock for the camera. The remaining UV-greenish stimulus is then focused on the photoreceptor layer of the retina.

To keep the retina alive, it is perfused with oxygenated HEPES-buffered Ringer's solution, which supplies nutrients to the retina. Simultaneously, the retina is illuminated with red excitation light (580 $\pm$ 10 nm) to provide energy for the genetically encoded biosensors.

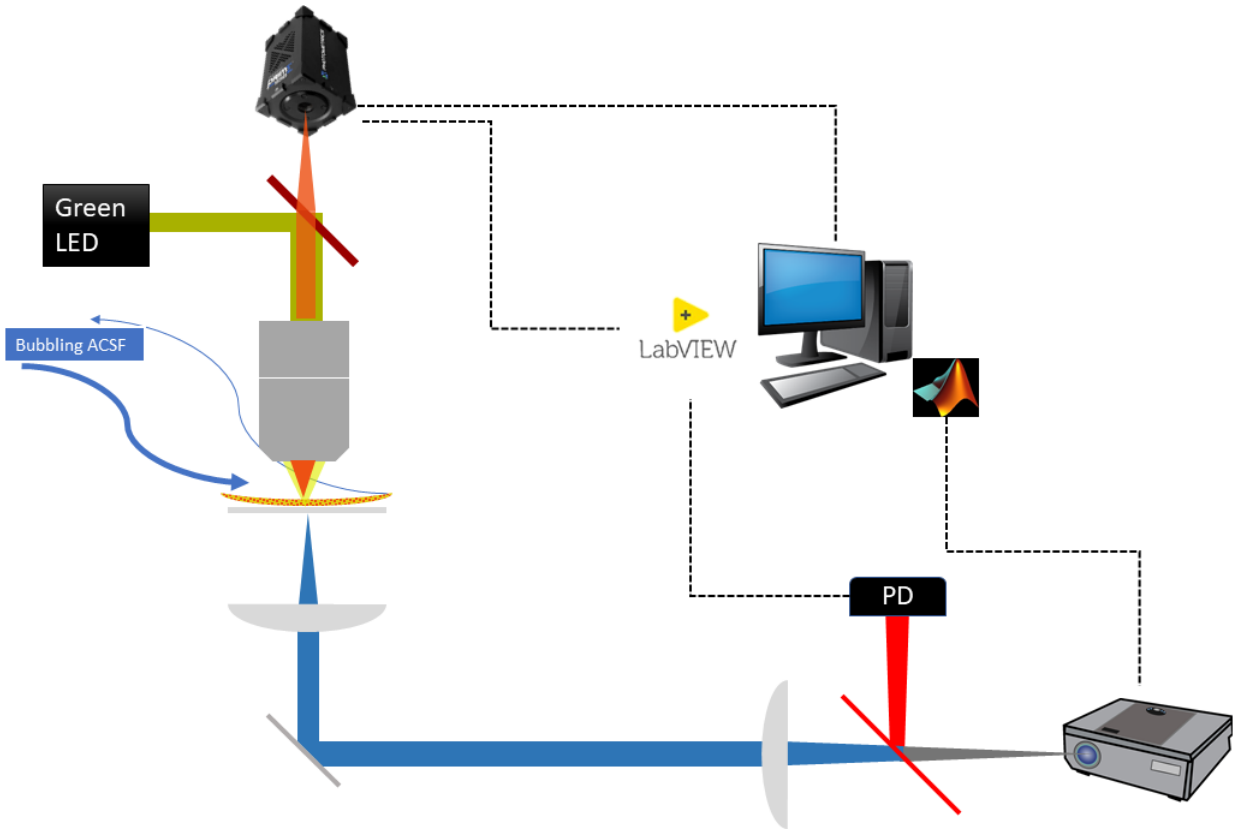

Figure 20: Schematic of microscope setup; courtesy of Divyansh Gupta

The outcoming fluorescent light, which indicate activity of neurons, travels through long-pass filter only to be registered in a ultra-sensitive camera (Photometrics PRIME 95B, recorded with 10 fps), shown at the top left of the schematic. Acquired images are saved to the controlling computer along with timing of projected stimuli frames and photodiode signal of the diverted red light coming from the projector. Together, they are used for time synchronization. In this way, we know what stimulus frame was presented at given microscope snapshot.

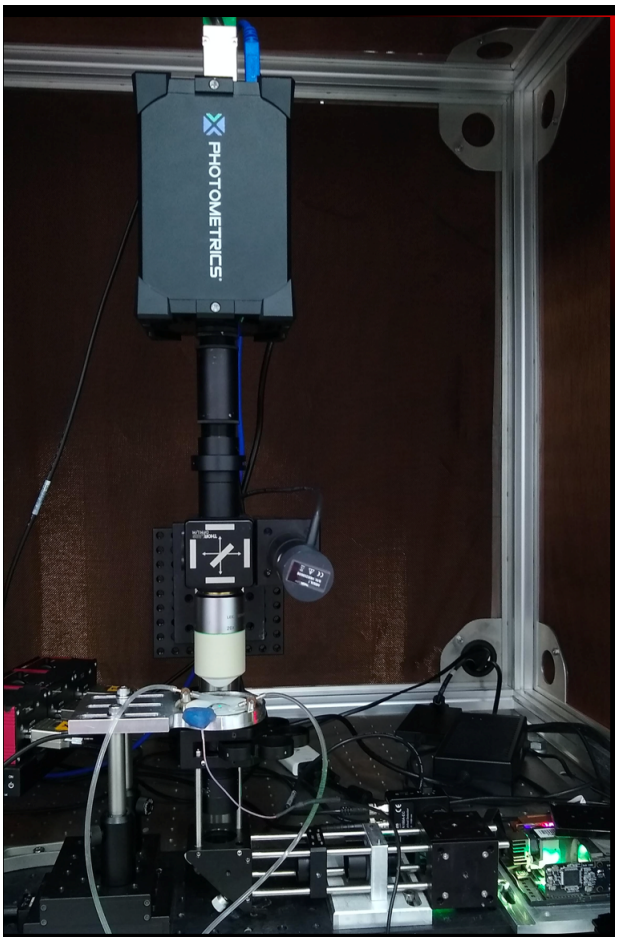

Figure 21: Microscope setup. The camera is ultrasensitive to light and hence, the entire setup has to be obscured from any external light. Courtesy of Divyansh Gupta

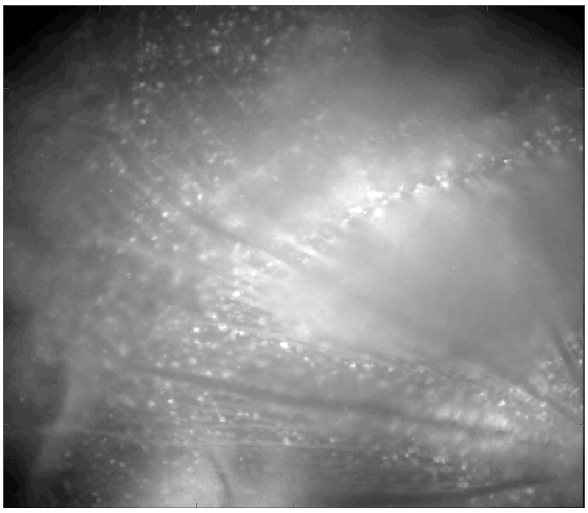

Figure 22: Example of acquired image from our setup. Each experiment yields ten of thousands of images. Here, the individual cells are the small bright dots.

6 Experimental Procedures

All of the subjected mice were *wild-type* (WT) from strain *C57BL/6J* (The Jackson Laboratory). All of them were intravitreally injected with rAAVs inducing expression of the red-shifted calcium indicators: either *AAV2.9.Syn.NES.jRCaMP1a.WPRE.SV40* or *AAV-dJ-hSyn-CAR-GECO1*. Sulforhodamine B was coinjected in the ratio of 1:2 with rAAVs to check whether the intravitreal injection was administered correctly.

For some mice, D-mannitol or Dexamethasone were additionally applied to test whether they facilitate viral infection of the administered rAAVs. D-mannitol was injected intravitreally, one hour before the rAAVs were applied. Dexamethasone was injected either in the same manner or intraperitoneally, one day before the rAAVs.

6.1 Intravitreal Injections

Intravitreal injections can be administered either with glass micropipette or metal needles (Hamilton syringe). In both cases the injection route can be either the intersection of cornea and sclera or through a bit lower, just through sclera (Venkatesh et al., 2013). For this thesis, $\sim 2\ \mu l$ of AAVs per eye were administered to 6-8 weeks old mice using a hand-held 33-gauge Hamilton syringe.

Protocol

1. Mouse is anesthetized with mixture of ketamine, xylazine and saline in ratio 5:2:25 with 70 μl per 10g of body mass.
2. After the mouse is unconscious and does not twitch when its tail is pinched, it is positioned under microscope with the eye to be injected facing upward.
3. A small hole at the margin of the sclera and cornea is poked with a 30-gauge needle to help Hamilton syringe to enter the vitreous body of the eye (Hamilton syringe has a blunt needle tip).
4. Hamilton syringe is inserted to into the hole and $\sim 2\ \mu l$ of vitreous is drawn out.
5. Hamilton syringe loaded with rAAV (or adjuvants) is inserted into the hole with the tip behind the lens, roughly in the central part of the eye (see Figure 23). The tip should not be inserted too deep, since it could damage the retina on the contralateral side.

6. Virus is injected into the eye and after a $\sim$ 10s pause the Hamilton syringe is slowly pulled out.

7. Before the animal is put back to its cage, eye cream is applied on its eyes to prevent them from drying out and developing cataract.

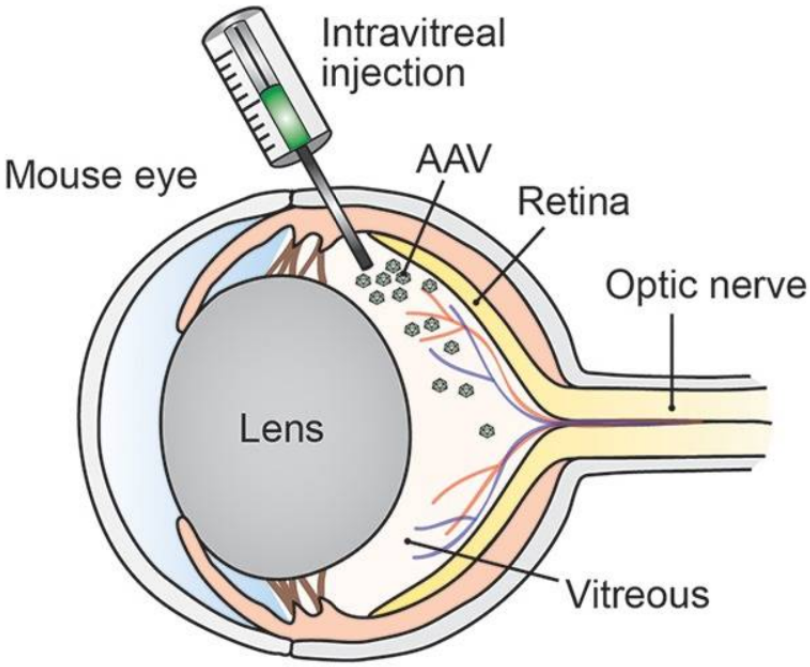

Figure 23: Illustration of intravitreal injection. Source: Looser et al. (2018, fig. 1, edited)

6.2 Potential Adjuvants Enhancing Viral Infections

The efficiency of the rAAV infection rate and thus the rate of gene transfer heavily depends on the chosen rAAV serotype. Some are highly efficient in infecting the cells of interest, others hardly infect any target cells. Moreover, the infection spread is often limited to the immediate injection site (Mastakov et al., 2001). To prevent this, injection has to be applied with optimal speed to achieve a global transduction. To facilitate the transduction rate even more, a number of studies tried combining injecting rAAVs with certain adjuvants, namely with D-mannitol or dexamethasone (Mastakov et al., 2001; Ghodsi et al., 1999; Nishimura et al., 1998; Kwak & D'Amico, 1992; Chai et al., 2019).

D-mannitol

Several studies have shown that co-infusion of D-mannitol with rAAV leads to increased gene transfer in the brain parenchyma (Ghodsi et al., 1999; Nishimura et al., 1998). The hypothesis is that after inducing systematic hyperosmolarity, caused by intracarotid administration of D-mannitol, capillary endothelial cells that form blood-brain barrier shrink, temporally opening tight junctions and thus allowing the rAAVs to enter the perivascular space (Nishimura et al., 1998). In addition, the direct adenovirus transfer into the brain parenchyma with hypertonic D-mannitol may shrink non-neuronal cells that block the viral accessibility to neurons (Nishimura et al., 1998).

Since intravitreally administered rAAVs do not need to cross the blood-brain barrier, only the second assumption, that hypertonic D-mannitol shrinks non-neuronal cells which prevent the virus from entering neurons, is applicable for our experiment.

To test the effect of D-mannitol, rAAVs were suspended in 10 $\%$ D-mannitol. The total volume of the injected solution was $\sim$ 2 μl, consisting of rAAVs, D-mannitol and sulforhodamine B in the ratio of 5:4:3, co-injected according to the protocol described above.

Dexamethasone

Other popular adjuvant that enhances viral infection is dexamethasone, a type of glucocorticoid medication which have been commonly used in clinic for its anti-inflammatory and immunosuppressive effects (Chai et al., 2019). It has been shown that after intracranial or intravitreal administration, dexamethasone inhibits activity of microglia and Müller cells, and thus impairs the active immune defense of neurons and possibly suppresses mechanisms for infection control (Herber et al., 2004; Kwak & D'Amico, 1992).

Table 2: Summary of tested viruses and adjuvants. IV = Intravitreally; IP = Intraperitoneally

Virus	Mice	Adjuvant	Adjuvant note
AAV2.9.Syn.NES.jRCaMP1a.WPRE.SV40	2	-	-
AAV-dJ-hSyn-CAR-GECO1	3	-	-
AAV-dJ-hSyn-CAR-GECO1	3	D-Mannitol	10 $\%$ with rAAVs
AAV-dJ-hSyn-CAR-GECO1	3	Dexamethasone	IV, pre 1h
AAV-dJ-hSyn-CAR-GECO1	3	Dexamethasone	IP, pre 24h

Dexamethasone was administered intravitreally to 3 mice, 1 hour prior to the rAAV injection with $\sim$ 1.5 μg of dexamethasone per eye, and to 3 mice intraperitoneally, 1 day prior to the rAAV injection, with 5 μl of dexamethasone solution (0.25 mg of dexamethasone on 1 ml of water) per 1 g of body weight.

6.3 Dissection of Wholemount Retina

There are a few good practice points that should be taken into account for every dissection procedure to obtain a responsive and usable retinal explant:

First, before the dissection procedure, the mouse has to be habituated in dark for at least 2 hours. The whole procedure, from euthanizing the animal till fixation of the retinal explant on a cover glass should be done as soon as possible, at least under 10 minutes. Next, the retina should be touched as little as possible, as every physical contact destroys the tissue and make the cells unresponsive. Lastly, it is good to add a few drops of oxygenated HEPES-buffered Ringer's solution to the retinal explant during the dissection procedure to keep it alive.

Protocol

1. After the mouse is euthanized by cervical dislocation, its eyes are enucleated and glued on a Petri dish with the eyes looking up.
2. Oxygenated HEPES-buffered Ringer's solution is applied on the enucleated eyes with a droplet to keep them nourished.
3. The cornea is removed by cutting in a circular path along the *ora serrata* with small scissors, while holding the eye at limbus with forceps.
4. The lens is pulled out with forceps along with floaters, resting in the vitreous body.
5. The eyecup with retinal pigment epithelium is gently torn apart from the retina, leaving the retina floating naked in the Ringer's solution.
6. Four equidistant incisions are made to the retina with small scissors.
7. The retinal explant is placed on a round cover glass and flattened with forceps while the excessive Ringer's solution is sucked out with a tissue. The retina then looks like a four-petal flower (see the final step in figure 24).
8. Round filter paper with a window in the middle is placed on the flat retina and glued to the cover glass with vaseline to fixate it.

6.4 Visual Stimulation

Visual stimuli, synthesized using Psychophysics Toolbox under Matlab (The MathWorks), were projected with TI DLP® LightCrafter™ 4500 (with 60 fps) and focused onto photoreceptor outer segments. The resolution of the projector was 1280 x 800 pixels with each pixel covering 2.25 x 2.25 μm^2 of the retina. RGB channels were set to (255, 37, 130) to adapt to spectra of mouse opsins.

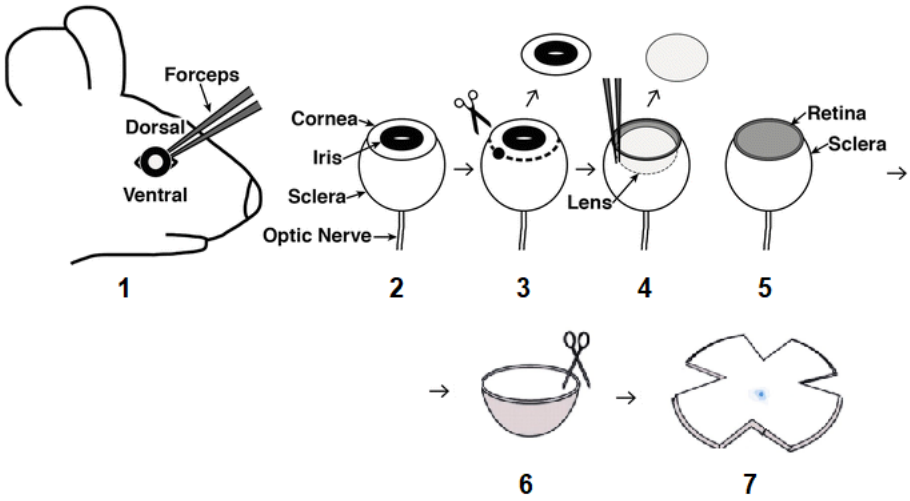

Figure 24: Schematic of the main steps of wholemount retitinal dissection: after the animal is euthanized, its eyes are enucleated (1), the eye is cut open along the *ora serrata* (3) and the lens is taken out (4), then the retina is detached from the eyecup and four cruciform incisions are made (6) to unfold the retina (7). Source: (Simmons & Fuerst, 2018; Jin et al., 2003, edited)

6.4.1 Receptive Field Stimuli

Remember from the previous chapters that each RGC responds to either increase (ON cell) or decrease (OFF cell) of light intensity in a particular visual space, called receptive field (RF). To probe these characteristics, we designed a checkerboard which is randomly generated every 5th frame (projector has 60 fps).

Conventionally, the size of the checkers is set to be $\sim$ 90 μm^2, which approximately corresponds to the RF span of RGC. In addition, we designed one checkerboard with half the checker size, with potential 4-fold increase of the RF resolution, and one with the same size, but with additional random shift of the checkerboard between each frame. Magnitude of this shift corresponds to the 1/10 size of the checker (i.e 9 μm), resulting in potential 100-fold increase of the RF resolution.

Table 3: Summary of RF checkerboards properties

Checker pixel size [μm]	**Random shift**	**Duration [s]**
90	no	300
90	yes	300
45	no	400

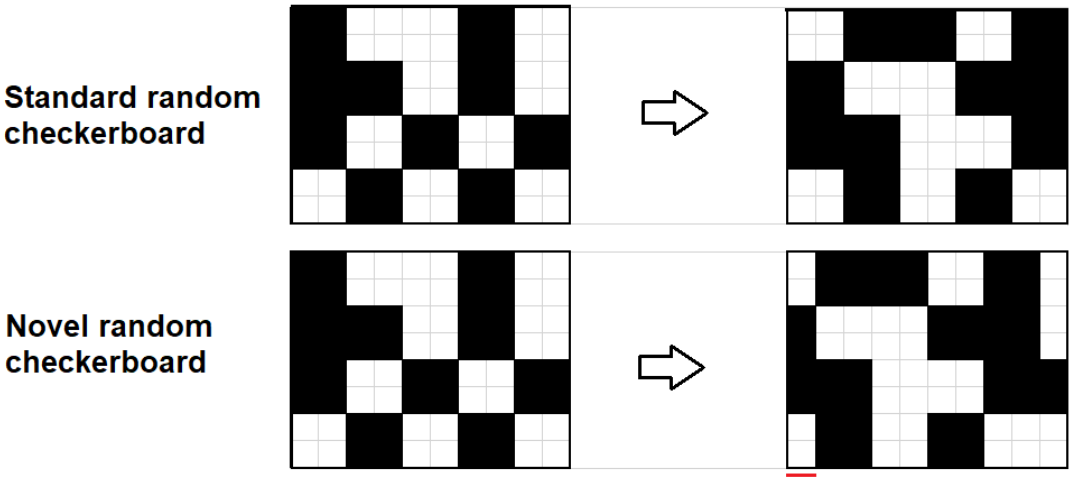

Figure 25: Illustration how novel random checkerboard stimulus works. Whereas conventional checkerboard, showed at the top, is generated in the unvarying grid (i.e a set of pixels can be only black or white), the novel approach shifts this grid inbetween the frames. In the example shown here, the frame is shifted one pixel to the left. In this way, the receotive field of the cell is mapped at much higher resolution.

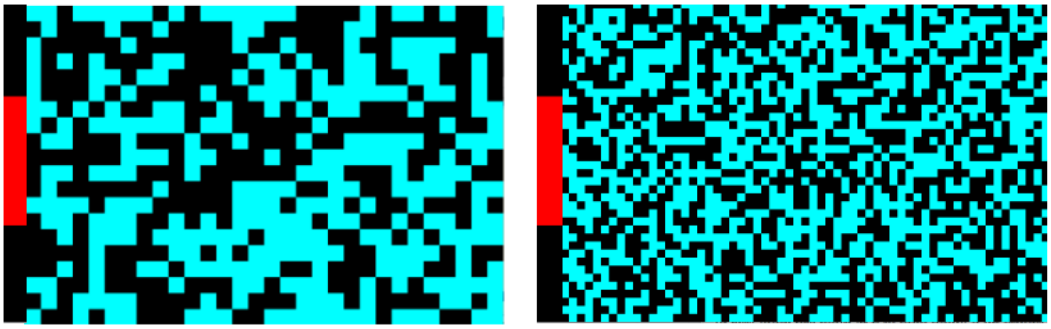

Figure 26: Illustration of random checkerboards devised for probing RFs of RGCs: on the left is presented conventional checkerboard with $\sim$ 90x90 μm^2 size of each checker, on the right checkerboard with half the checker size. The red bar on the left is used for synchronization with camera as described in the previous chapter.

6.4.2 Direction Selective Stimuli

To probe the direction-selectivity of RGCs, in total three different stimuli designs were developed: single moving bar, grating and moving checkerboard. Each stimulus swiped across the screen in a randomized sequence of 8 equidistant directions. This sequence was repeated 5 times to acquire the mean neuron response.

Moving Bars

Three moving bars were developed, differing in the speed of motion and width of the bar. The faster the bar was moving, the wider it was. With this approach, the bars illuminated any neuron in the retina for exactly 2 seconds.

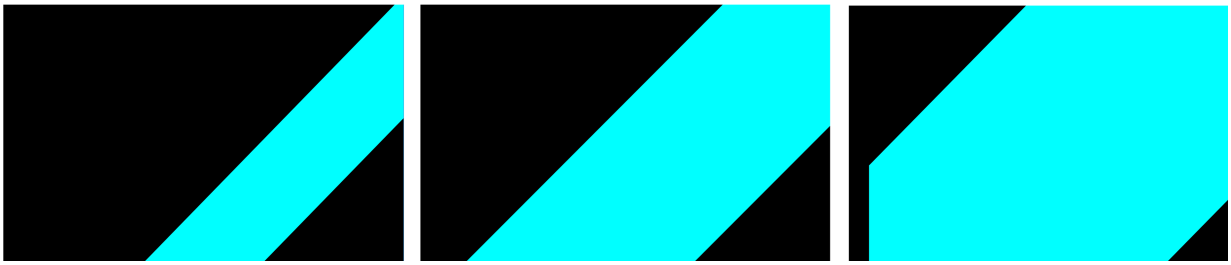

Figure 27: Illustration of moving bars stimuli. Left: 300 $\mu m/s$, 600 μm wide; Center: 562 $\mu m/s$, 1125 μm wide; Right: 990 $\mu m/s$, 1980 μm wide.

Grating

Grating was devised as a sinusodial wave with each cycle having 250 μm (125 μm per stripe) moving 500 $\mu m/s$ for 2 seconds (four cycles in total per direction).

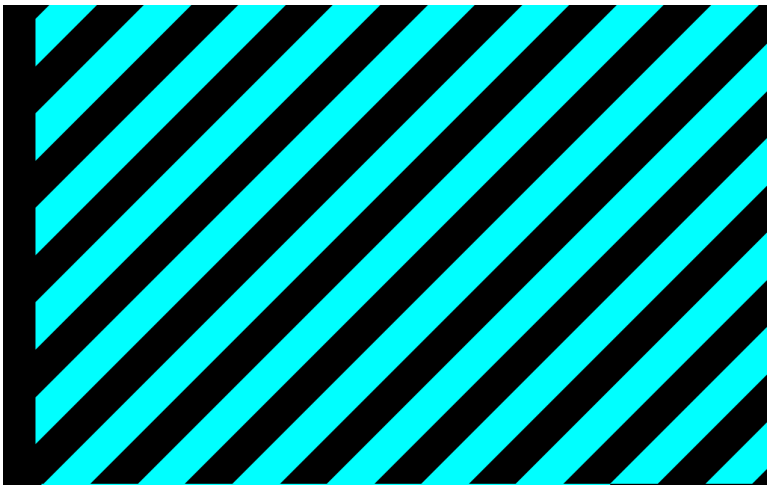

Figure 28: Illustration of grating stimulus. Width of each stripe was 125 μm with speed of 500 $\mu m/s$.

Moving checkerboard

Last artificial stimulus to probe the direction-selectivity of RGCs was a checkerboard with the size of each checker having 90 x 90 μm^2. The checkerboard moved with the same speeds as bar stimuli: 300 $\mu m/s$, 562 $\mu m/s$ or 990 $\mu m/s$, and with 8 equidistant directions per speed and 5 total repetitions.

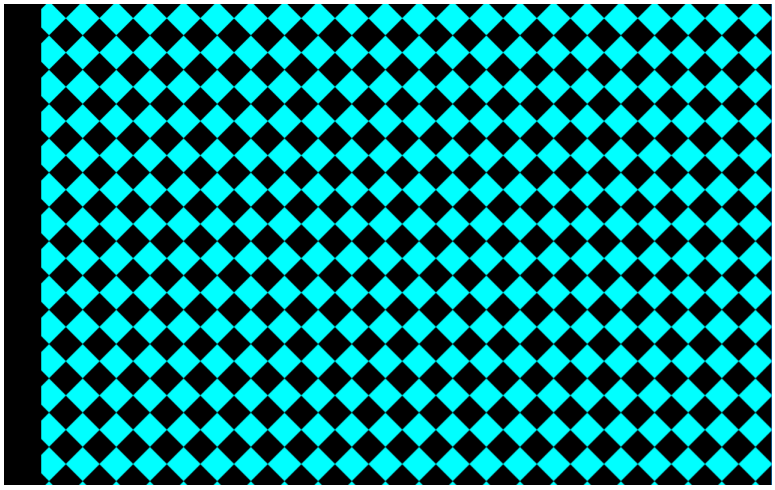

Figure 29: Illustration of moving checkerboard stimulus. The speeds were 300 $\mu m/s$, 562 $\mu m/s$ or 990 $\mu m/s$, with 8 equidistant directions per speed and 5 total repetitions; the checkers were always oriented with the edges moving perpendicular to the axis of motion.

Moving natural stimuli

In addition to the artificial stimuli described above, we designed also three natural stimuli. These stimuli were photos of natural scenes: a forest, grass and pebbles. Similarly to the moving checkerboard stimulus, enlarged window displaying part of the images moved across the images with the same speeds (300 $\mu m/s$, 562 $\mu m/s$ or 990 $\mu m/s$) and with 8 equidistant directions per speed and 5 total repetitions.

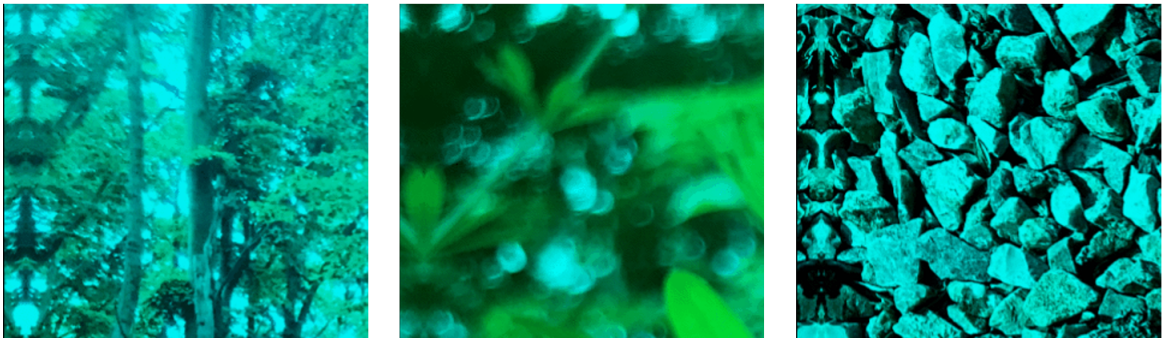

Figure 30: Illustration of moving natural stimuli. Windows were drifting across natural images with 300 $\mu m/s$, 562 $\mu m/s$ or 990 $\mu m/s$, with 8 equidistant directions per speed and 5 total repetitions.

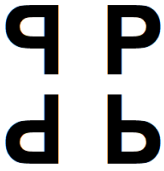

Figure 31: Before the images of natural scenes were presented in the shades of UV and green light, they were mirrored horizontally and vertically to ensure no abrupt changes happened in optic flow when presented window drifted out of the image. Here illustrated with the later 'P'.

6.5 Extraction of Neuronal Activity data

After the experiment is done, acquired sets of thousands of TIFF images need to be first transformed to more convenient data format of neuronal activity. The neuronal activity corresponds to the fluorescence of the cells: the more active the cell is, the more fluorescent light it produces.

Registration of the images along with detection of neurons and extraction of their activity is done with Suite2P image processing pipeline, run under Python. This preprocessing step is computationally demanding, taking even a few days to complete.

Fluorescence of the cells is then normalized as follows:

$$\frac{\Delta F}{F} = \frac{F - F_0}{F_0}, \tag{1}$$

with F_0 being the fluorescence baseline, calculated as median of weighted neuropil fluorescence in a sliding temporal window.

6.6 Computation of Receptive Fields

Computation of receptive field is relatively straightforward: after correlating cell activity with presented checkerboard for enough time, its receptive field emerges. This method, commonly known as spike-triggered average (STA), is nicely explained in Figure 33.

We computed the RF inversely from the perspective of the presented checkerboard. In this way, each presented random checkerboard pattern was correlated with cell activity in a given time window and such windows were subsequently averaged together. This approach is easier to implement than the conventional method and the outcome is the same.

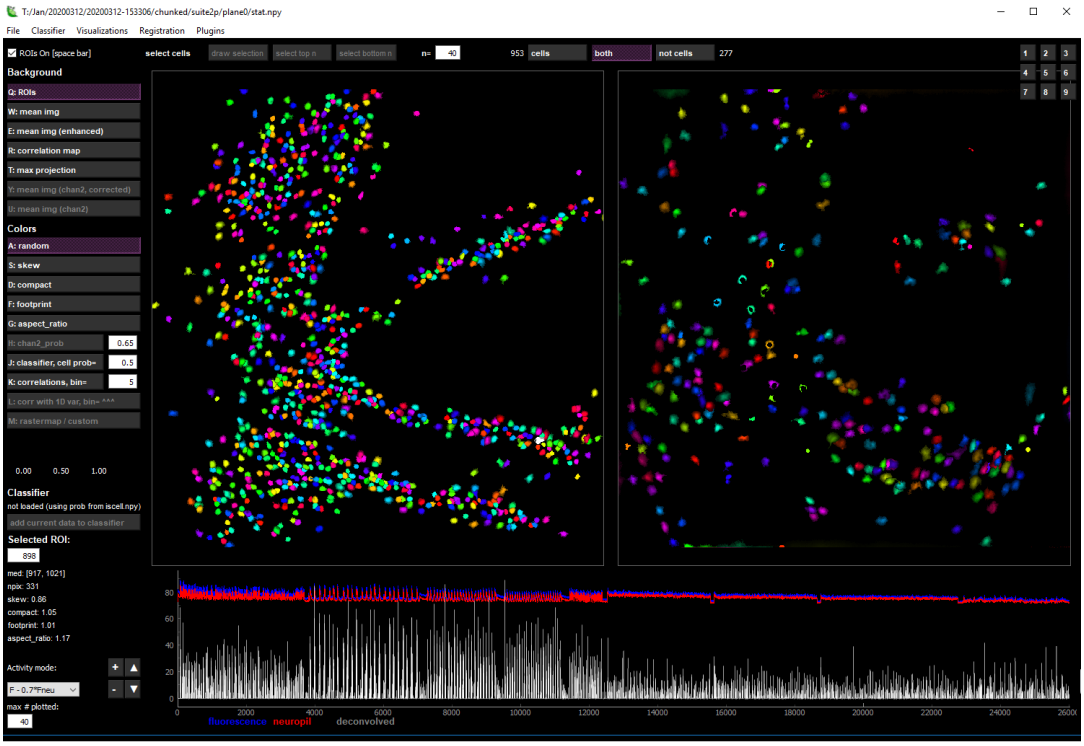

Figure 32: Detected cells and their neuronal activity traces (same FOV as in Figure 22). On the left side of the screen are randomly color-coded detected cells (n = 953) with their convoluted activity signal in red at the bottom. On the right screen are putative non-cells objects (n = 277).

```
parfor i = neurons %parallel processing
    fprintf("Mapping RF for neuron %d\n", i);
    for frame = 1:stim.opt.update_each_nth_frame:floor(size(stim.pattern,4))
        t0 = stim.opt.Frameinfo.frametime(frame);
        if isnan(t0); break; end
        stimulus = double(stim.pattern(:,:,:,frame)/255);
        stimulus = reshape(stimulus, 1, size(stimulus, 1), size(stimulus,2),
            size(stimulus, 3));
        for filter_pos = 1:numlat
            response_pos = rp(frame, filter_pos);
            if isnan(response_pos); continue; end;
            weight = response(i, response_pos);
            weighted_stim = stimulus*weight;
            filter(i,:,:,:,filter_pos) = filter(i,:,:,:,filter_pos) +
                weighted_stim;
        end
    end
end
delete(gcp('nocreate')); %end parallel processing
```

Code 1: Computing of RFs. For each cell, every random checker is weighted by the cell fluorescence response. Since this computation is demanding, neurons are processed in parallel.

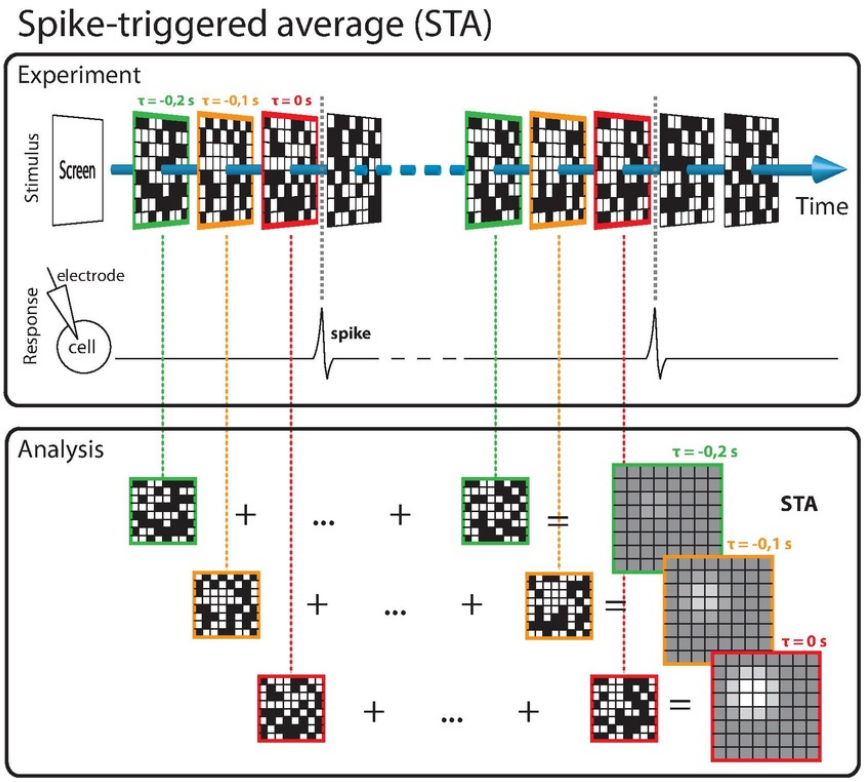

Figure 33: Illustration of receptive field calculation: a random checkerboard is presented and, in this example, spikes from a neuron are recorded. The stimuli frames in a time window preceding each spike (here consisting of 3 time bins) are selected (color boxes) and then averaged to obtain the receptive field. This specific neuron is selective for a bright spot of light just before the spike, in the top-left corner of the screen. Source: (Commons, 2015)

6.7 Computation of Directional Properties

The preferred direction (PD) of a cell was calculated as follows:

$$PD = \sum_{\varphi} r(\varphi) e^{i\varphi}, \tag{2}$$

where r is the maximum response of a stimulus moving at direction φ (0°, 45°, ..., 45°), converted to radians.

The direction-selectivity index (DSI), indicating the degree of directional bias of each cell, can range from 1 (most biased) to 0 (no directional selectivity at all) and was calculated as follows:

$$DSI = \frac{|PD|}{\sum_{\varphi} r(\varphi)} \tag{3}$$

RGCs with DSI above 0.2 were defined as direction-selective (DSGCs).

7 Results

7.1 Performance of Adjuvants for Enhanced Viral Infection

The performance of adjuvants for enhanced viral infection is summarized in table 4. In some cases, retinae were destroyed or lost during the dissection process (e.g. retinae attached to a *luftstein*), hence the occasional odd numbers of evaluated retinae. Upon brief inspection, you can see that the number of infected cells vary a lot from retina to retina. This is probably due to the variable conditions in applying the intravitreal injections: with a hand-held Hammilton syringe, the position and speed of injecting varied from retina to retina.

Table 4: Count of infected cells per retina. IV = Intravitreally; IP = Intraperitoneally.

Virus	**Infected cells per retina**				
AAV2.9.Syn.NES.jRCaMP1a.WPRE.SV40	2734	1398	6362		
AAV-dJ-hSyn-CAR-GECO1	1948	2846	333	344	
AAV-dJ-hSyn-CAR-GECO1 + D-mann. IV	380	1077	256	329	
AAV-dJ-hSyn-CAR-GECO1 + Dex. IV	1754	918	1140	3712	1669
AAV-dJ-hSyn-CAR-GECO1 + Dex. IP	337	205	1724	329	

The number of infected cells was estimated by selecting an infected area and multiplying the size of this area with mean cell density. We used this approach, since Suite2p software could detect only those cells that were in focus, which was sometimes not achieved. In addition, this estimation method was very fast to perform and turned out to yield nearly identical results as if the images were processed with Suite2p software, as shown in Figure 34.

The data from the table 4 are visualized in the form of boxplots in Figure 36. We can see that the virus *AAV-dJ-hSyn-CAR-GECO1*, which was never used in our lab before, did not perform well in comparison with *AAV2.9.Syn.NES.jRCaMP1a.WPRE.SV40*.

The performance of the adjuvants seems to be rather questionable. There does not seem to be any enhancement of the AAV infection rate. On the contrary, it seems as if D-mannitol, applied intravitreally, and dexamethasone, applied intraperitoneally, even decreased the infection rate. Dexamethasone, applied intravitreally, appears to have non-significant effect. Yet, more retinae should be first tested to verify these assumptions. For the same reason, we decided not to run ANOVA or any other statistical test. The number of retinae is simply too small.

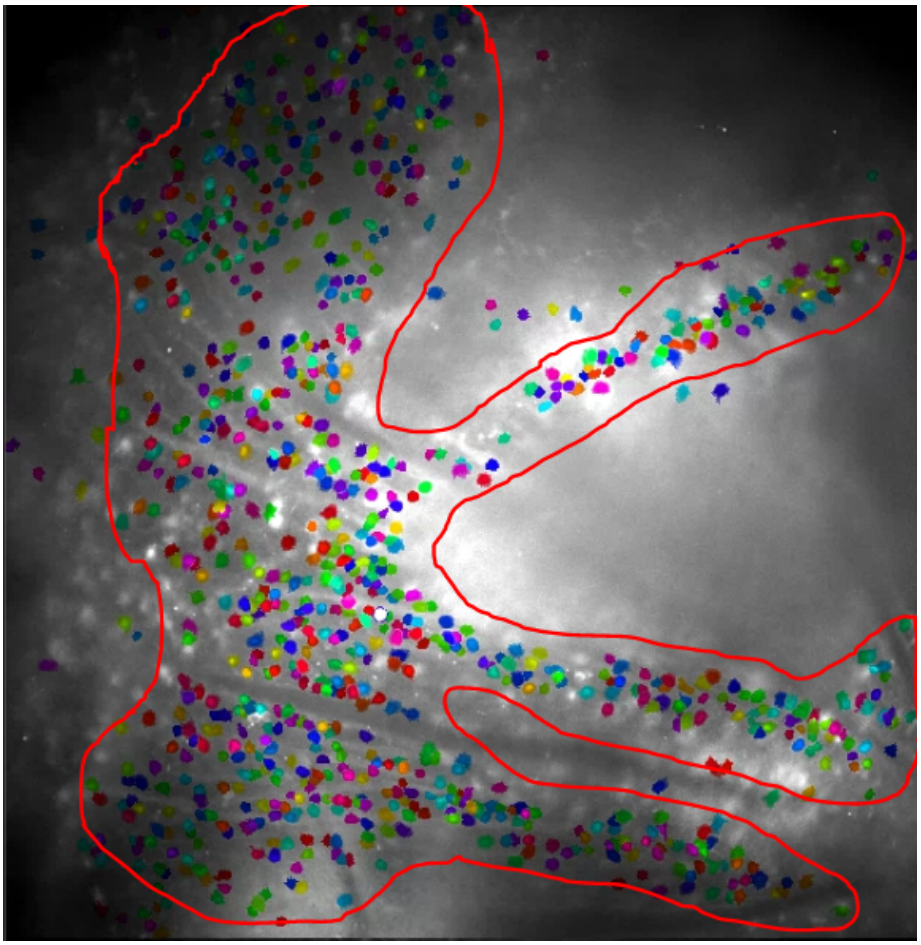

Figure 34: Estimating the number of infected cells by calculating the infected area and multiplying it with mean cell density. Mean cell density was estimated to be 20 cells over the area of 100 x 100 px ($\sim$ 225 x 225 μm^2). For this particular FOV, Suite2p identified 953 cells (see Figure 32), the estimated number of infected cells for the same area in focus is 974. In reality, however, there are many more infected cells that are not in focus and were therefore not identified by Suite2p. For instance, see the lobe in top right corner; there are many not identified cells right from this lobe. We can overcome this problem by selecting the whole infected area and estimating the total number of cells.

AAV-dJ-hSyn-CAR-GECO1

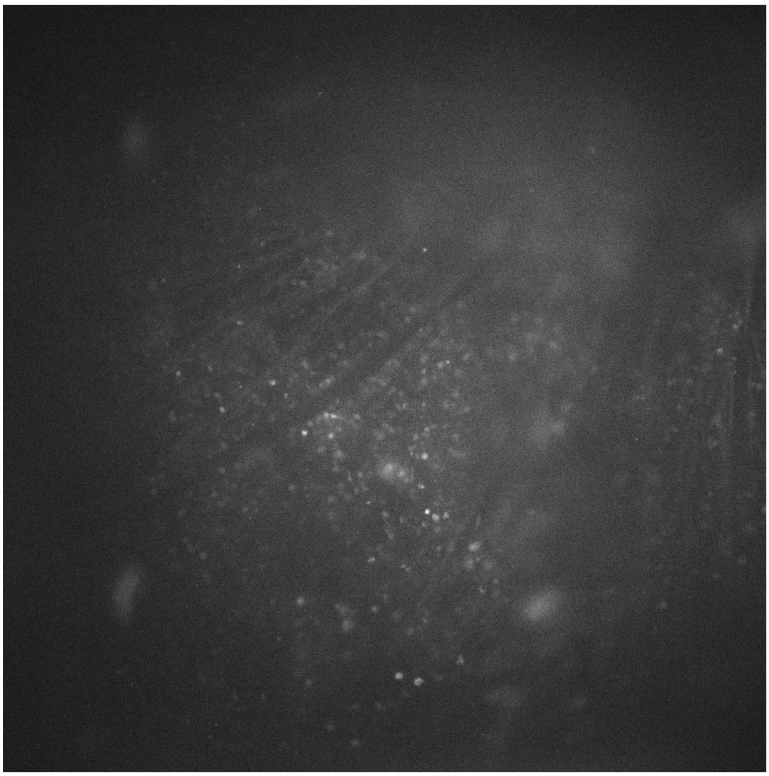

AAV2.9.Syn.NES.jRCaMP1a.WPRE.SV40

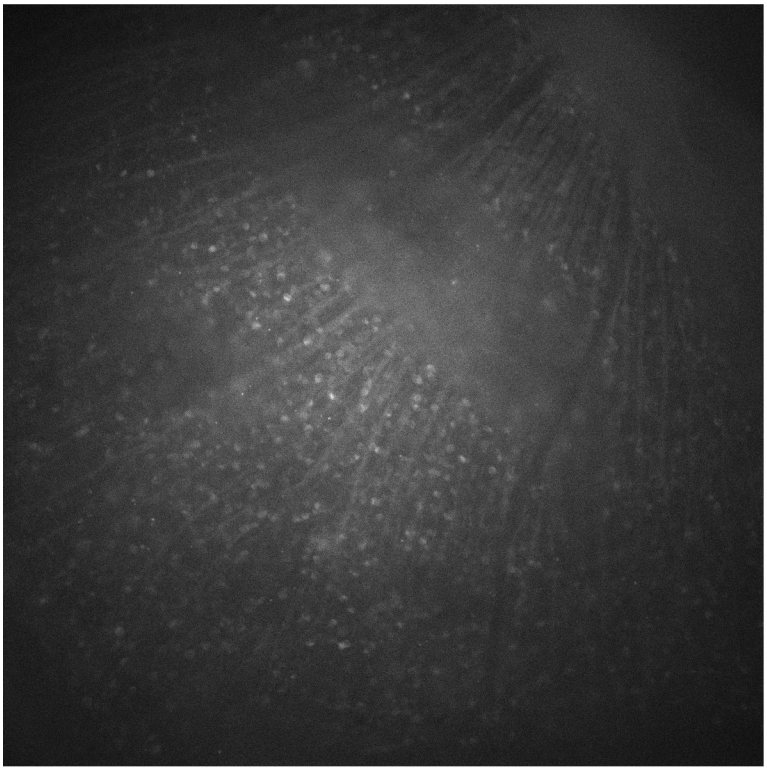

Figure 35: Upon inspection, you can see that *AAV2.9.Syn.NES.jRCaMP1a.WPRE.SV40* is a stronger fluorescence indicator than *AAV-dJ-hSyn-CAR-GECO1*; even individual axons (white strings in the image) are visible.

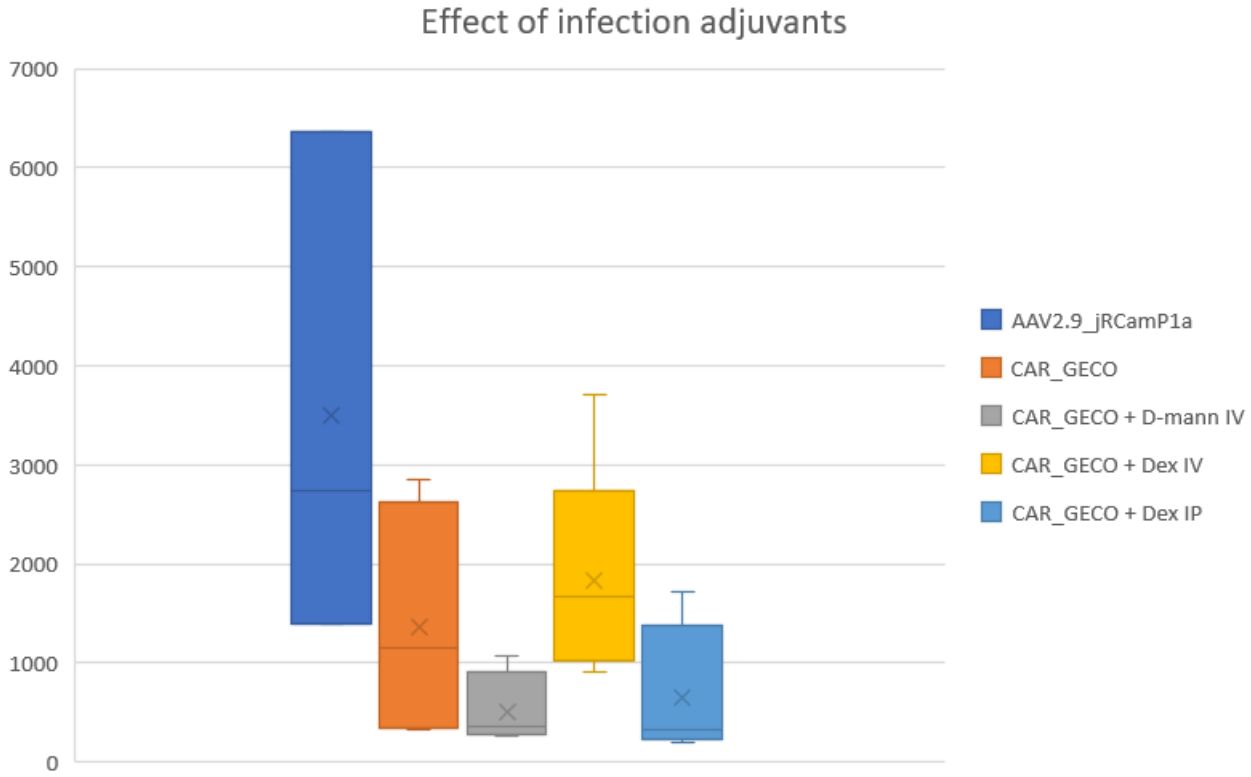

Figure 36: Performance of adjuvants for enhanced viral infection: AAV2.9_jRCamP1a (*AAV2.9.Syn.NES.jRCaMP1a.WPRE.SV40*) performed better than CAR_GECO (*AAV-dJ-hSyn-CAR-GECO1*) even with the use of adjuvants; their effect remains questionable.

7.2 Performance of Novel Stimuli for Receptive Field Computation

Comparison of computed receptive fields using the novel (middle row) and conventional (top and bottom row) stimuli, is demonstrated on 3 neurons in Figure 38.

In neuron number 2, the 45 μm checkers introduced significantly more spurious correlations, which make it difficult to clearly discern the localization of RF, compared to the outcomes from conventional 90 μm checkers and 90 μm checkers with additional random shift. This troublesome feature of 45 μm checkers was encountered frequently in other cells, too (more examples in Appendix A) and could not have been reconciled even with the 100 second time advance (45 μm checkers were presented for 400 seconds, whereas 90 μm checkers only for 300 seconds). Interestingly, neuron number 3 exhibited just the opposite scenario, where spurious correlations were introduced mainly by the conventional 90 μm checker stimulus. Neuron number 4 was free of any strong spurious correlations, notwithstanding the presented stimulus.

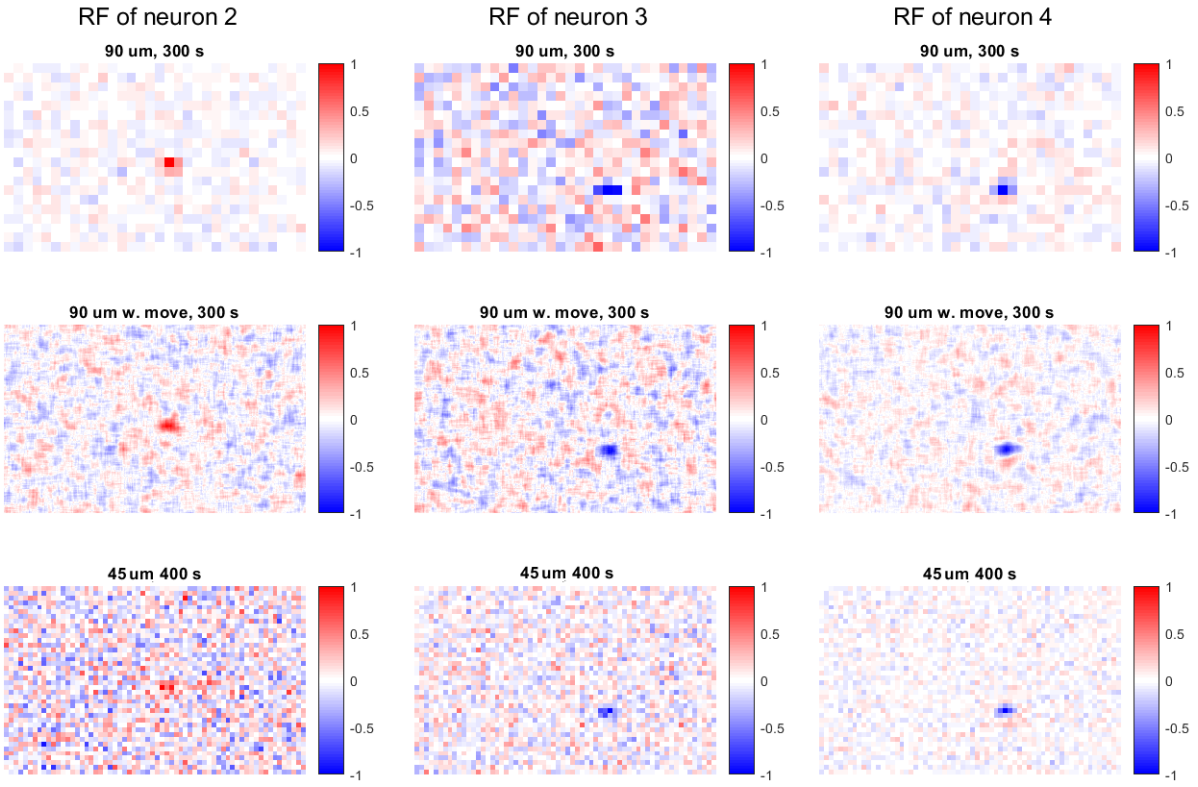

Figure 37: RF comparison of 3 neurons. Conventional 90 μm checkers (300 seconds) are shown at the top, novel approach of 90 μm checkers with additional random move (300 seconds) in the middle and 45 μm checkers (400 seconds) at the bottom.

Figure 38 shows how RF of neuron 2 looks after resampling to match the resolution of each of the stimuli: the conventional 90 μm checkers (20 x 32 pixels), the 45 μm checkers (40 x 64 pixels), and the novel 90 μm checkers with additional random shift (200 x 320 pixels). Even after resampling of the RFs we can see that the novel checkerboard outperforms the conventional checkers.

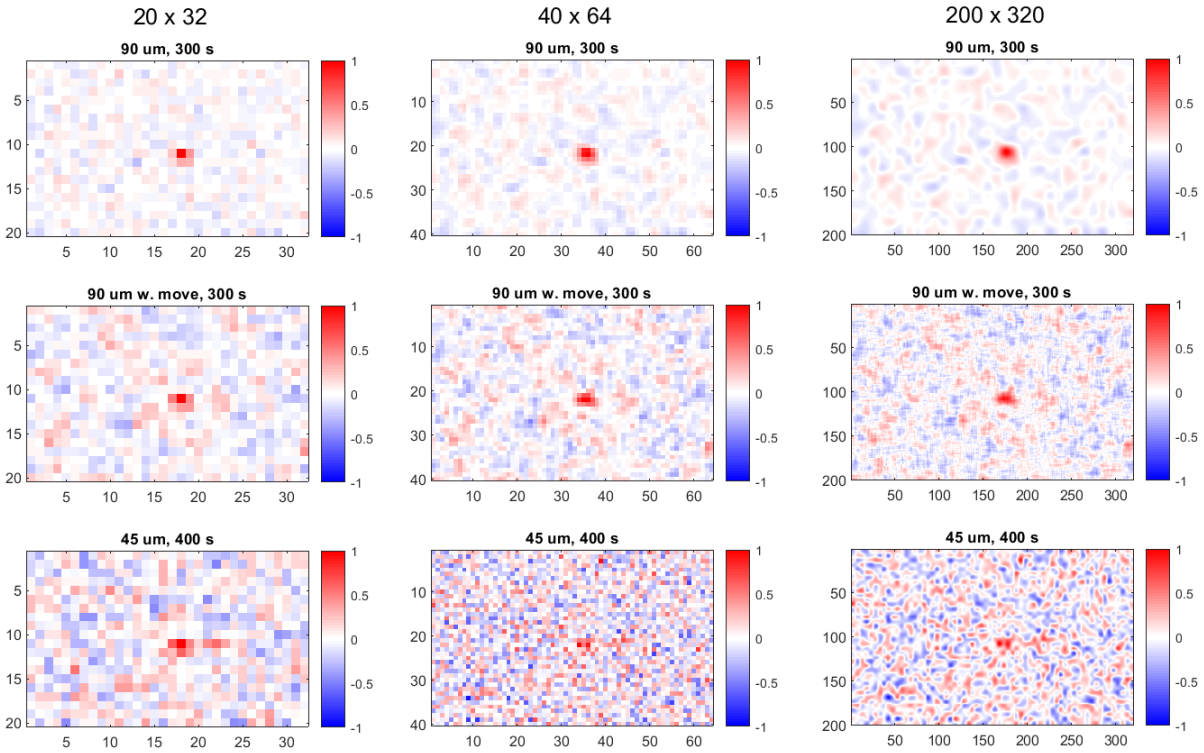

Figure 38: Comparison of RFs, resampled to match the resolution of individual stimuli, of neuron number 2. On the left, the RFs are resampled to match the resolution of conventional 90 μm checkers, in the middle to match the 45 μm checkers and on the right to match the novel 90 μm checkers with additional random move.

We then tried to push the limits of this novel stimulus even further. To do this, we first presented conventional static checkers with 150 μm size of checkers and compare the results with (1) 150 μm checkers with additional random shift of 25 μm and (2) static 25 μm checkers. The outcome is showed in Figure 40.

You can see that despite the enormous 20-minutes duration of the static 25 μm checkers, the outcome was mostly random noise. In most cases, it was impossible to discern what was an actual RF nor what polarity (ON/OFF) it had. Only in a few cases, the static 25 μm checkers provided distinguishable RF; here in Figure 40 neuron 10. This particular cell appeared to have a strong RF surround and weak center (more examples in Appendix A). This is very interesting finding per se, since such RFs were not described before.

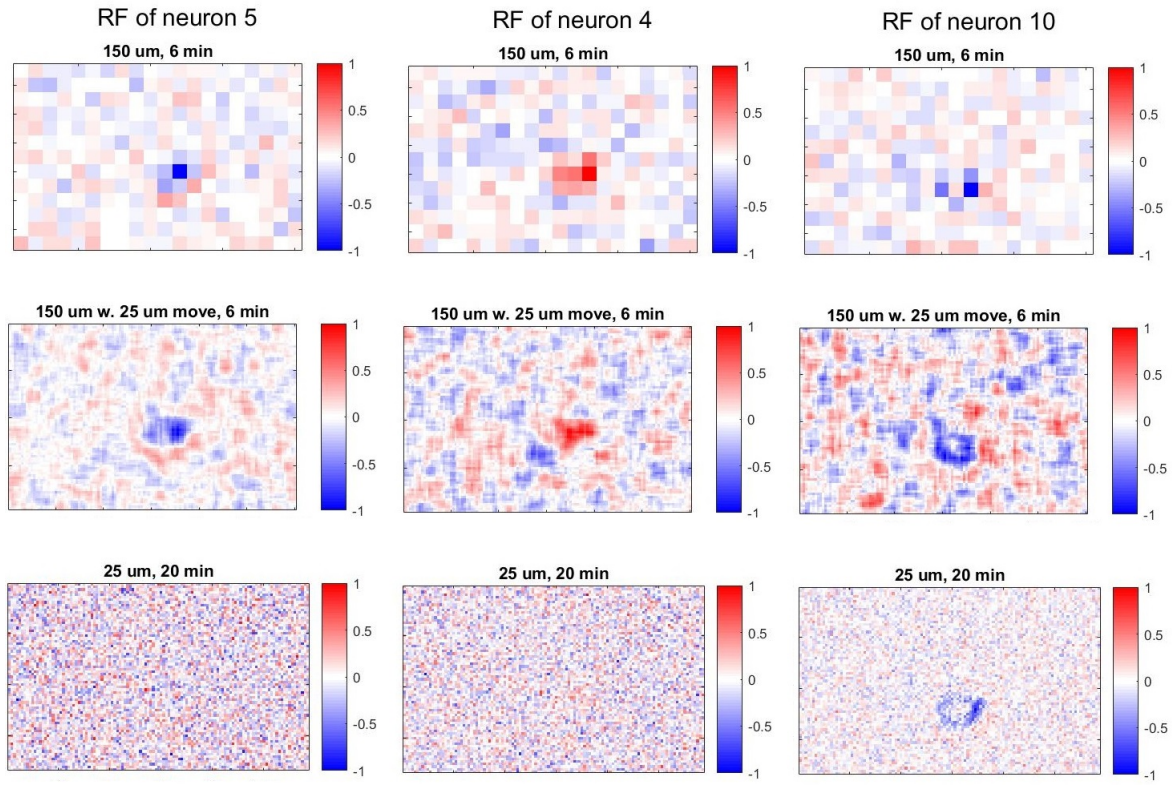

Figure 39: Comparison of a RF. Again, conventional 150 μm checkers are shown at the top, novel approach of 150 μm checkers with additional random move of 25 μm in the middle and 25 μm checkers at the bottom.

Lastly, we presented the 150 μm checkers with additional random shift of 25 μm for whole 20 minutes (Figure 39). The Figure shows cells that have strong ON center and OFF surround. With the conventional approach (bottom RFs of the Figure) it is impossible to retrieve such properties. We found many other interesting RFs (e.g. Gabor-filter- like RFs) thanks to this novel method (more than 700 RFs shown in Appendix A).

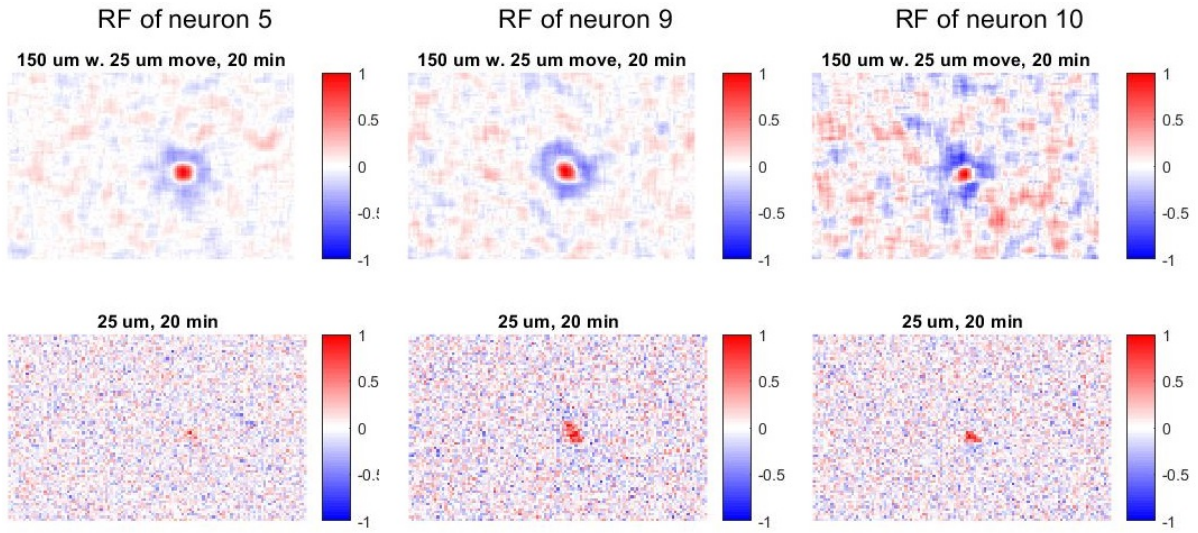

Figure 40: Example of cells with ON center and OFF surround RF. This property was detected only with our novel stimulus.

The novel stimulus clearly outperforms both variants of the conventional static checkers. In comparison with the 25 μms checkers, the novel method yields a clear and distinguishable RF every time, and unlike the 150 μm checkers it provides high-resolution mapping that can explore RFs in a much greater detail than ever possible. In addition, this high-resolution mapping can be achieved in a fraction of time that would be required by the 25 μm checkers.

7.3 Influence of Stimuli Statistics on Directional Preferences of DSGCs

When we started exploring DSGCs' properties in our lab, we used VGluT2 transgenic mice (obtained from the Jackson Laboratory). To our bewilderment, we realized that responses of DSGCs differ significantly, depending on the presented stimulus (Figure 41). What we were expecting to see was a cruciform distribution of preferred directions of DSGCs, as repeatedly demonstrated by the previous studies. However, our results did not even closely match such cruciform patterns. This was very interesting finding, since if we found that DSGCs change their preferred directions depending on the visual context, it would dramatically alter the scientific view on the role and functioning of DSGCs.

To test, whether this feature was not pure bug or whether VGluT2 mice suffered from some kind of bias against DSGCs, we looked into DSGCs responses of virally-infected wild-type mice (Figure 42). There, however, we could clearly see the cruciform distribution of DSGCs' PDs across all stimuli, suggesting VGluT2 line suffers from a bias against DSGCs. The cruciform distribution of DSGCs' PDs was apparent also in other datasets with wild-type mice recordings (more in Appendix B).

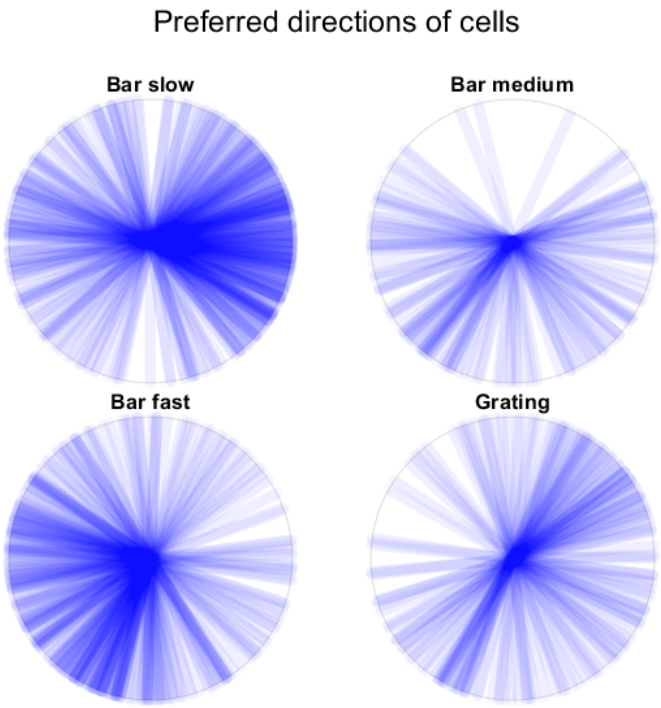

Figure 41: Non-cruciform PD distribution in VGluT2 transgenic mouse

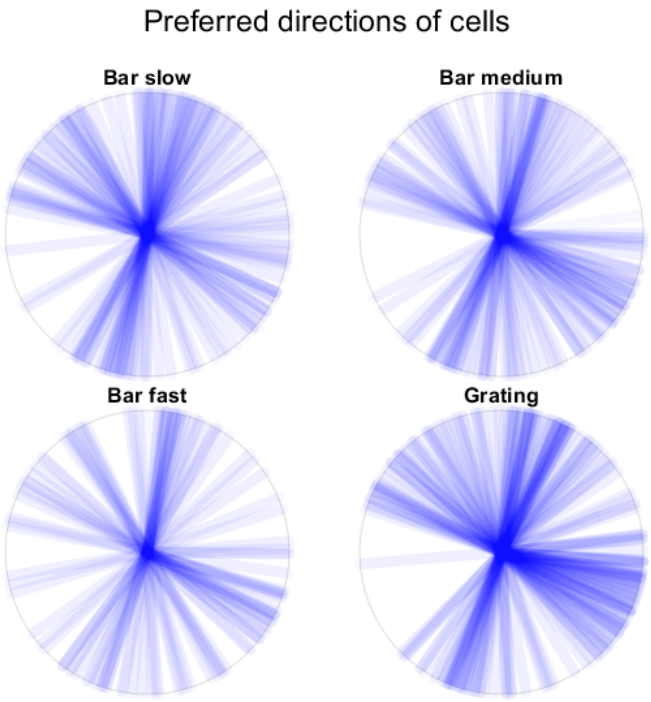

Figure 42: Preferred directions of DSGCs form cruciform distribution in wilde-type mouse, regardless the stimulus.

Still, by only looking at global distribution of PDs we might have missed angular nuances of respective DSGCs, which could be stimuli dependent nonetheless. Figure 43 presents histogram of PD angular variability of DSGCs; only PDs which elicited DSI of 0.2 or more were taken into analysis. It is clearly visible that vast majority of DSGCs have stable PDs across stimuli (i.e. angle variability is close to zero). Moreover, after inspecting raw responses of those cells that appeared to have high PD angular variability (50 degrees and more), it turned out that this behaviour is caused mostly by artifacts or noisy signal - see Figure 45).

This observation of robustness of DSGCs' preferred directions was perpetually repeated throughout all examined datasets (see Appendix B for more examples).

Unfortunately, we could not assess the DSGCs responses from natural stimuli due to synchronization problems that occurred during stimuli presentation.

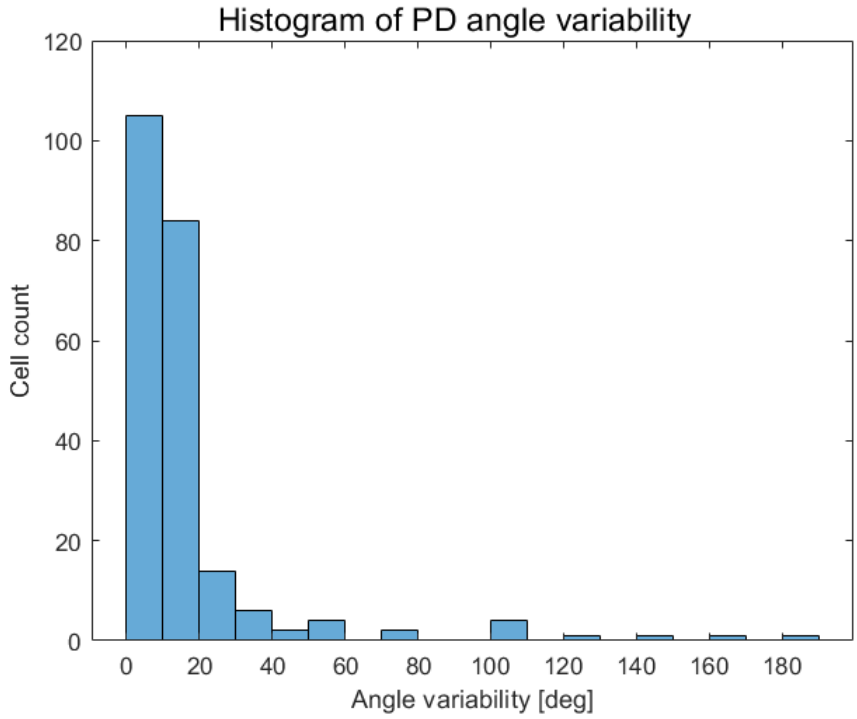

Figure 43: Majority of PDs are very stable across the stimuli. Only PDs of DSGCs with DSIs > 0.2 were included.

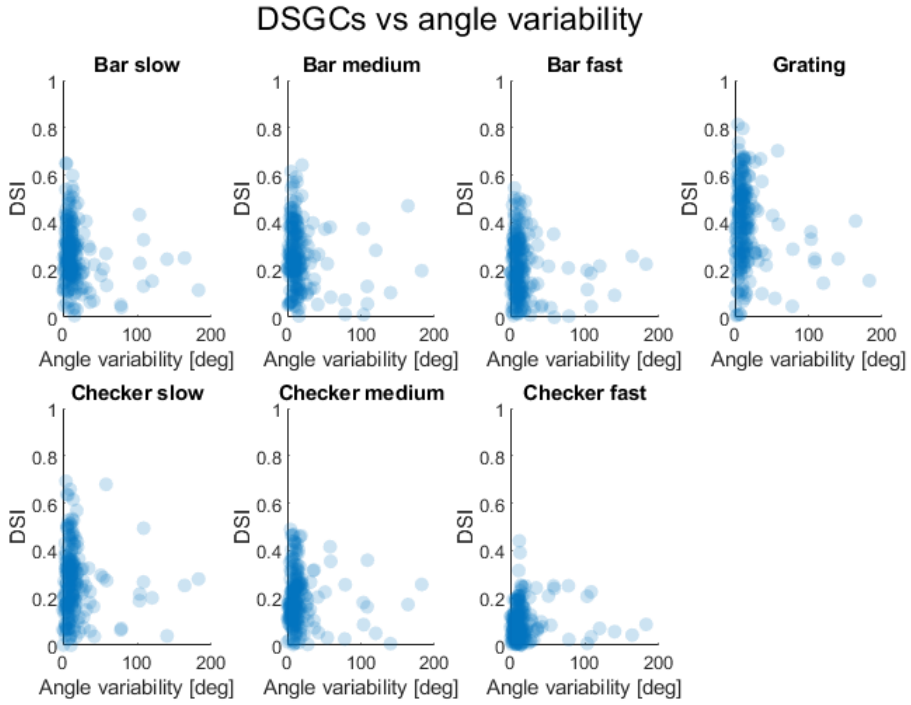

Figure 44: Angular variability from Figure 43, here replotted with DSIs of each stimulus. We can see that grating is the strongest DS stimulus.

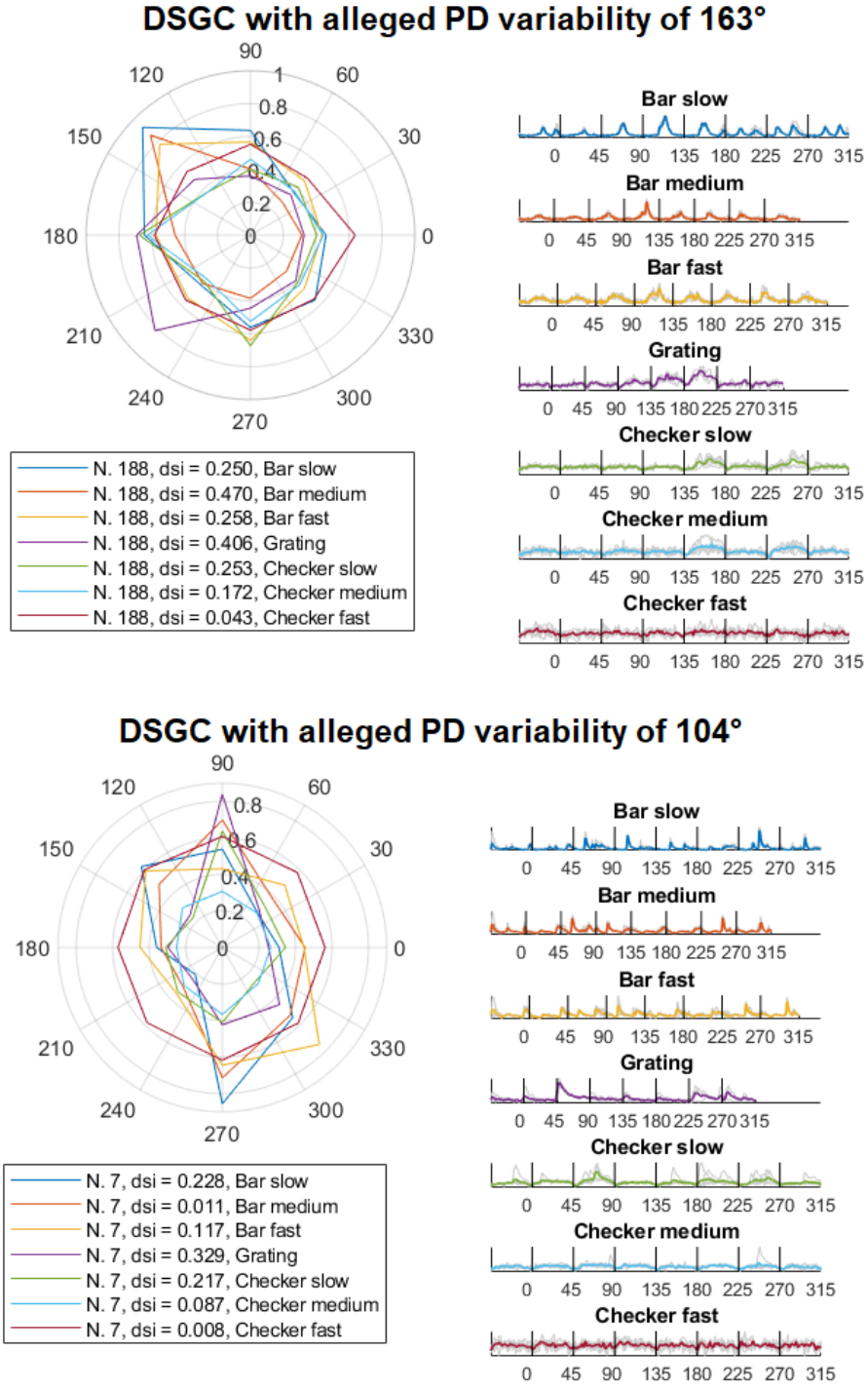

Figure 45: After inspecting raw data of DSGCs with high PD angle variability, it turned out that these outcomes are spurious. Right: individual stimuli and their raw responses: individual responses in grey, mean responses color-coded. Each of 8 equidistant angles (0...315) are separated by black line and labeled on the x-axis. Left: Directional responses of color-coded stimuli in a polar plot, with a legend indicating respective DSIs of each stimulus. Note, that the PD variability was computed only for cells with DSI above 0.2; for instance, in the case of the neuron N. 7 at the bottom, only responses from Bar slow, Grating and Checker slow were taken into account. This particular neuron seems to be an Orientation-selective RGC.

7.4 Distribution Pattern of DSGCs Across Retinal Space

Exploring the patterns of how DSGCs are distributed across the retinal space is the main goal of this thesis. To probe the DSGCs characteristics, we chose to use the grating stimulus due to its strong direction-selective drive (see Figure 44) and its short time of presentation in comparison with moving bar stimuli (3 seconds/direction vs 10+ seconds/direction).

When we plotted DSGCs, in the forms of arrows that point to PDs of respective DSGCs, back onto their original position in the image of the retina and color-coded the arrows according to the cruciform cluster to which they belonged, we started to see apparent optic flows passing through the retina (Figure 46c). For instance, optic flow of the yellow DSGCs seems to converge from left side of the image to the bottom-right corner, where optic nerve is located. Vice versa, the opposing red-colored DSGCs appear to origin from the optic nerve and diverge thence to the left side. The blue and green DSGCs appear to be aligned perpendicularly to this optic flow introduced by the red and yellow DSGC subtypes.

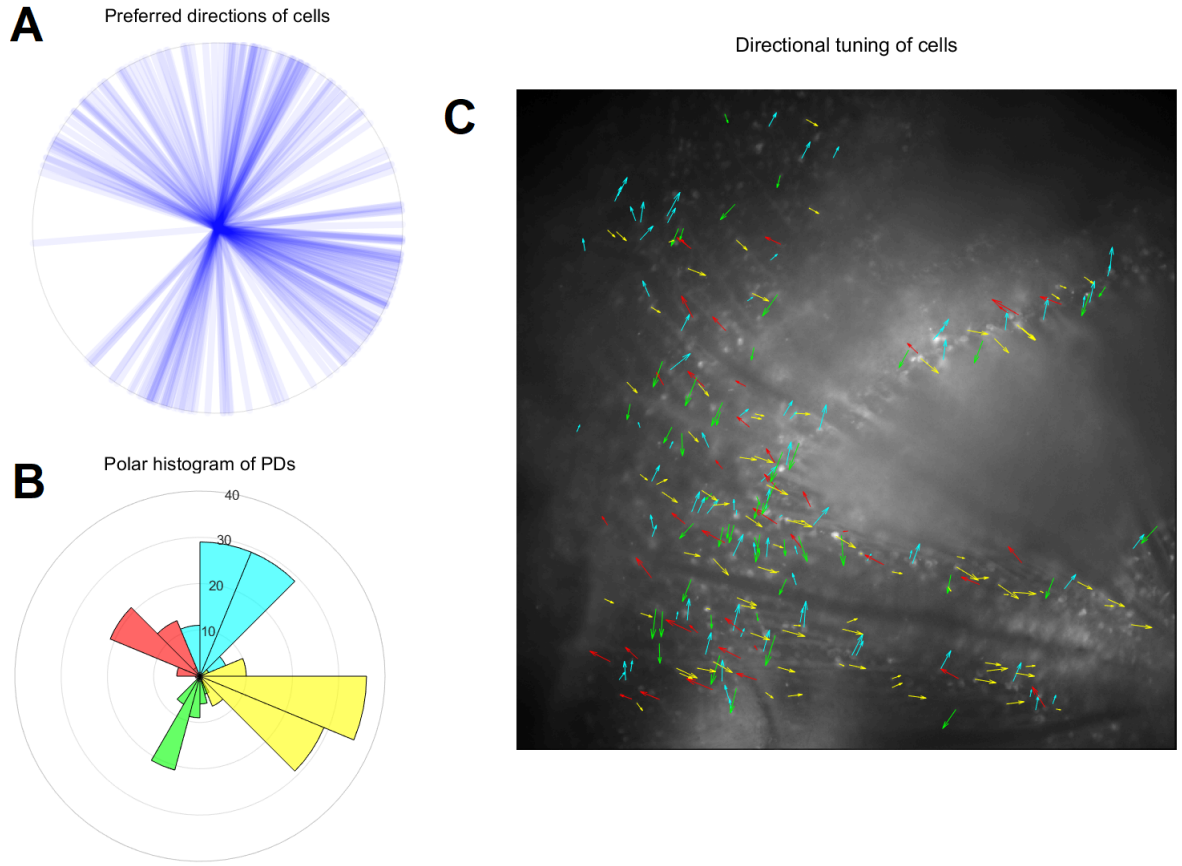

Figure 46: Populations of DSGC subtypes from apparent optic flows. A: Preferred direction of DSGCs form cruciform pattern. B: Polar histogram of A with color-coded DSGC subtypes. C: DSGCs in the form of arrows that point to the respective PD in the retina.

Another example of these optic flow distributions of DSGCs are presented in Figure 47. Here, however, we see that optic flows are not converging to the optic nerve, nor they are perpendicular to these axes, suggesting there must be some other underlying principle that would explain how these optic flows are formed. Indeed, a large study on this topic was carried out in 2007 by Shai Sabbah et al. (Sabbah et al., 2017). Here, Sabbah presented that DSGCs organize their directional preferences around the geometry of optic flow produced by translatory self-motion along two axes of high behavioural relevance: the body axis and the gravitational axis (Sabbah et al., 2017); recall Figure 13.

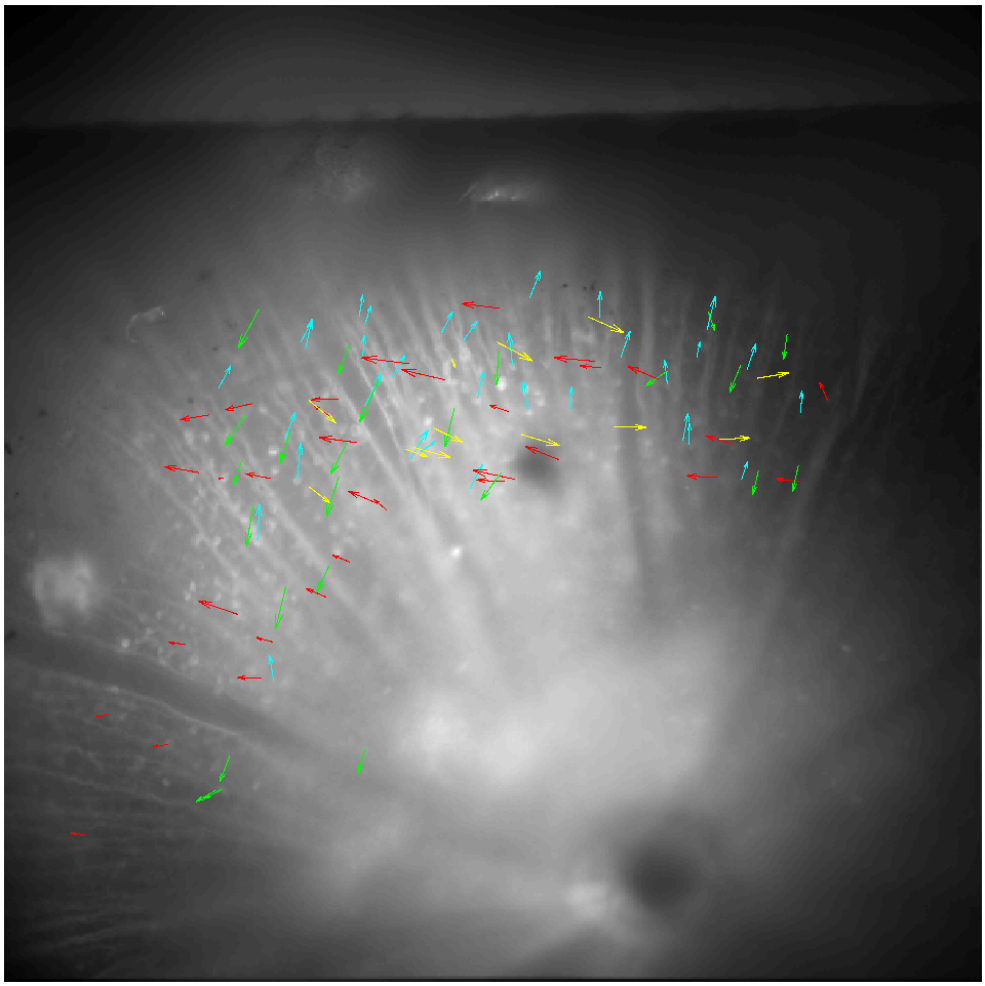

Figure 47: DSGCs are aligned along apparent optic flow axes. Here, however, we see that the optic flow pattern largely differs from that presented in previous Figure, suggesting DSGCs' PDs are not pointing along axons and arteries to the optic nerve locus (dark circle at the bottom of the image) nor they are perpendicular to this axis.

Replicating such a large-scale study with our relatively simple and low-cost setup would enable us to confirm its functionality and foreshadow potentials one could achieve with it.

To do this, we did several recordings of the retinal activity at different locations (FOVs) and subsequently stitched these FOVs together. Figure 48 presents such retinal image that is composed of total 11 recording sites (sometimes only changing the Z-axis to better focus for local unflattened parts of the retina). Again, DSGCs are represented with arrows pointing theirs PDs. This time all arrows are depicted in ocher yellow, since due to the varying cruciform distribution of DSGCs it would be difficult to cluster DSGCs back to their right subtype.

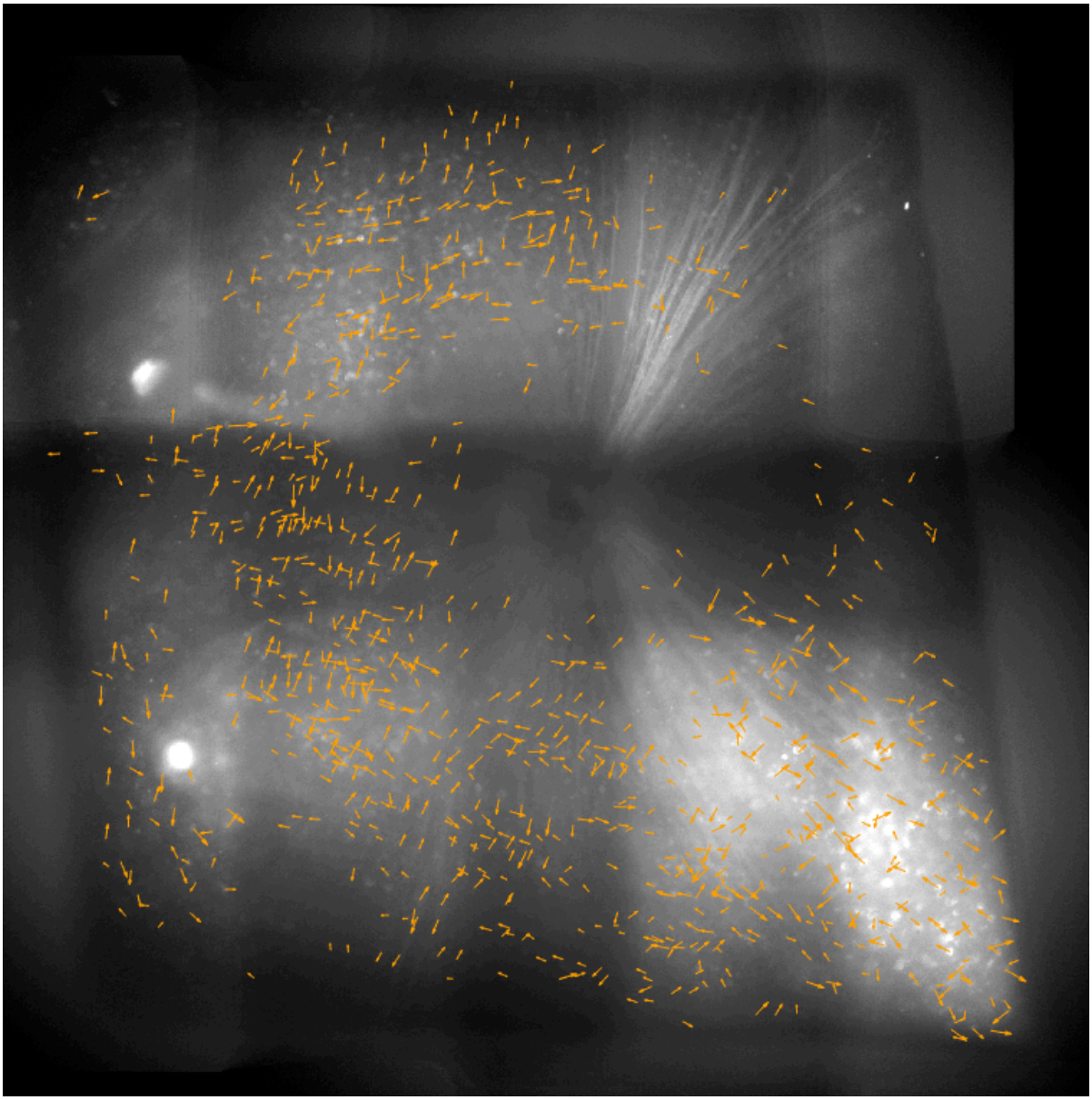

Figure 48: DSGCs represented with arrows pointing to their PDs, depicted in ocher yellow. The image is composed of 11 different FOVs.

As one can see, it is impossible to see any patterns in this tangle of arrows. A better way of visualizing the optic flows is to overlay the retinal image with local polar DSGCs histograms: each line represents PD of respective DSGC. In this way, we can clearly see the how the PD orientation changes depending on the DSGC location in the retina: around the center the DSGC distribution is perfectly cruciform. The more to the periphery, however, the more is this pattern deformed (see, for instance, how is the cruciform distribution pattern squished in the left of the image). More similarly analyzed retinae are shown in Appendix C.

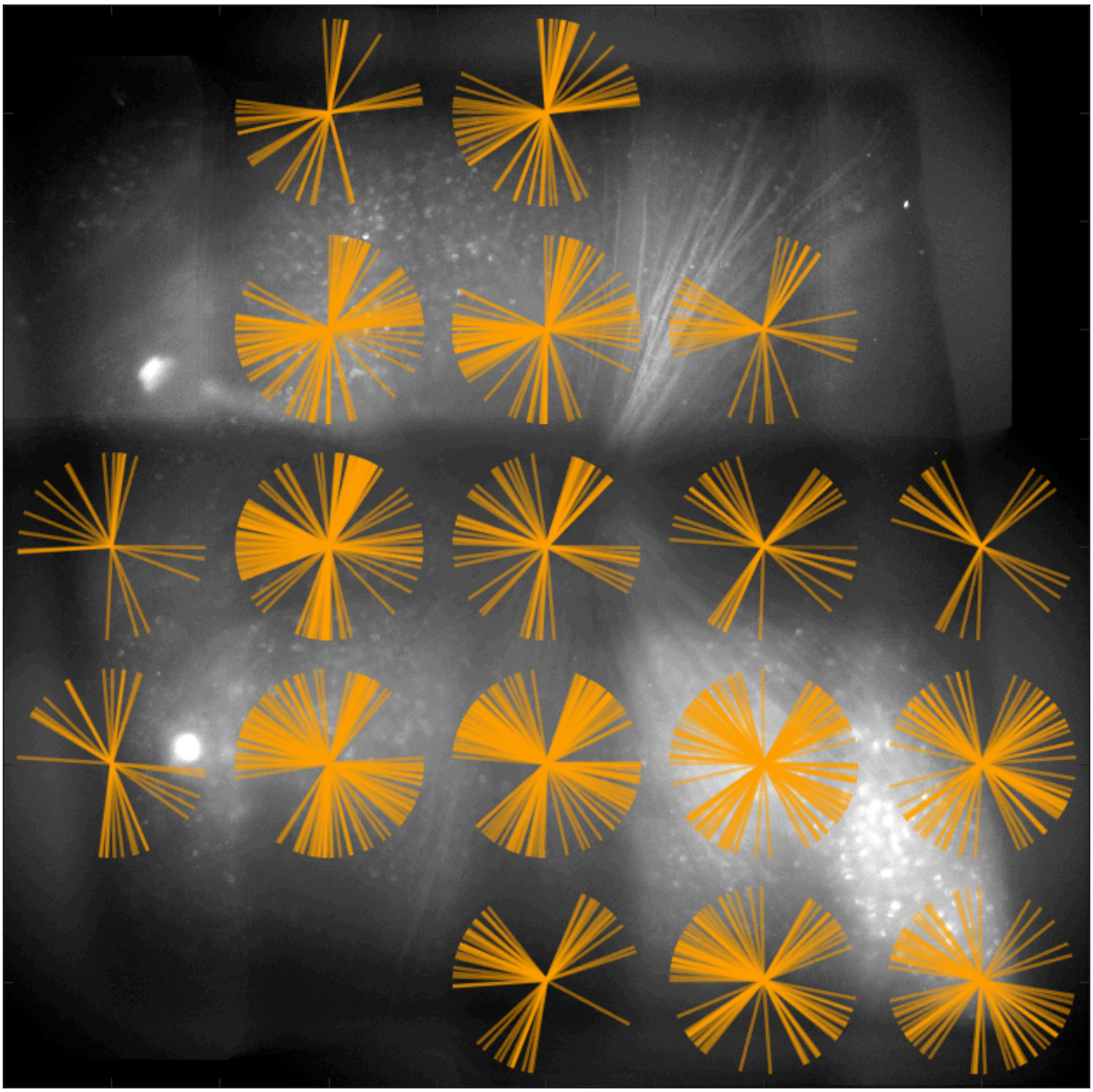

Figure 49: Same data as presented in 48, but replotted with local polar histograms of DSGCs' PDs.

Figure 50 compares outcomes of the Sabbah study (on the left) with our replication of this study (right). The green and pink curves represent the translational and rotational optic poles and their meridians that runs through the retina. They form the optic flow axes, along to which DSGCs align their PD orientations. Note that in our results on the right, possible locations of the optic poles and their respective meridians are drawn in a photo editing software for illustration purposes, the real locations of the optic poles are quite likely to be elsewhere.

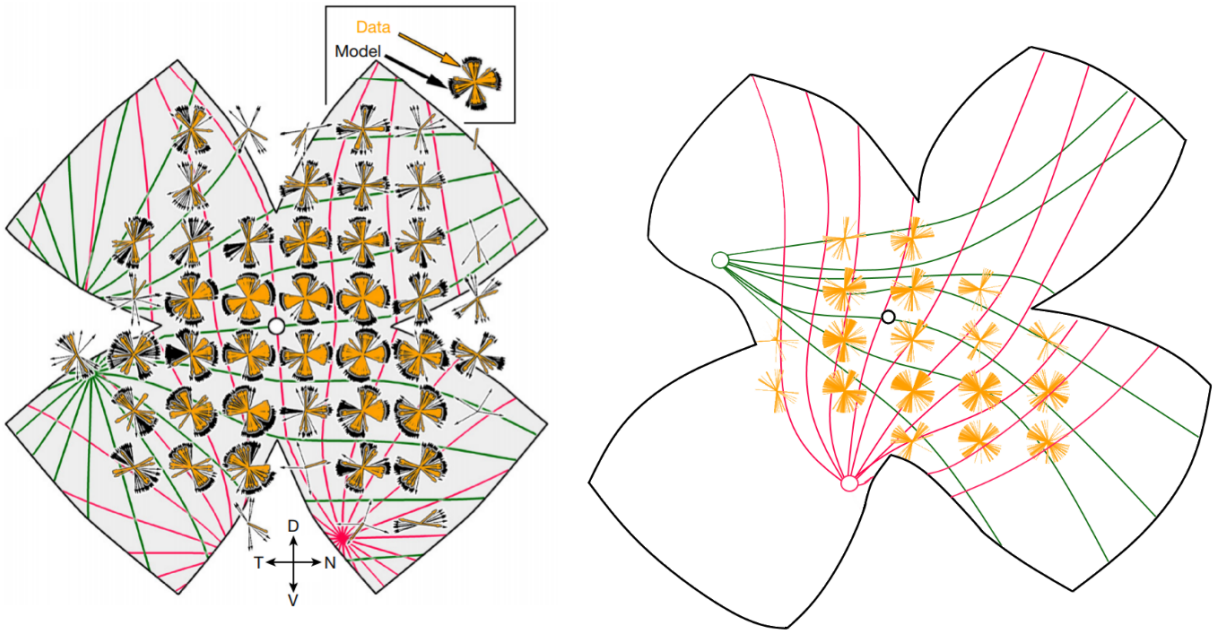

Figure 50: Left: Sabbah study on DSGCs alignment in the retina - green and pink curves denote meridians of translational and rotational optic poles; 26 retinae with >2400 DSGCs were used. Right: Outcomes from our replicating study. Note that meridians were drawn for illustration purposes only; 1 retina with 951 DSGCs was used.

8 Discussion

By recreating the already known DSGC population properties (Sabbah et al., 2017), I demonstrated that our novel one-photon microscopy method works and that it can be used for various large-scale retinal studies. With $\sim$ 40-times larger FOV than any conventional imaging methods have, our method enables us to perform large population recordings of neuronal activity with only a few experiments, compared to tens or even hundreds of experiments when using conventional recording methods. Moreover, the setup is relatively inexpensive, making state-of-the-art neuronal population studies also affordable for other labs.

Although replicating the Sabbah study may seem quite effortless according to the previous chapter, it was rather a laborious task to do: from learning how to perform good intravitreal AAV injections and how to dissect and flatten retinae to designing new stimuli, running an actual experiment and analyzing data. The main technical obstacle lay in achieving globally infected retinae with adeno-associated viruses, which carry calcium indicators of neuronal activity. First I thought that I might avoid this drawback by using transgenic mice that produce calcium indicators in RGCs on their own. However, as shown in the previous chapter, DSGCs properties were rather odd in VGlut2 transgenic mice, inconsistent with previous studies: it appeared that DSGCs were stimuli-dependent, changing their PDs with every presented stimulus. Subsequently I tested whether this behaviour is to be seen in virally infected retinae as well. It was not, suggesting there is a bias in VGlut2 transgenic mice against DSGCs, leaving us with no other alternative than to use wild-type mice injected intravitreally with AAVs.

To resolve the problem of infecting only a handful, often very localized clusters, of DSGCs, I tried using certain drugs that were described by previous studies to enhance the viral infection rate (Mastakov et al., 2001; Ghodsi et al., 1999). I was hoping to acquire globally infected retina with these adjuvants, a prerequisite for studying DSGC population properties. Unfortunately, upon inspecting a few retinae treated with these adjuvants, my hopes faded. There are two possible reasons why they did not perform as expected. Firstly, the previous studies on the effects of these adjuvants were performed in the mouse brain instead of the mouse retina, in which the adjuvants might work differently. Secondly, the adjuvants (or at least some of them) might have worked, but the effect was concealed due to other concurrent influences on the infection spread. Since the intravitreal injection procedure was carried out manually, many of its attributes (e.g. speed of injecting, injection spot etc.) differed from eye to eye. Last but not least, each mouse is unique and so might be the retinal infection. By testing many more retinae we could probably see the real effect of the adjuvants. This task, however, was beyond the scope of this thesis.

In addition to replicating the existing large-scale study, this thesis also introduces an improved stimulus for computing receptive fields of retinal ganglion cells. This novel stimulus proved to recover receptive fields at a much higher resolution than previously achieved, in a matter of several minutes. Together with our novel large-scale imaging method, not only can the improved stimulus elicit new findings on the tiling of the retina with distinct DSGC subtypes, but it also opens the door for following studies to describe space for the first time the distribution patterns of RFs across the retinal.

Bibliography

Baden, T., Berens, P., Franke, K., Rosón, M. R., Bethge, M. & Euler, T., 2016. The functional diversity of retinal ganglion cells in the mouse. *Nature*, 529(7586), pp.345–350.

Baker, M., 2013. Neuroscience: through the eyes of a mouse. *Nature News*, 502(7470), p.156.

Barlow, H. B. & Hill, R. M., 1963. Selective sensitivity to direction of movement in ganglion cells of the rabbit retina. *Science*, 139(3553), pp.412–412.

Biomedicum AAV Core Facility, U. o. H., 2017. *AAV Gene Transfer*. Available at: <http://research.med.helsinki.fi/corefacilities/aav/default.html> [Accessed 2020-04-15].

Borghuis, B. G., Marvin, J. S., Looger, L. L. & Demb, J. B., 2013. Two-photon imaging of nonlinear glutamate release dynamics at bipolar cell synapses in the mouse retina. *Journal of Neuroscience*, 33(27), pp.10972–10985.

Bridges, C. D. B., 1959. Visual pigments of some common laboratory mammals. *Nature*, 184(4700), pp.1727–1728.

Briggman, K. L., Helmstaedter, M. & Denk, W., 2011. Wiring specificity in the direction-selectivity circuit of the retina. *Nature*, 471(7337), pp.183–188.

Chai, Z., Zhang, X., Dobbins, A. L., Rigsbee, K. M., Wang, B., Samulski, R. J. & Li, C., 2019. Optimization of dexamethasone administration for maintaining global transduction efficacy of adeno-associated virus serotype 9. *Human gene therapy*, 30(7), pp.829–840.

Chen, Q., Pei, Z., Koren, D. & Wei, W., 2016. Stimulus-dependent recruitment of lateral inhibition underlies retinal direction selectivity. *Elife*, 5, p.e21053.

Commons, W., 2015. *Illustration diagram for the Spike-triggered average — Wikipedia, The Free Encyclopedia*. Available at: <https://en.wikipedia.org/wiki/File:Illustration_diagram_for_the_Spike-triggered_average.pdf> [Accessed 2020-04-15].

Denk, W. & Detwiler, P. B., 1999. Optical recording of light-evoked calcium signals in the functionally intact retina. *Proceedings of the National Academy of Sciences*, 96(12), pp.7035–7040.

Duebel, J., Haverkamp, S., Schleich, W., Feng, G., Augustine, G. J., Kuner, T. & Euler, T., 2006. Two-photon imaging reveals somatodendritic chloride gradient in retinal on-type bipolar cells expressing the biosensor clomeleon. *Neuron*, 49(1), pp.81–94.

Euler, T., Detwiler, P. B. & Denk, W., 2002. Directionally selective calcium signals in dendrites of starburst amacrine cells. *Nature*, 418(6900), pp.845–852.

Euler, T., Franke, K. & Baden, T., 2019. *Studying a light sensor with light: multiphoton imaging in the retina*: Springer.

Euler, T., Hausselt, S. E., Margolis, D. J., Breuninger, T., Castell, X., Detwiler, P. B. & Denk, W., 2009. Eyecup scope—optical recordings of light stimulus-evoked fluorescence signals in the retina. *Pflügers Archiv-European Journal of Physiology*, 457(6), pp.1393–1414.

Felsen, G. & Dan, Y., 2005. A natural approach to studying vision. *Nature neuroscience*, 8(12), pp.1643–1646.

Ghodsi, A., Stein, C., Derksen, T., Martins, I., Anderson, R. D. & Davidson, B. L., 1999. Systemic hyperosmolality improves β-glucuronidase distribution and pathology in murine mps vii brain following intraventricular gene transfer. *Experimental neurology*, 160(1), pp.109–116.

Gollisch, T. & Meister, M., 2010. Eye smarter than scientists believed: neural computations in circuits of the retina. *Neuron*, 65(2), pp.150–164.

Helmchen, F., Borst, J. & Sakmann, B., 1997. Calcium dynamics associated with a single action potential in a cns presynaptic terminal. *Biophysical Journal*, 72(3), pp.1458–1471.

Herber, D. L., Roth, L. M., Wilson, D., Wilson, N., Mason, J. E., Morgan, D. & Gordon, M. N., 2004. Time-dependent reduction in aβ levels after intracranial lps administration in app transgenic mice. *Experimental neurology*, 190(1), pp.245–253.

Jacobs, G. H., Neitz, J. & Deegan, J. F., 1991. Retinal receptors in rodents maximally sensitive to ultraviolet light. *Nature*, 353(6345), pp.655–656.

Jercog, P., Rogerson, T. & Schnitzer, M. J., 2016. Large-scale fluorescence calcium-imaging methods for studies of long-term memory in behaving mammals. *Cold Spring Harbor perspectives in biology*, 8(5), p.a021824.

Jin, Z., Zhang, J., Klar, A., Chédotal, A., Rao, Y., Cepko, C. L. & Bao, Z.-Z., 2003. Irx4-mediated regulation of slit1 expression contributes to the definition of early axonal paths inside the retina. *Development*, 130(6), pp.1037–1048.

Joesch, M. & Meister, M., 2016. A neuronal circuit for colour vision based on rod–cone opponency. *Nature*, 532(7598), pp.236–239.

Kalat, J. W., 2016. *Biological psychology*. 12 edition. 20 Channel Center Street, Boston, MA 02210,USA: Cengage Learning.

Kühn, N. K. & Gollisch, T., 2019. Activity correlations between direction-selective retinal ganglion cells synergistically enhance motion decoding from complex visual scenes. *Neuron*, 101(5), pp.963–976.

Kwak, H. W. & D'Amico, D. J., 1992. Evaluation of the retinal toxicity and pharmacokinetics of dexamethasone after intravitreal injection. *Archives of ophthalmology*, 110(2), pp.259–266.

Leamey, C., Protti, D. & Dreher, B., 2008. Comparative survey of the mammalian visual system with reference to the mouse. *Eye, retina, and visual system of the mouse*, pp.35–61.

Lin, M. Z. & Schnitzer, M. J., 2016. Genetically encoded indicators of neuronal activity. *Nature neuroscience*, 19(9), p.1142.

Looser, Z. J., Barrett, M. J., Hirrlinger, J., Weber, B. & Saab, A. S., 2018. Intravitreal aav-delivery of genetically encoded sensors enabling simultaneous two-photon imaging and electrophysiology of optic nerve axons. *Frontiers in cellular neuroscience*, 12, p.377.

Lundstrom, K., 2018. Viral vectors in gene therapy. *Diseases*, 6(2), p.42.

Mastakov, M. Y., Baer, K., Xu, R., Fitzsimons, H. & During, M. J., 2001. Combined injection of raav with mannitol enhances gene expression in the rat brain. *Molecular therapy*, 3(2), pp.225–232.

Matsumoto, A., Briggman, K. L. & Yonehara, K., 2019. Spatiotemporally asymmetric excitation supports mammalian retinal motion sensitivity. *Current Biology*, 29(19), pp.3277–3288.

Meister, M. & Berry, M. J., 1999. The neural code of the retina. *Neuron*, 22(3), pp.435–450.

Natkunarajah, M., Trittibach, P., McIntosh, J., Duran, Y., Barker, S., Smith, A., Nathwani, A. & Ali, R., 2008. Assessment of ocular transduction using single-stranded and self-complementary recombinant adeno-associated virus serotype 2/8. *Gene therapy*, 15(6), pp.463–467.

Nishimura, I., Uetsuki, T., Dani, S. U., Ohsawa, Y., Saito, I., Okamura, H., Uchiyama, Y. & Yoshikawa, K., 1998. Degeneration in vivo of rat hippocampal neurons by wild-type alzheimer amyloid precursor protein overexpressed by adenovirus-mediated gene transfer. *Journal of Neuroscience*, 18(7), pp.2387–2398.

Normann, R. A., Maynard, E. M., Rousche, P. J. & Warren, D. J., 1999. A neural interface for a cortical vision prosthesis. *Vision research*, 39(15), pp.2577–2587.

Obien, M. E. J., Deligkaris, K., Bullmann, T., Bakkum, D. J. & Frey, U., 2015. Revealing neuronal function through microelectrode array recordings. *Frontiers in neuroscience*, 8, p.423.

Peirson, S. N., Brown, L. A., Pothecary, C. A., Benson, L. A. & Fisk, A. S., 2018. Light and the laboratory mouse. *Journal of neuroscience methods*, 300, pp.26–36.

Rodieck, R. W. & Rodieck, R. W., 1998. *The first steps in seeing*. Vol. 1: Sinauer Associates Sunderland, MA.

Sabbah, S., Gemmer, J. A., Bhatia-Lin, A., Manoff, G., Castro, G., Siegel, J. K., Jeffery, N. & Berson, D. M., 2017. A retinal code for motion along the gravitational and body axes. *Nature*, 546(7659), pp.492–497.

Simmons, A. B. & Fuerst, P. G., 2018. *Analysis of retinal vascular plexuses and interplexus connections*: Springer.

Simurda, J., 2007. *Bioelektricke jevy*. Elektronicka skripta: The Faculty of Electrical Engineering and Communication, Brno University of Technology.

Sundberg, J. P., John, S. W., Nishina, P. M. & Smith, R. S., 2001. *Systematic evaluation of the mouse eye: anatomy, pathology, and biomethods*: CRC press.

Thompson, D. A. & Gal, A., 2003. Vitamin a metabolism in the retinal pigment epithelium: genes, mutations, and diseases. *Progress in retinal and eye research*, 22(5), pp.683–703.

Venkatesh, A., Ma, S., Langellotto, F., Gao, G. & Punzo, C., 2013. Retinal gene delivery by raav and dna electroporation. *Current protocols in microbiology*, 28(1), pp.14D–4.

Yonehara, K., Farrow, K., Ghanem, A., Hillier, D., Balint, K., Teixeira, M., Jüttner, J., Noda, M., Neve, R. L., Conzelmann, K.-K. et al., 2013. The first stage of cardinal direction selectivity is localized to the dendrites of retinal ganglion cells. *Neuron*, 79(6), pp.1078–1085.

Yoshida, K., Watanabe, D., Ishikane, H., Tachibana, M., Pastan, I. & Nakanishi, S., 2001. A key role of starburst amacrine cells in originating retinal directional selectivity and optokinetic eye movement. *Neuron*, 30(3), pp.771–780.

Zylberberg, J., Cafaro, J., Turner, M. H., Shea-Brown, E. & Rieke, F., 2016. Direction-selective circuits shape noise to ensure a precise population code. *Neuron*, 89(2), pp.369–383.

List of Figures

List of Tables

List of Code

List of Abbreviations

RGC retinal ganglion cell

GC ganglion cell

DSGC direction-selective retinal ganglion cell

ooDSGC ON-OFF direction-selective retinal ganglion cell

FOV field of view

RF receptive field

SAC starburst amacrine cell

GECI genetically encoded calcium indicator

AAV adeno-associated virus

AP action potential

GFP green fluorescent protein

RFP red fluorescent protein

2P two-photon

1P one-photon

PD preferred direction

DSI direction-selectivity index

STA spike-triggered average

A Appendix: Receptive Fields Reconstructed with Novel Stimulus

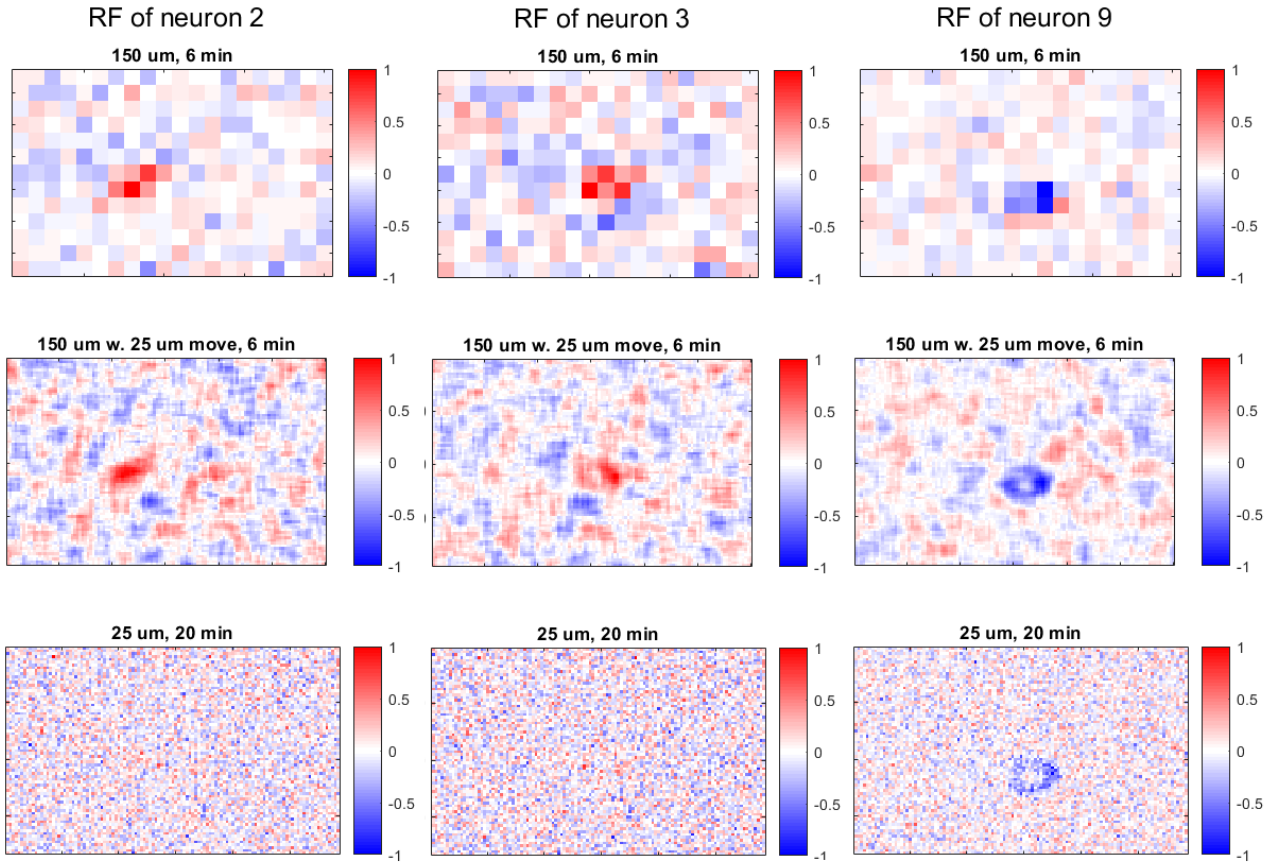

Figure 51: Comparison of a RF. Again, conventional 150 μm checkers are shown at the top, novel approach of 150 μm checkers with additional random move of 25 μms in the middle and 25 μm checkers at the bottom.

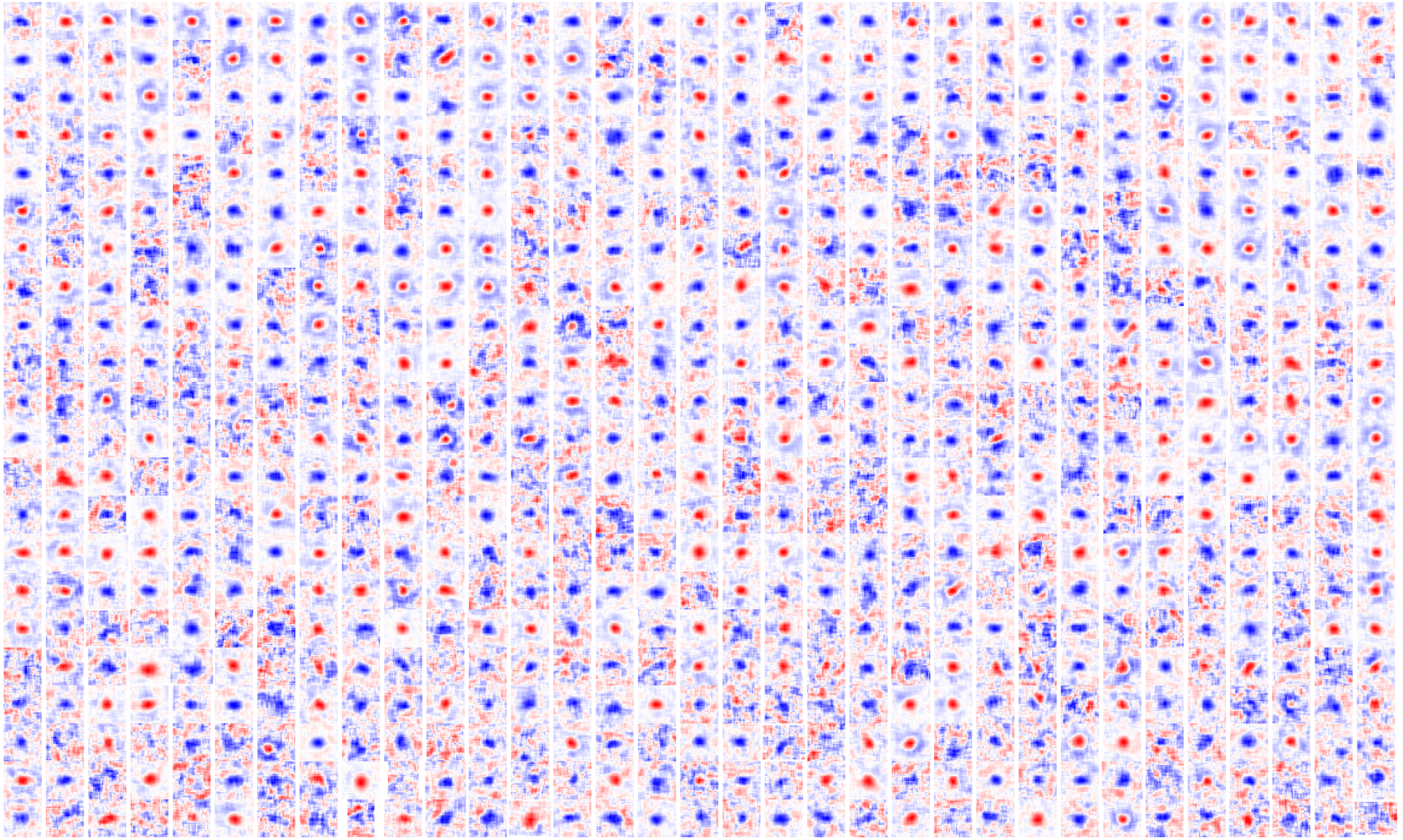

Figure 52: High-resolution RF of 700+ cells, analyzed using the novel stimulus (150 μm checkers with additional random move of 25 μ presented for 20 minutes)

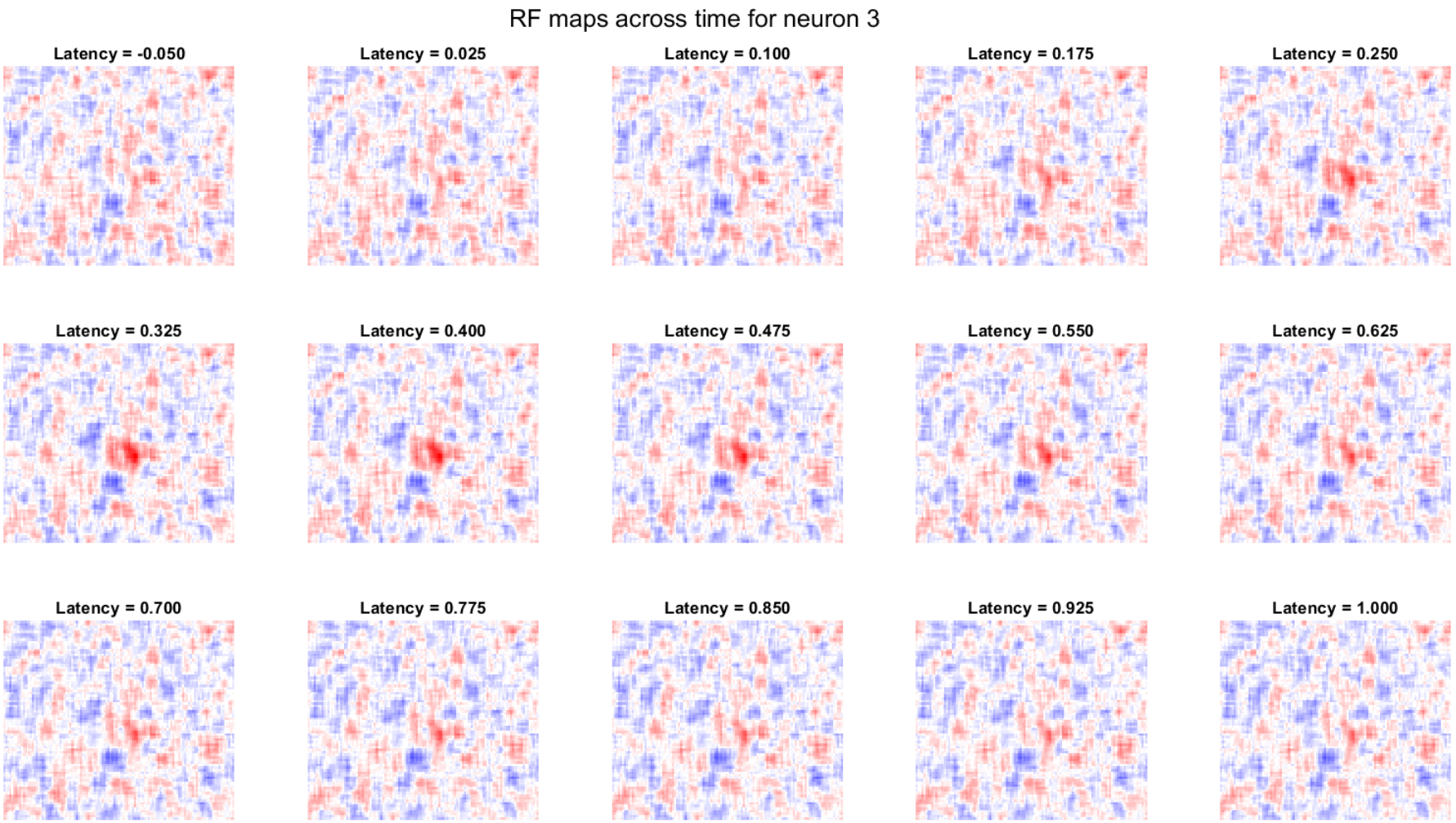

Figure 53: Temporal RF of approach of 150 μm checkers with additional random move of 25 μ for neuron 3

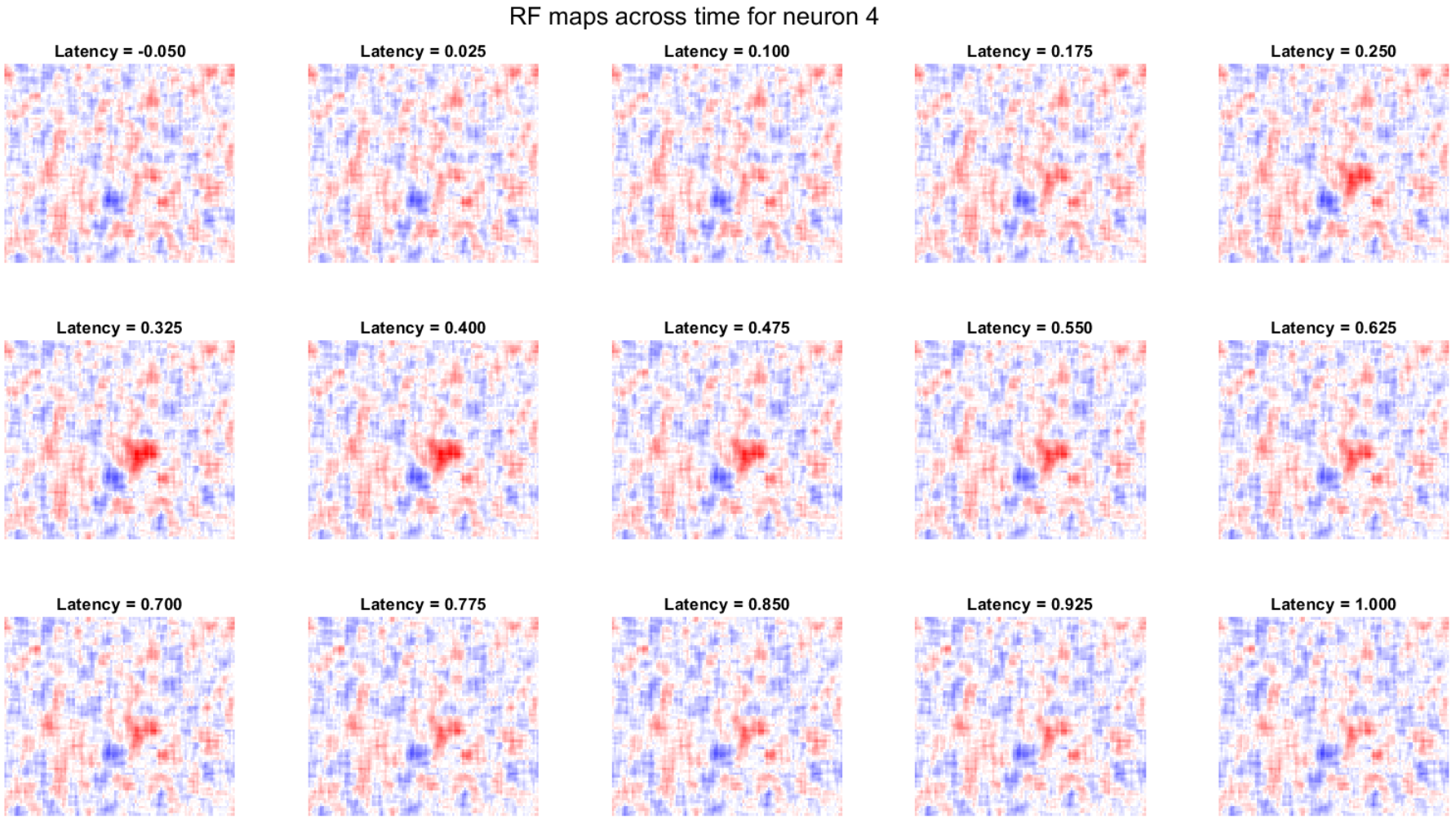

Figure 54: Temporal RF of approach of 150 μm checkers with additional random move of 25 μ for neuron 4

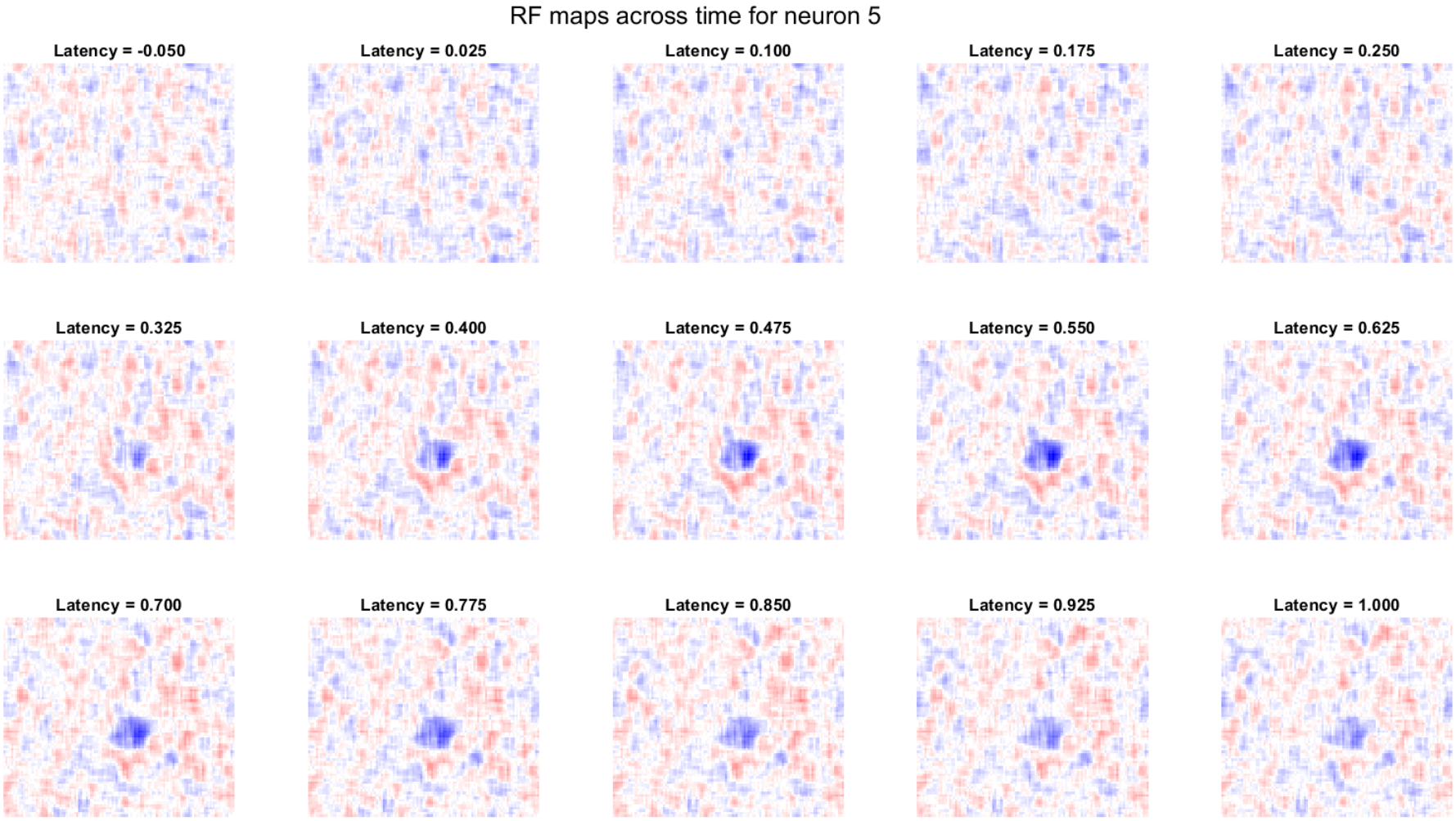

Figure 55: Temporal RF of approach of 150 μm checkers with additional random move of 25 μ for neuron 5

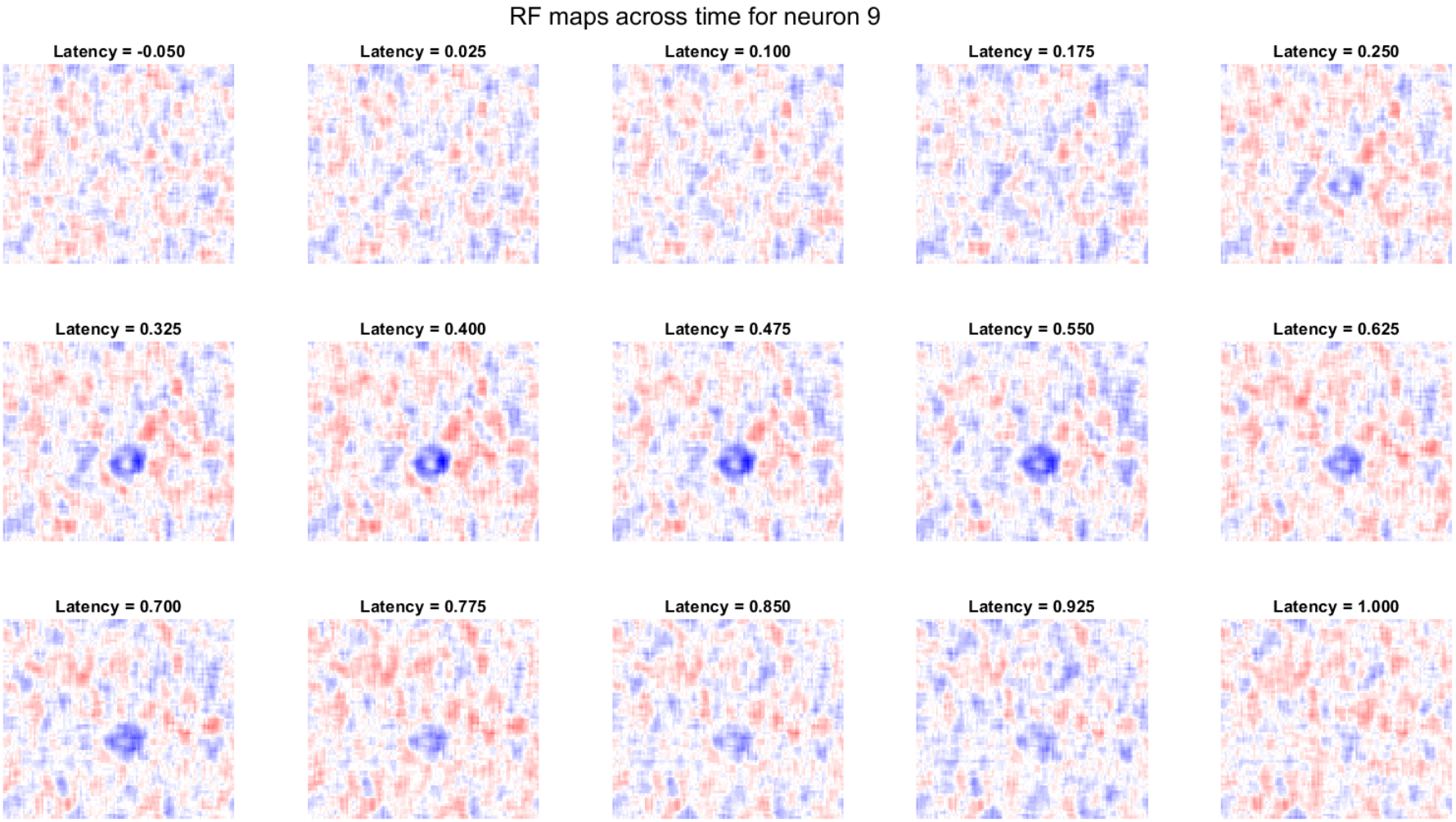

Figure 56: Temporal RF of approach of 150 μm checkers with additional random move of 25 μ for neuron 9

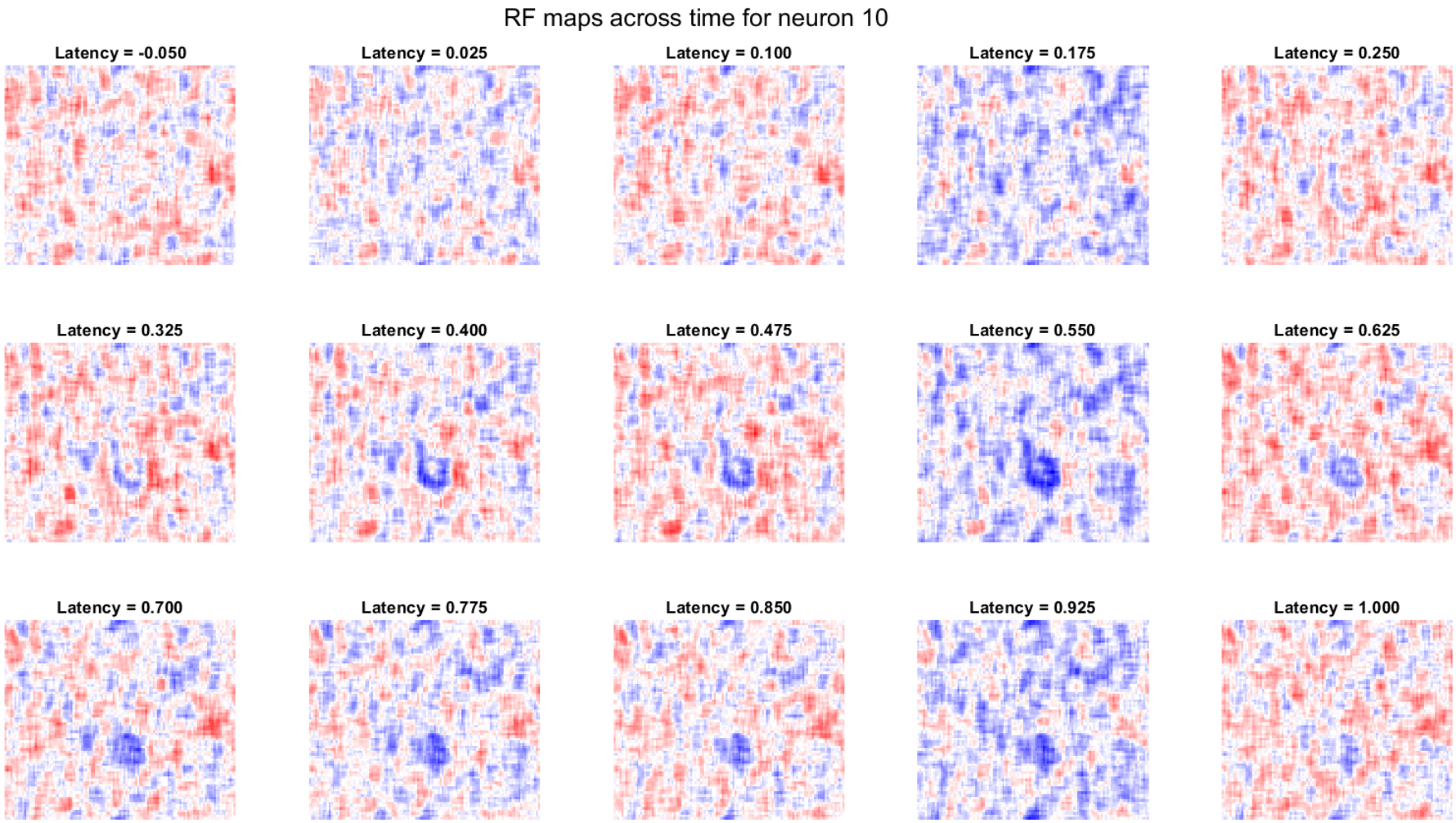

Figure 57: Temporal RF of approach of 150 μm checkers with additional random move of 25 μ for neuron 10

B Appendix: Cruciform Distributions of DSGCs

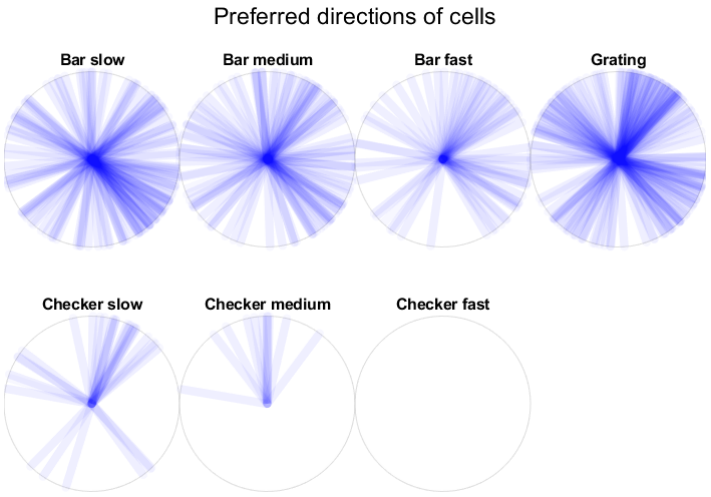

Figure 58: Preferred directions of DSGCs form cruciform distribution in wilde-type mouse, regardless the stimulus; dataset "1444".

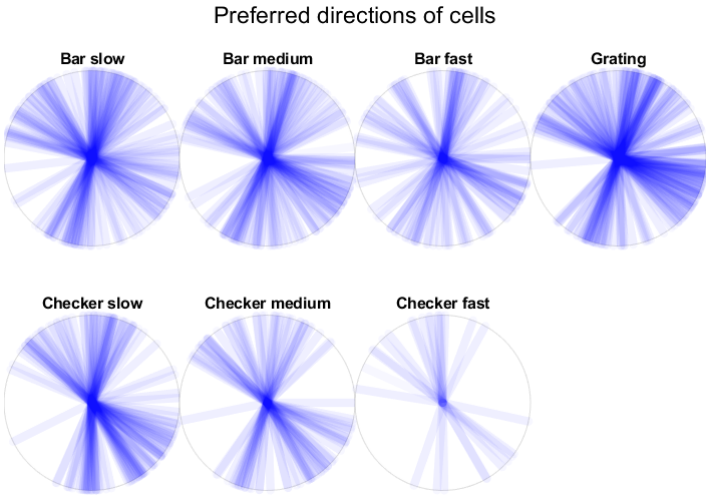

Figure 59: Preferred directions of DSGCs form cruciform distribution in wilde-type mouse, regardless the stimulus; dataset "1533".

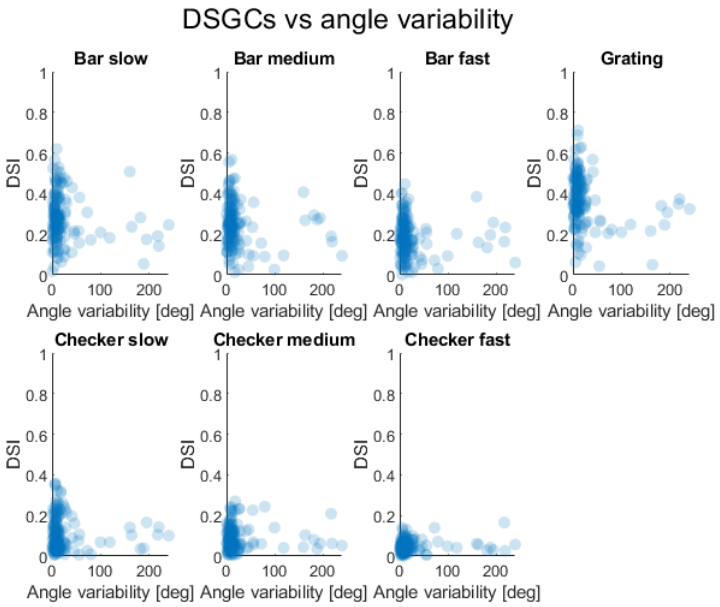

Figure 60: Majority of PDs are very stable across the stimuli. Only PDs of DSGCs with DSIs > 0.2 were included; dataset "1444".

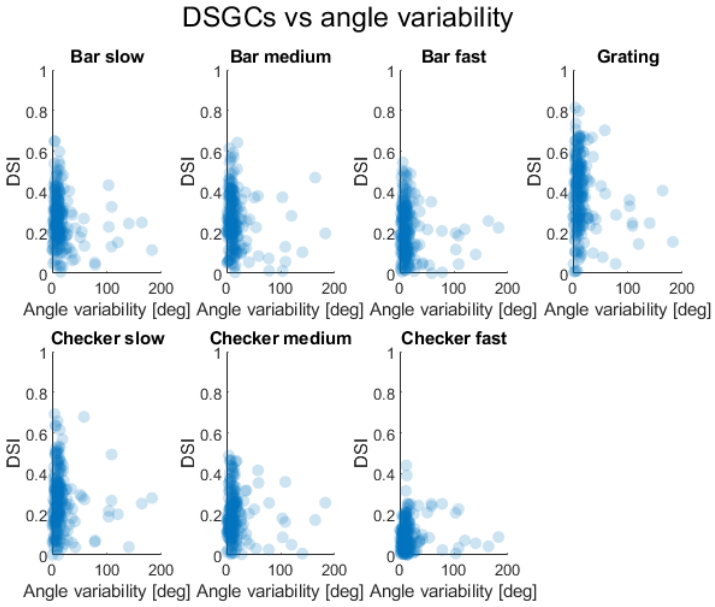

Figure 61: Majority of PDs are very stable across the stimuli. Only PDs of DSGCs with DSIs > 0.2 were included; dataset "1533".

C Appendix: Sabbah DSGCs Flowfield Patterns

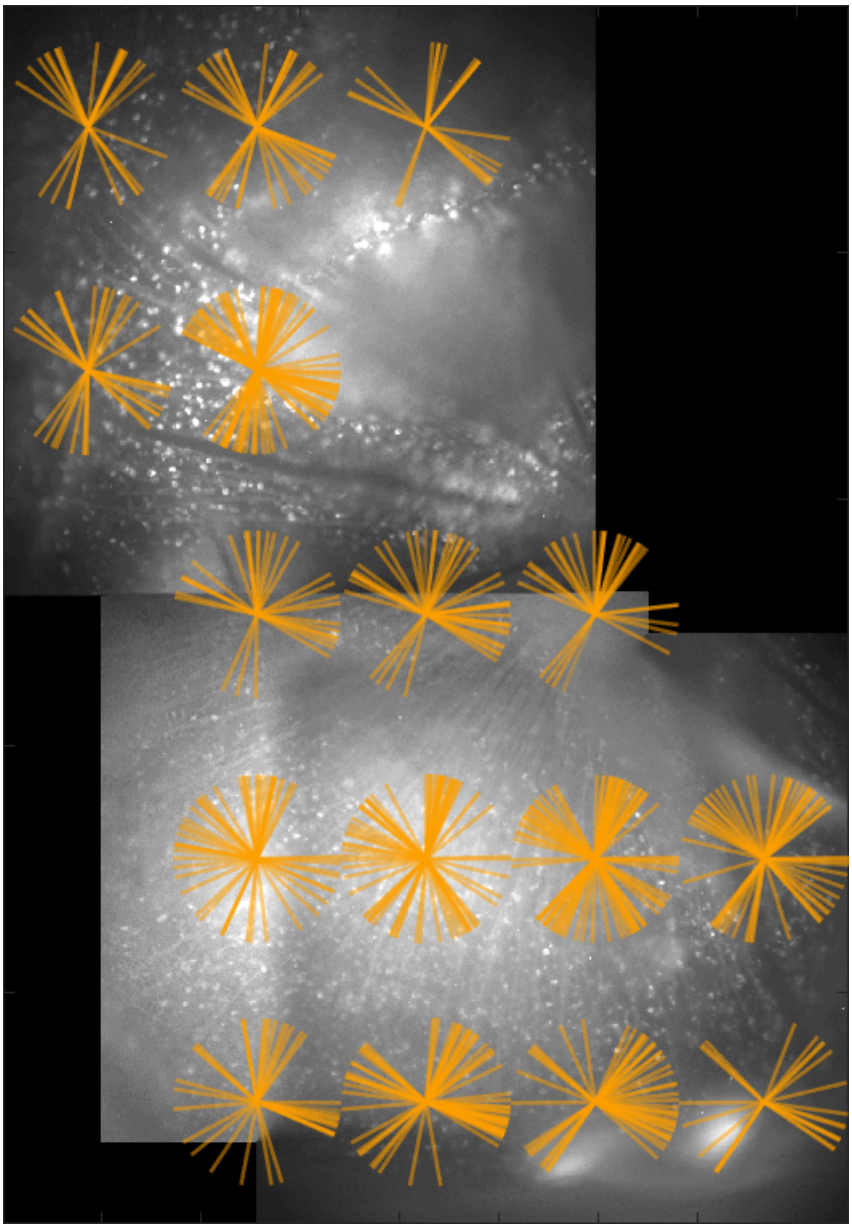

Figure 62: Stitched retina with local PD histograms, in total 3 FOVs

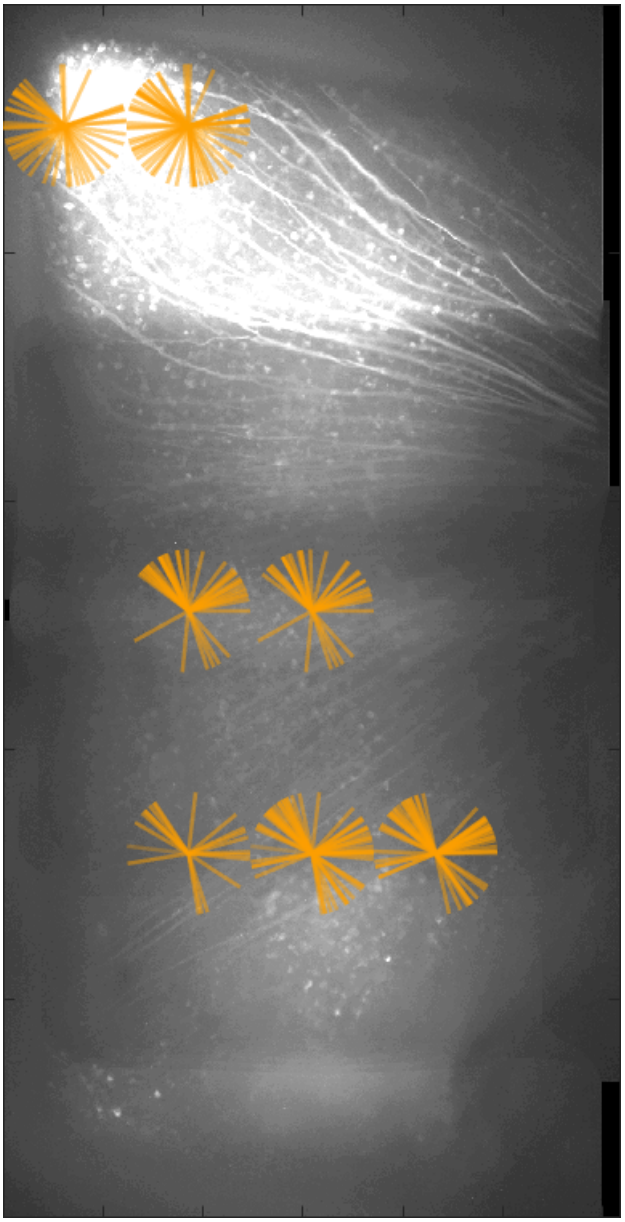

Figure 63: Stitched retina with local PD histograms, in total 7 FOVs

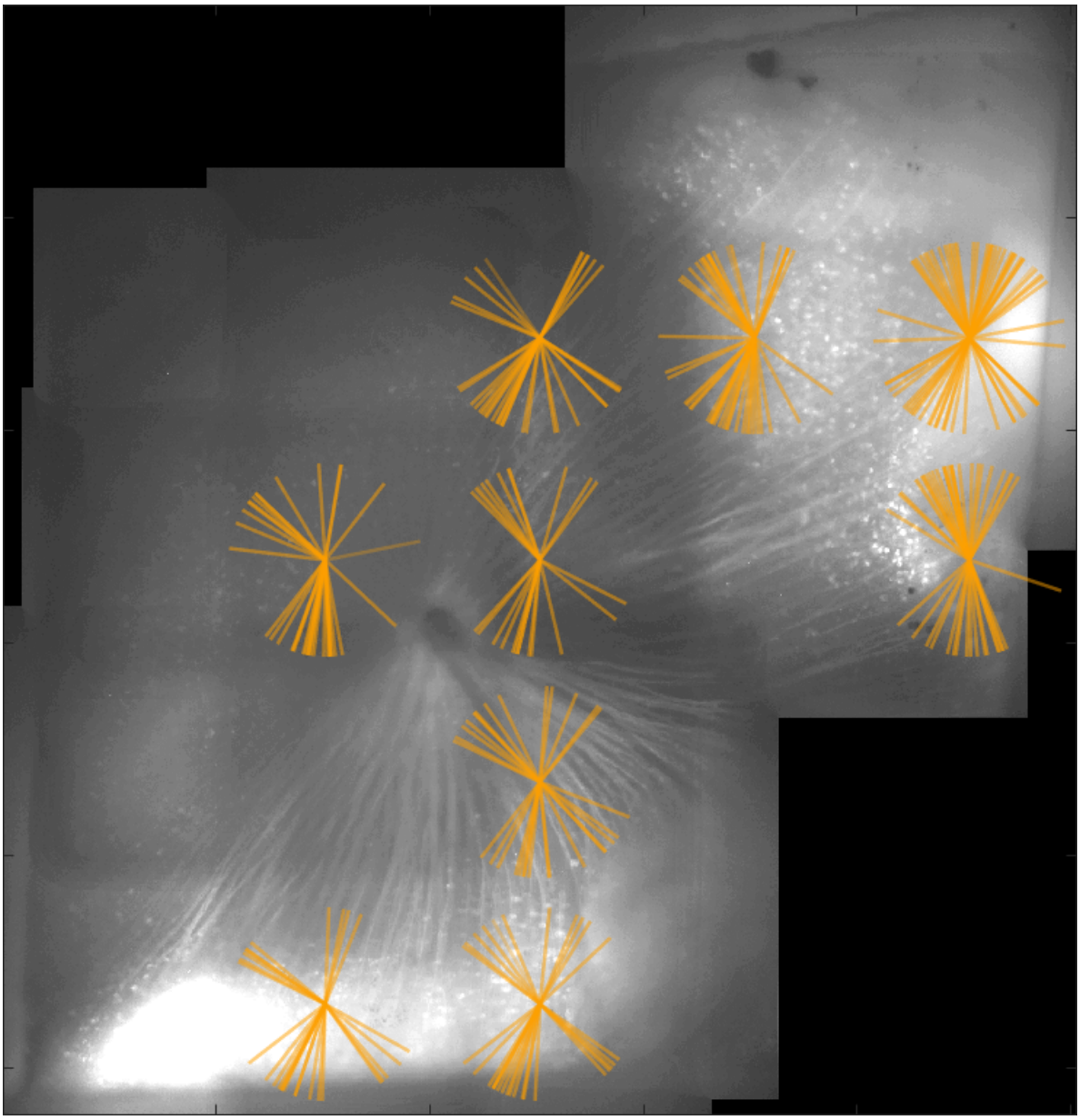

Figure 64: Stitched retina with local PD histograms, in total 9 FOVs